Noise emitted from a generic side-view mirror with different aspect ratios and inclinations

CHODE, Kushal, VISWANATHAN, Harish and CHOW, Kevin

Noise emitted from generic side view mirror with different aspect ratios and inclinations

K. K. Chode [a], H. Viswanathan [a, b *], K. Chow [c]

[a] Materials and Engineering Research Institute, Sheffield Hallam University, Howard Street, Sheffield, England, S1 1WB, United Kingdom.

[b] Department of Engineering and Mathematics, Sheffield Hallam University, Howard Street, Sheffield, England, S1 1WB, United Kingdom

[c] HORIBA MIRA Ltd, Watling Street, Nuneaton Warwickshire, CV10 0TU, United Kingdom.

ABSTRACT

Noise radiated from flow past different configurations of the Half-Round Mirror (HRM) mounted on a plate has been investigated using computational aeroacoustics (CAA). The Stress-Blended Eddy Simulation (SBES), together with the Ffowcs Williams-Hawkings (FW-H) acoustic analogy, was employed to predict near field flow and far-field noise, respectively. The numerical methodology was verified and validated for the standard HRM case against several previously published numerical and experimental data sets, which provides good agreement. Further, (i) the choice of different type of grids for CAA and (ii) the applicability of methods such as the Kirchhoff integral and the FW-H using near field inputs computed from the SBES were assessed. As a next step, the effect of induced noise from the HRM for different a) Aspect Ratios (*AR*) ranging from 1 to 2.5 and b) inclination of the mirror towards the plate (θ) ranging from 0° to 32° were investigated. For all the investigated cases, the distribution of the radiated noise exhibits a dipole-like structure closer to the plate and a monopole-like structure away from the plate. By inclining the mirror closer to the mounting plate, the emitted noise is reduced both in the vertical and lateral directions of the wake, whereas an increase in the *AR* of the mirror increases the induced noise considerably. The findings from the current study can provide a deeper understanding for effectively mitigating the induced aerodynamic noise from side-view mirrors.

* Corresponding author. Email address: h.viswanathan@shu.ac.uk (H. Viswanathan); Phone: +0441142256244.

NOMENCLATURE

Re_D	Reynolds Number
ρ	Density
ρ_o	Density in freestream
v	Fluid viscosity
t	Time
h	Height of the Half Round Mirror
D	Diameter of the Half Round Mirror
U_∞	Freestream velocity
θ	The inclination angle between the mirrors rear surface and the plate
M	Mach Number
Δ_c	Length of the cell.
C_p	Coefficient of Pressure
k	Turbulence kinetic energy
τ_w	Wall Shear Stress
P_{ij}	Compressive Stress tensor
$H(f)$	Heaviside function
$\delta(f)$	Dirac Delta function
S_{ij}	Strain rate tensor
τ_{ij}	Shear stress tensor
$\widetilde{\Omega}$	Filtered Vorticity
$\widetilde{\mathrm{S}}$	Filtered Strain rate
P'	Incompressible pressure fluctuation
p'	Pressure Perturbations
T_{ij}	Lighthill Stress tensor
P_{ij}	Compressive Stress tensor
M	Mach Number
f_s	Shielding function
C_w	WALE Constant
Δx^+, Δy^+, Δz^+	Dimensionless wall units
C_D	Drag Coefficient
p'_T	Thickness Term

p'_L	Loading Term
p^a	Acoustic Pressure Perturbations
c	Speed of sound
φ	Sound potential
L_{hx}	Length of horseshoe vortex in streamwise
L_{ws}	Length of the wake
L_{hz}	Length of horseshoe vortex in spanwise

ABBREVIATIONS

URANS	Unsteady Reynolds Averaged Navier Stokes
SA	Spalart-Allmaras
LES	Large Eddy Simulation
WALE	Wall-Adapting Local Eddy-Viscosity
DES	Detached Eddy Simulation
DDES	Delayed Detached Eddy Simulation
IDDES	Improved Delayed Detached Eddy Simulation
SAS	Scale-Adaptive Simulation
SST	Shear Stress Transport
GIS	Grid Induced Separation
SBES	Stress-Blended Eddy Simulation
FW-H	Ffowcs Williams-Hawkings
DNC	Direct Noise Computation
CFL	Courant-Friedrichs-Lewy
SSL	Separated Shear Layer
TKE	Turbulence Kinetic Energy
TVR	Turbulent Viscosity Ratio
PPW	Points Per Wave
SPL	Sound Pressure Level
HPF	Hydrodynamic Pressure Fluctuation
APE	Acoustic Perturbation Equation
AR	Aspect Ratio

I. INTRODUCTION

Aerodynamics and aeroacoustics of standard bluff bodies are subject of considerable interest owing to their widespread applications in science and engineering.[1–8] For example, during vehicle design and development stages, evaluating the noise generated due to the wind and its propagation into the cabin becomes critical as the wind-induced noise is a dominant noise source at speeds greater than 100 km/h. Frequent exposure to wind-induced noise can lead to driver fatigue, which for longer journeys may impact driver's safety at high noise levels, whereas, at lower levels of noise, it can impact the degree of vehicle refinement. With modern electrified powertrains, the migration of more tonal noises can distract the driver.[9] The flow past the vehicle A-pillar is highly turbulent, and the position of the side view mirror in this region makes the mirror a significant contributor to wind noise generated.[10] Analysis of the side view mirror is critical in designing quieter interior cabins by taking into account factors such as the shape of the mirror, the alignment of the mirror to the side window and additional design features such as turn signals and rain gutters that are changed continuously due to aesthetic merits and to avoid any tonal noise characteristics.[11] Nevertheless, by examining generic mirror configurations, a deeper understanding of the flow and emitted noise generation can be gained and offer a high degree of repeatability.

A. The Generic Side View Mirror

The Half-Round Mirror (HRM) is a generic side-view mirror model developed by Höld *et al.*[12] and Siegert *et al.*[13] based on a half-cylinder model complemented by a quarter sphere geometry at the top edge of the cylinder. The HRM is placed perpendicularly on a plate to represent an idealised assembly of the side view mirror and the side window on a vehicle. Preliminary experimental studies were conducted by Höld *et al.*[12] and Siegert *et al.*[13] to predict sound generated by HRM when subjected to a free stream velocity of 200 km/h corresponding to a Reynolds Number of $Re_D = 7.06 \times 10^5$ based on the diameter of the mirror. The experiment was performed to determine both the Hydrodynamic Pressure Fluctuations (HPF) on plate[12], and the sound radiated from the HRM.[13] Rung *et al.*[14] conducted a similar experimental study with a lower Reynolds Number (Re_D) of 5.2×10^5, representing the average driving speeds of ~ 140 km/h. The experimental studies mentioned above form the basis for understanding the noise generated from a generic mirror and stand as a benchmark for testing and validating various computational strategies.

From a numerical perspective, several turbulence modelling approaches have been carried out by researchers for hydrodynamic pressure fluctuations on both the mirror and plate.[5,14–22] The efforts based on Unsteady Reynolds Averaged Navier Stokes (URANS) and Ffowcs Williams-Hawkings (FW-H) approaches[12,13] have shown to yield a difference of up to 7dB in Sound Pressure Levels (SPL) recorded with microphones positioned around the mirror for frequencies ranging from 200 – 300 Hz, but beyond 300 Hz they show considerable disparity with experimental data and the pressure fluctuations predicted at sensors located on the mirror and the plate flatten out after 200 Hz indicating the limitation of the RANS models in resolving the intricate details of the flow which are necessary to capture high-frequency modes. Ask and Davidson[16,23,24] compared both Detached Eddy Simulation (DES) with Spalart-Allmaras (SA) and Large Eddy Simulation (LES) models with grid resolution following LES recommendations by Pope[25] with specific modifications made to the grid on HRM to avoid Grid Induced Separation (GIS). Their findings summarised that the combination of DES-SA with upwind schemes is a poor choice for resolving pressure fluctuations accurately as the upwind schemes used were dissipative. Further, they suggested that advection schemes such as second-order upwind or second-order hybrid schemes had no significant influence on downstream pressure fluctuations as long as the DES-SA model is avoided. The prediction of laminar separation point and the point of transition of the boundary layer from laminar to turbulent regions by the LES models based on Smagorinsky-Lilly and Dynamic Smagorinsky Sub-grid Scale (SGS) models are in reasonable agreement with the experiment. By analysing the flow patterns using velocity contours around the HRM, Ask and Davidson[16] demonstrated that the LES methods resolved the horseshoe vortex in front of the mirror accurately and thereby predicting the unsteady pressure fluctuations and wide range of turbulence scales which are in good agreement with experimental data for a wide range of frequencies.[12,13]

To reduce the tremendous computational resources required for a well-resolved LES owing to the near-wall mesh requirements[26] as well as to mitigate the GIS, Delayed Detached Eddy Simulation (DDES) and Improved DDES (IDDES)[27] were developed. Chen and Li[28] recently employed other hybrid formulations based on Shear Stress Transport (SST)-DES and SST-DDES to study the flow past HRM. Despite encouraging results on fundamental aerodynamic predictions such as the horseshoe vortex on the front of the mirror, wake profiles and the resulting drag, the wall pressure fluctuations were not compared with both the experimental and numerical data. In addition, both the SST-DES and SST-DDES models evaluated by Chen and Li[28] appear to under-predict the pressure magnitude in the stagnation

region and overestimate the wake compared to the LES results presented by Ask and Davidson.[16] Further, the separation point on the mirror is also under-predicted for the DES and DDES cases owing to excessive production of turbulent viscosity, which is in line with the observations made by Ask and Davidson[16,23] for their DES-SA.

For the far-field noise predictions, methods such as Ffowcs Williams-Hawkings (FW-H), Acoustic Perturbation Equations (APE), Lighthill's analogies and Direct Noise Computation (DNC) are commonly used for predicting and mitigating the induced noise from side-view mirrors.[29–33] Lokhande *et al.*[34] used the LES approach with the FW-H analogy and DNC method for evaluating acoustic and compared the numerical prediction against the experimental by Siegert *et al.*[13] The hydrodynamic pressure fluctuations were resolved accurately up to 700 Hz with a maximum deviation of 5–10 dB, and also SPL reported was in reasonable agreement with experiments at high frequencies against the experimental results of Siegert *et al*.[13] Rung *et al.*[14] observed a similar deviation in the SPL level predicted by DES with the FW-H analogy. The authors point out that the deviations in the studies mentioned above were attributed to the low-resolution of the grid in the wake and larger time steps used.[11,12] Tosh *et al.*[29] employed the SST-DES and APE on a well resolved hierarchical cartesian grid consisting of 69.6 x 10^6 cells. The unsteady pressure signatures on the mounting plate and HRM were well resolved and provided an excellent agreement with the experimental results presented by Ask and Davidson[16] for frequencies of up to 1200 Hz.The level of agreement on the HPFs with experimental data obtained by Tosh *et al.*[29] using the SST-DES is similar to a very recent study by Yu *et al.*[22] using the SST-DDES with different pressure velocity coupling based on the traditional SIMPLEC algorithm and four-step algorithm proposed by Choi and Moin.[35] However, information on the far-field noise propagation was not presented in the study of Yu *et al.*[22] Whereas with Tosh *et al.*[29], despite a good overall agreement with the experiment on the far-field noise predicted by a direct calculation, deviation of ~ 6–9 dB was observed in the mid-frequency ranges between (300 –700 Hz) among the microphone placed around the mirror, and the distant microphone was ignored. However, considering the large number of cells used in the cases mentioned above, the feasibility of extending it to realistic cases with a mirror integrated on a vehicle with the requirements proposed by Tosh *et al.*[29] may be challenging.

The recently developed SBES formulation is intended to be an improvement over both the DDES and the IDDES by providing stronger shielding over the RANS layers even with mediocre meshes by blending the eddy viscosities of both RANS and LES and offers a rapid

and definitive transition from RANS to LES.[36] The work of Chode *et al.*[37] has shown that the SBES turbulence model can accurately resolve the flow as they offer a robust blending between RANS and LES modes and rapid switch from RANS to LES in Shear Separated Layers (SSL). Despite several advantages, the SBES turbulence model is yet to be explored comprehensively for both near field and far field aeroacoustics predictions as it is a recently developed formulation.

B. Scope of Work

In real vehicles, the vortices induced from the side-view mirrors significantly contribute to aerodynamic noise generation. Previous works that have attempted to reduce noise in real vehicles have primarily modified the side-mirror topology or together with the A-pillar that have resulted in ~8–10 dB reduction on the side window.[9,38–40] However, to date, the efforts to understanding the physics of aerodynamic noise reduction from a standard mirror have not been made. Bluff body aeroacoustics analyses performed on the cylinders, square prisms, and turret studies indicate that the change in aspect ratio ($AR = h/D$) tends to change the lateral vortex size resulting in changes in unsteady pressure foot-print on the mounting surface away from the body and reduced the far-field noise by up to 10 dB.[41–43] Similarly, the HRM, which has been extensively studied as a benchmark case, can suitably be modified over a real vehicle or a mounting plate arrangement to closely mimic realistic inclinations or aspect ratios to better understand the change in noise generation that is induced by topological changes. Therefore, in this study, we present two changes to the generic side-view mirror viz., Aspect Ratio (AR) and Inclination of angle w.r.t the mounting surface (θ). For realistic cases, the angle swept by the mirror about the side window could range between 16° to 32°.

Motivated by the intricacies in mirror topologies that can potentially lead to rich flow physics associated with induced aerodynamic noise, our objectives of this study can be divided into two parts. *i)* Validate and verify the suitability of the newly developed SBES turbulence model coupled with several far-field computational techniques such as the FW-H and APE for standard mirror aeroacoustics. *ii)* Examine the behaviour of flow and the sound generated and transmitted due to *a)* changes in the aspect ratio of the standard mirror and *b)* inclining the mirror closer to the mounting plate by varying the angle swept by the standard mirror.

II. NUMERICAL METHODOLOGY

In the present study, a hybrid method is used to compute the noise generation and propagation from HRM. The hybrid method consists of two steps: *i)* the incompressible N-S equation is used to obtain flow field quantities, and *ii)* the calculation of the acoustic solution based on the obtained flow field quantities using an acoustic solver. The SBES turbulence model[36] is used with the WALE Subgrid scale model[44] in LES mode, whilst $k-\omega$ SST (Shear Stress Transport) turbulence model[45] is used in the RANS mode to obtain the flow field quantities as a first step. In the second step, the sound propagation in the domain is determined from the flow field quantities obtained using FW-H acoustic analogy.[46] In addition, the acoustic solution is computed using Acoustic Perturbation Equation (APE)[47] and discussed in the forthcoming sections to justify the choice and rationale behind choosing different methods. The formulations of all the numerical techniques used in this study are presented as follows:

The governing equation for conservation of mass is mathematically represented, as shown in Eq. 1. Considering the Mach number (M) in the present study is 0.11, the effect of compressibility and sound wave reflections are inconspicuous, and therefore, the flow is treated as incompressible.[14,16,17,23,48]

$$\frac{\partial u_i}{\partial x_i} = 0 \tag{1}$$

Here, i = 1, 2, 3 represents each direction in the Cartesian coordinate system, u_i is the velocity component and x_i the coordinate directions.

Conservation of momentum generally represents Newtons second law of motion and is mathematically expressed, as shown in Eq. 2.

$$\rho\frac{\partial u_i}{\partial t} + \rho u_j\frac{\partial u_i}{\partial x_j} = -\frac{\partial p}{\partial x_i} + \frac{\partial \tau_{ij}}{\partial x_j} \tag{2}$$

Where,

$$\tau_{ij} = 2\nu S_{ij} \tag{3}$$

and,

$$S_{ij} = \frac{1}{2}\left(\frac{\partial u_i}{\partial x_j} + \frac{\partial u_j}{\partial x_i}\right) \tag{4}$$

Here, ρ is the density of the fluid, p pressure, t time, and ν is the fluid viscosity. For three-

dimensional flow, Eq. 2 can be expressed with three equations, one for each Cartesian direction. Together, these equations (Eq. 2, 3 and 4) form the Navier-Stokes (N-S) equation.

A. Stress-Blended Eddy Simulation (SBES):

The SBES model is a hybrid RANS/LES turbulence model that is formulated to overcome the shortcomings of previously developed DES variants such as GIS and the slow transition from RANS to LES.[36] This approach relies on the subtle formulation of the shielding function f_s to shield the boundary layer in RANS while quickly shifting to LES where applicable. The proposed shielding function is at the stress and eddy viscosity level given by τ_{ij} and v_t in Eq. 5 and 6.

$$\tau_{ij}^{SBES} = f_s.\tau_{ij}^{RANS} + (1 - f_s)\tau_{ij}^{LES} \tag{5}$$

$$v_t^{SBES} = f_s.v_t^{RANS} + (1 - f_s).v_t^{LES} \tag{6}$$

The eddy viscosity and stress tensor switch to LES mode when f_s is zero, and whereas if f_s is equal to one, then both eddy viscosity and stress tensor will be in RANS mode. The SBES model allows the user to choose from the various LES subgrid-scale models available due to the unique blending of the stress and eddy viscosities of RANS and LES formulations using a shielding function. In this study, we adopt the WALE subgrid-scale model[44] as it provides a correct wall asymptotic behaviour for wall-bounded flows by estimating eddy viscosity without any dynamical algorithms or damping function, and mathematical formulation is given as follows:

1. Wall-Adapting Local Eddy-Viscosity SGS model (WALE – SGS):

The kinematic eddy viscosity is defined as

$$v_{SGS(WALE)} = L_s^2 \frac{\left(S_{ij}^d S_{ij}^d\right)^{3/2}}{\left(\widetilde{S_{ij}}\widetilde{S_{ij}}\right)^{5/2} + \left(S_{ij}^d S_{ij}^d\right)^{5/4}} \tag{7}$$

Where S_{ij}^d is the traceless symmetric part of the square of the velocity gradient tensor and is defined as

$$S_{ij}^d = \widetilde{S_{ik}}\widetilde{S_{kj}} + \widetilde{\Omega_{ik}}\widetilde{\Omega_{kj}} - \frac{1}{3}\delta_{ij}\left(\widetilde{S_{mn}}\widetilde{S_{mn}} - \widetilde{\Omega_{mn}}\widetilde{\Omega_{mn}}\right) \tag{8}$$

Where $\widetilde{\Omega}$ is the filtered vorticity and $\widetilde{S}$ the filtered strain rate. The mixing length is defined as SL-SGS filter length, and the WALE constant (C_w) is defined as 0.325. The formulation of the SGS eddy viscosity (Eq. 7) acts as an automatic damping function to ensure the SGS eddy viscosity goes to zero near the wall.

B. Ffowcs Williams-Hawkings (FW-H) Acoustic Analogy:

The FW-H analogy adopts the most general form of Lighthill's acoustic analogy[46] and can predict sound generated by acoustic sources such as monopoles, dipoles and quadrupoles. The mathematical description of the FW-H equation can be described as an inhomogeneous wave equation that can be derived using continuity (Eq. 1) and N-S equation (Eq. 2, 3, and 4) and is defined as

$$\frac{1}{c_0^2}\frac{\partial^2 p'}{\partial t^2} - \nabla^2 p' = \begin{pmatrix} \dfrac{\partial^2}{\partial x_i \partial x_j}\{T_{ij}H(f)\} \\ -\dfrac{\partial}{\partial x_i}\{[P_{ij}n_j + \rho u_i(u_n - v_n)]\delta(f)\} \\ +\dfrac{\partial}{\partial t}\{[\rho_0 v_n + \rho(u_n - v_n)]\delta(f)\} \end{pmatrix} \tag{9}$$

Where $H(f)$ is the Heaviside step function used to separate the fluid from the solid region, if $H(f) = 0$ defines the surface and $H(f) > 0$ defines the fluid region. p' is the pressure perturbations, T_{ij} is the Lighthill stress tensor, P_{ij} is the compressive stress tensor, n_j the unit normal vector pointing into the fluid, u_n is the velocity of the fluid normal to the surface, v_n the velocity of the surface in the direction normal to the surface, $\delta(f)$ is the Dirac Delta function, and ρ_0 the density of the fluid. The function $f(\vec{x}, t)$ describes the moving integration surface.

T_{ij} Lighthill stress tensor is defined as in Eq. 10

$$T_{ij} = \rho u_i u_j + P_{ij} - c_0^2(\rho - \rho_0)\delta_{ij} \tag{10}$$

Here P_{ij} represents the compressive stress tensor.

The solution obtained for FW-H formulation using Green's function contains surface and volume integrals. The surface integrals represent the contributions from monopoles and dipole acoustic sources whereas, the volume integrals represent the contributions from quadrupole sources generally in the region outside the source surface. However, the contributions of volume sources are negligible as the cases investigated in the present study are for M < 0.11, and therefore, volume integrals are neglected. The obtained solution can be rewritten in terms of pressure perturbations as

$$p'_{\mathrm{T}}(x,t) = p'_{T}(x,t) + p'_{L}(x,t) \tag{11}$$

Where,

$$4\pi p'_{T}(\vec{x},t) = \int_{f=0}\left[\frac{\rho_0\left(\dot{U}_n + U_{\dot{n}}\right)}{r(1-M_r)^2}\right]dS + \int_{f=0}\left[\frac{\rho_0 U_n\left\{r\dot{M}_r + c_0(M_r - M^2)\right\}}{r^2(1-M_r)^3}\right]dS \tag{12}$$

$$\begin{aligned} 4\pi p'_{L}(\vec{x},t) = {} & \frac{1}{c_0}\int_{f=0}\left[\frac{\dot{L}_r}{r(1-M_r)^2}\right]dS + \int_{f=0}\left[\frac{L_r - L_M}{r(1-M_r)^2}\right]dS \\ & + \frac{1}{c_0}\int_{f=0}\left[\frac{L_r\left\{r\dot{M}_r + c_0(M_r - M^2)\right\}}{r^2(1-M_r)^3}\right]dS \end{aligned} \tag{13}$$

Here,

$$U_i = v_i + \frac{\rho}{\rho_o}(u_i - v_i) \tag{14}$$

$$L_i = P_{ij}\hat{n_j} + \rho u_i(u_n - v_n) \tag{15}$$

The terms $p'_{T}(\vec{x},t)$ and $p'_{L}(\vec{x},t)$ are referred to as thickness and loading terms, respectively. In Eqs. (12) and (13), the dotted variables are the time derivatives of the corresponding variable. The subscripts *r* and *n* correspond to the dotted product of the vector with the unit normal in the radiation direction **r**/r or the surface normal **n**/n, respectively. Furthermore, M represents the Mach number calculated using the velocity **v** of the integration surface.

C. Acoustic Perturbation Equations (APE):

Ewert and Schröder[47] formulated a basic set of acoustic perturbation equations (APE) for perturbating variables, and mathematically, they are given as

$$\frac{\partial p'}{\partial t} + c^2\nabla.\left(\bar{\rho}u^a + \bar{U}\frac{p'}{c^2}\right) = 0 \tag{16}$$

$$\frac{\partial u^a}{\partial t} + \nabla(\bar{U}.u^a) + \nabla(\frac{p'}{\bar{\rho}}) \approx \nabla\emptyset_P \tag{17}$$

Here, p', $\bar{\rho}$, u^a represents the pressure perturbation, the mean density and irrotational acoustic perturbation, respectively. Whereas, $\bar{U}$ and c represents the mean velocity and speed of sound, respectively.

In Eq. 17, as the flow is incompressible and there are no heat or combustion sources, only vortex sound source function $\nabla\emptyset_P$ is considered in the right-hand terms from the original APE form presented by Ewert and Schröder[47] and the vortex sound source is the time derivative of

the incompressible pressure $\frac{\partial P'}{\partial t}$. By decomposing the pressure perturbation as $p' = \bar{\rho}\emptyset_P + p^a$, performing a total derivative operation $(\partial/\partial t + \bar{U}.\nabla)$ on Eq. 16 to include convective effect on acoustic propagation and taking the divergence of Eq. 17. A further assumption of constant density $(\bar{\rho})$ incompressible flow leads to $\bar{U}.\nabla = 0$, assuming negligible diffusion of mean velocity, applying some necessary vector algebra and using $\bar{\rho}\frac{\partial \emptyset_p}{\partial t} = \frac{\partial P'}{\partial t}$. Where P' is the incompressible pressure fluctuation, we obtain Equ. 18.

$$\frac{1}{c^2}\frac{\partial^2 p^a}{\partial t^2} + \frac{2\bar{U}.\nabla}{c^2}\frac{\partial p^a}{\partial t} + \frac{1}{c^2}(\bar{U}.\nabla)(\bar{U}p^a) - \nabla^2 p^a = -\left(\frac{1}{c^2}\frac{\partial^2 P'}{\partial t^2} + \frac{2(\bar{U}.\nabla)}{c^2}\frac{\partial P'}{\partial t} + \frac{(\bar{U}.\nabla)}{c^2}\nabla.\bar{U}P'\right) \tag{18}$$

In the absence of mean flow velocity ($\bar{U} = 0$), the wave equation reduces to

$$\frac{1}{c^2}\frac{\partial^2 p^a}{\partial t^2} - \nabla^2 p^a = -\frac{1}{c^2}\frac{\partial^2 P'}{\partial t^2} \tag{19}$$

Which further can be rewritten by introducing a sound potential quantity which is defined as $p^a = -\rho\frac{\partial \varphi}{\partial t}$

$$\frac{\partial^2 \varphi}{\partial t^2} - c^2\nabla^2\varphi = \frac{1}{c^2}\frac{\partial P'}{\partial t} \tag{20}$$

III. SYSTEM DETAILS, GRID INDEPENDENCE AND GRID CHOICES

A. Computational Domain and Boundary Conditions:

The Half-Round Mirror (HRM) with a diameter of D of 0.2 m is mounted perpendicularly on a flat plate representing a realistic vehicle side window, as shown in Fig.1(a). The plate dimensions are consistent with the previously published experimental and numerical studies.[5,14,16,23] A freestream velocity U_∞ = 39 m/s, which corresponds to a Reynolds Number $Re_D = U_\infty D/\nu = 5.23 \times 10^5$ based on the diameter of the mirror, is used in this study. The aspect ratio ($AR = h/D$) of the HRM is 1.5, defined as the height of the HRM (h) in the cross-flow direction along the y-axis over its diameter (D). For AR cases, the height (h) of the HRM is changed while the diameter (D) is kept constant, as shown in Fig.1(b). Fig. 1(c) illustrates the sweep angle (θ) made by the back face of HRM with the plate in the streamwise direction.

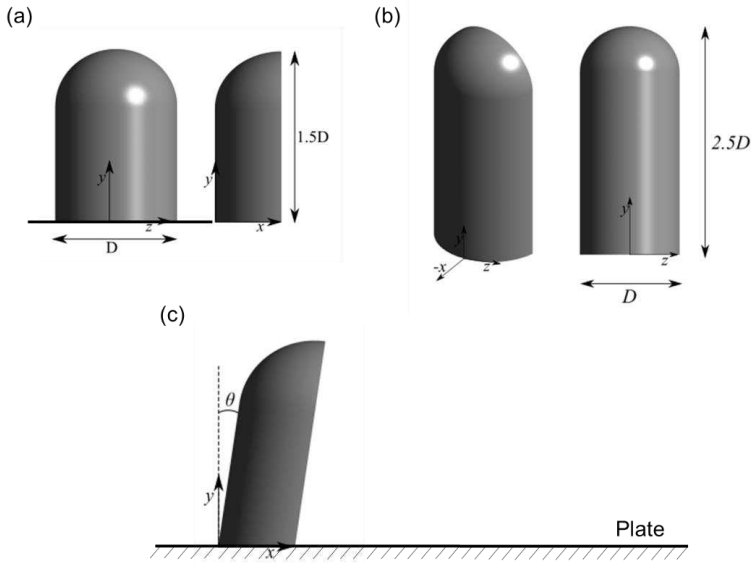

Fig.1. Geometrical representation of a) the Half-Round Mirror (HRM) as proposed by Höld *et al.*[12] and Siegert *et al.*[13] ,b) the Half-Round Mirror with an Aspect Ratio (AR) of 2.5D and c) the Half-Round Mirror with sweep angle is represented by θ.

The HRM mounted on the plate is enclosed in a computational domain of 12D x 9D x 10D (Fig. 2) and is consistent with other numerical studies conducted by Belamri *et al.*[17], Egorov *et al.*[21], Chen and Li[28], DeVilliers[20], Grahs and Othmer[49], Rung *et al.*[14], and Su and

Yu.[50] The origin of the geometrical setup is located at the centre of the front face of the mirror, as shown in Fig. 1(a). The inlet is located at a distance of 4.5*D* from the origin, and a uniform velocity condition is imposed on the inlet with a turbulent intensity of 0.1%. A constant zero-pressure outlet is applied to the outlet located at 7.5*D*. The walls surrounding the domain in spanwise and normal direction are set as symmetry, and a No-slip boundary condition is applied to both the mirror and the plate, as shown in Fig. 2.

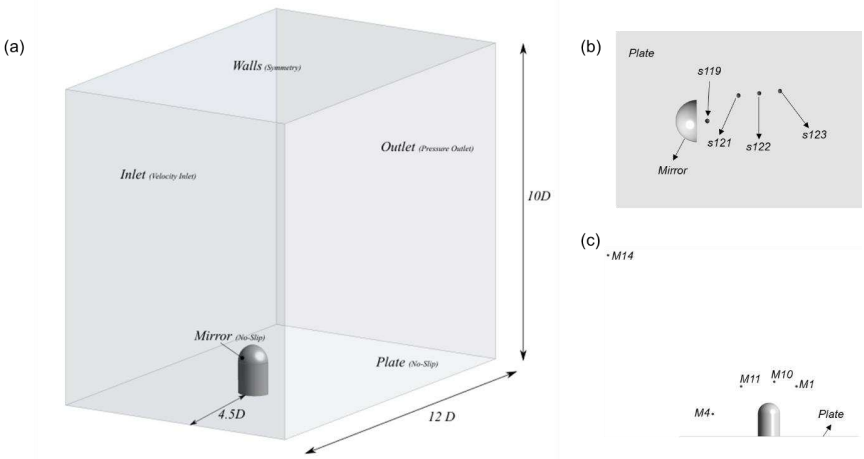

Fig. 2. a) Geometrical representation of the domain with normalised dimensions and boundary conditions used in the simulation, b) Layout of the sensor positions in the wake of the mirror, and c) Layout of the microphones around the mirror.

B. Grid Generation and Solution Setup

In this study, two different types of meshes are used: structured grid (Fig. 3) and Poly-hex core grid (Fig. 4) are investigated to verify the sensitivity of the SBES-FW-H approach. In general, the structured grids provide accurate flow solutions due to their alignment of cell faces in the flow direction and are less diffusive. Traditionally, structured meshes are preferred for aeroacoustics to obtain accurate acoustic wave propagation in the entire domain.[51] Despite such advantages, implementing a fully structured grid on complex automotive bodies such as the SAE Reference body and the DrivAer model is challenging. Therefore, unstructured grids with high levels of refinement are a good choice to solve aeroacoustics for complex bodies.[52]

The poly-hex core unstructured grid used in this study is generated using ANSYS Mosaic meshing methodology.[53] Poly-hex core grid uses polyhedron cells to capture complex geometrical surfaces accurately, and the volume region is filled with octree hexahedron

elements. A smooth transition from surface mesh to freestream is obtained using layers containing regular polyhedral cell to adjust for the cell size difference called peel layer.[53] However, local grid refinements are needed to improve accuracy for unstructured grids, and the obtained solution must be grid-independent. Thus, a grid evaluation study is performed using three grids: Coarse grid, medium grid and fine grid. The SBES-FW-H solution obtained from a grid-independent solution is compared against the SBES-FW-H solution from the structured grid to estimate the grid settings accuracy. The structure grid investigated in this study is previously used by Ask and Davidson[16], Belamri *et al*.[17], Egorov *et al.*[21] and Yao and Davidson[5] to determine the accuracy of the flow equations by evaluating wall pressure fluctuations. The grid sizes used in this study estimate the wall pressure fluctuations accurately but not the induced noise. Therefore, we present the noise-induced and propagated by HRM using SBES-FW-H and APE for the structured grid. The total cell count for the structured grid is ~2.8 x 10^6 and is shown in Fig. 3.

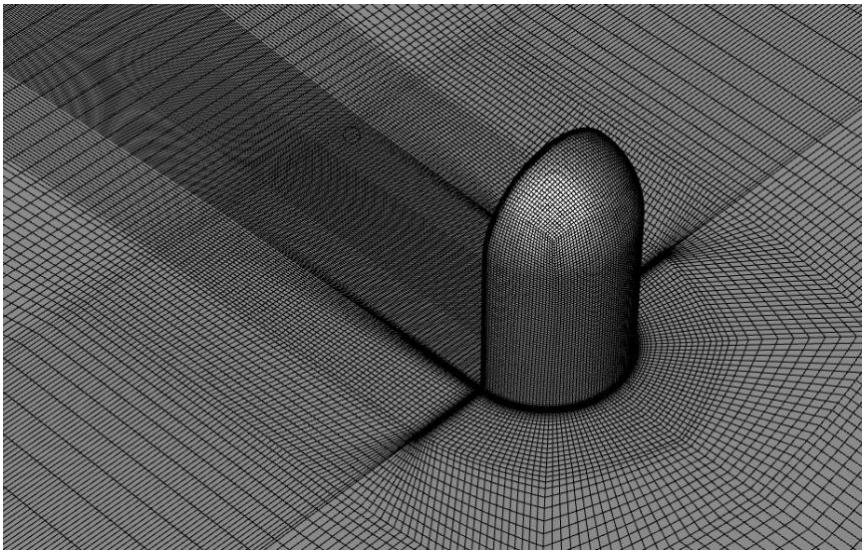

Fig. 3. An overview of the structured grid on both the mirror and the plate used in this study (Courtesy of ANSYS Inc.). The structured grid details are identical to the previous works of Egorov *et al.*[21] *and* Belamri *et al*.[17]

For the grid evaluation study on the poly-hex core grid, the surface sizes on the mirror are determined based on the wall-normalised unit methodology presented for the SBES turbulence model by Chode *et al.*[37] The wall-normal units for all the meshes investigated in this study have $\Delta y^+ < 1$. Local mesh refinement is used to control the mesh in the vicinity of the mirror, as shown in Fig. 4. For the grid evaluation study, the wall-normalised unit Δy^+ was

ensured to be < 1, whereas the surface size on the HRM and the freestream gradually reduced. Table 1 summarises the mesh sizes used for all the grids presented in this study. For the fine grid, a spatial resolution of a minimum of 0.02D is used for the local refinement in the wake of the mirror, which corresponds to approximately 22 Points Per Wave ($PPW = c/f_{max}.\Delta x$) for a 4 kHz acoustic wave. The PPW is consistent and at instances offer better resolution compared to the previously published numerical studies on HRM with other hybrid RANS/LES cases.[5,14,16–18,22]

Table 1

Comparison of mesh resolution used in the current study

Cases	Δx^+	Δy^+	Δz^+	PPW	Cell Count
Coarse Grid	360-680	< 1	360-680	7	0.85 x 10^6
Medium grid	120-520	< 1	120-520	10	3.42 x 10^6
Fine grid	120-320	< 1	120-320	22	6.86 x 10^6

All the cases investigated in the present work are numerically solved using ANSYS Fluent version 2020 R2. A pressure-based transient solver with a SIMPLE scheme for the pressure-velocity coupling is used for all the cases investigated. For spatial discretisation, the bounded-central differencing (BCD) scheme was used for the momentum equation, whereas the turbulent quantities such as Turbulent Kinetic Energy (TKE) and Specific Dissipation Rate (SDR) are discretised using the second-order upwind scheme. For temporal discretisation, the bounded second-order implicit formulation was applied. The transient simulation was initialised using a steady-state solution obtained from the steady $k-\omega$ SST turbulence model and then solved for 0.5s, which corresponds to ~ 97.5 convective cycles (97.5 x D/U). The last 40 convective cycles (~ 0.2s) were considered for obtaining the time-averaged statistics. A time-step of 3 x 10^{-5} s was used for all the cases investigated to ensure the convective Courant-Friedrichs-Lewy (CFL) number is less than 1. The pressure fluctuations on the mirror and the plate are recorded at every time step after flow quantities reached the asymptotic state and are later used as the input to the FW-H acoustic analogy.

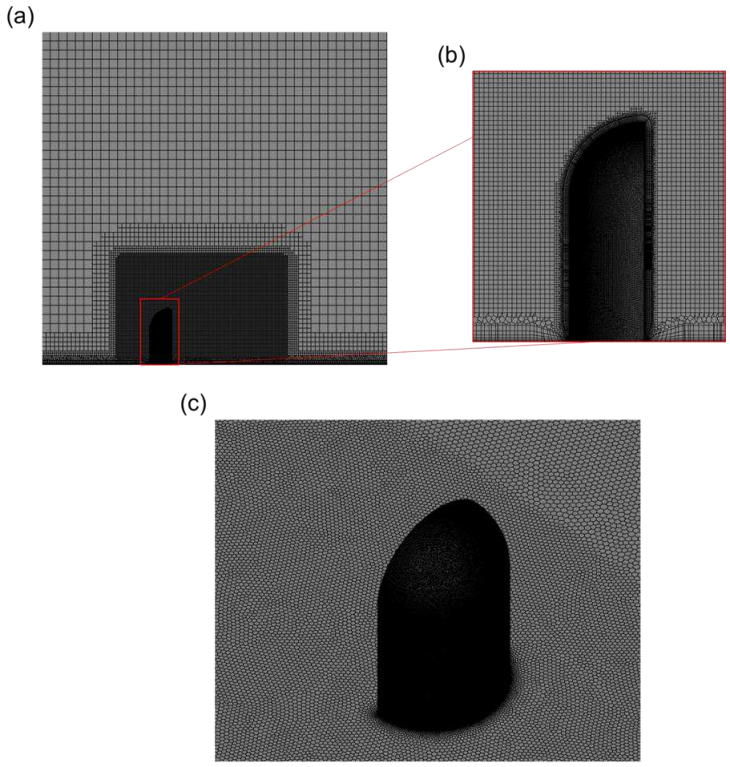

Fig. 4. Grid used for the validation study a) Overview of the grid generated for the final grid with local refinement zones, b) Detailed view of the mesh on the mirror and its vicinity, and c) Isometric view of the cells on the surface of the mirror and the plate.

C. Grid Evaluation Study

Three poly-hex core grids were generated by gradually varying grid sizes to assess the grid convergence, and the grid sizes are summarised in Table 1. As seen in Table 2, the drag coefficient predicted by the three grids lies well within the range of the drag values predicted by the other numerical studies. The difference in the predicted value of C_D is < 1% amongst the grids that have been investigated. A comparison is drawn between the predicted coefficient of pressure evaluated at several sensor locations on the mirror surface and the hydrodynamic pressure fluctuations (HPF) obtained from sensors placed on both the plate and the mirror (Ref: Table A1 from Appendix). The HPF spectra obtained from the sensor s112 and s120 indicate that the cut-off frequency is higher for the fine grid than the other two grids, as indicated by solid lines in Fig. 5(b). The mesh cut-off frequency is estimated as $f_{mc} = \sqrt{2\langle k \rangle/3}/(2\Delta_c)$

where $\langle k \rangle$ is the time-averaged turbulence kinetic energy and Δ_c represents the length of the cell.[26] The *Cp* predicted using fine mesh indicates the flow is more attached at the front edge than the other two grids. At the centreline on the mirror, as shown in Fig. 5(a), the *Cp* predicted by the coarse grid at s16 is 9.14% lower than s20, whereas the medium and fine grid show a maximum difference of < 3% between *Cp* predicted at s16 and s20. At sensor s32, the coarse grid predicts a lower *Cp* by 11% compared to both the medium and the fine grid. Owing to several comparisons that appear more reasonable with the fine grid, fine grid sizes were used for the rest of the HRM analysis.

Table 2
Comparison of the Drag Coefficient predicted in the present cases against several published numerical results

Published cases	**C_D**	**Present Cases**	**C_D**
Ask and Davidson[16] – LES	0.475	Coarse Grid (Poly-hex Core)	0.474
Capizzano *et al.*[18] – X-LES	0.440	Medium Grid (Poly-hex Core)	0.469
Tosh *et al.*[29]– DES	0.489	Fine Grid (Poly-hex Core)	0.472
Yu *et al.*[22] – DDES	0.445	Structured Grid	0.491
Ask and Davidson[16] – DES	0.425		
Chen and Li[28] – DES	0.489		
Chen and Li[28] – DDES	0.478		

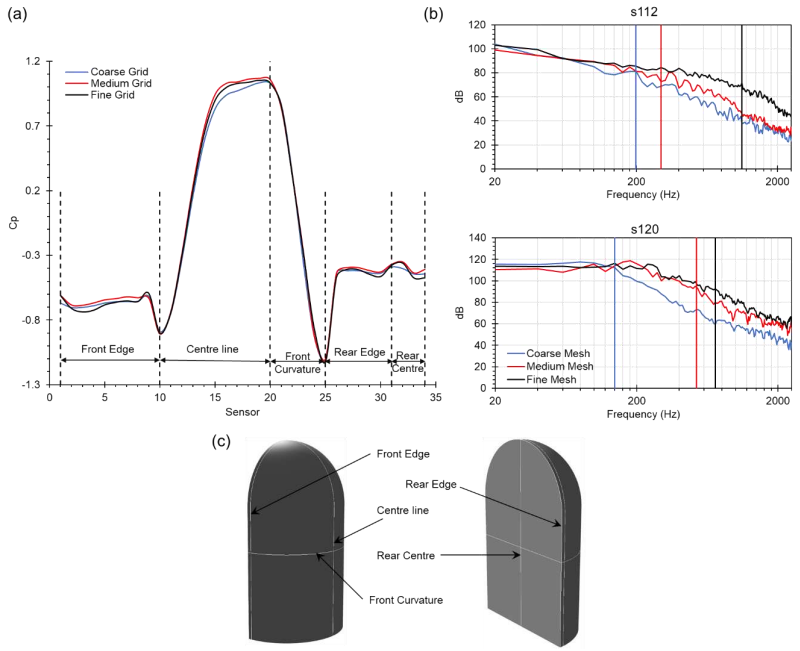

Fig. 5. Comparison of a) the time-averaged Pressure Coefficient (c_p) on the surface of the mirror, b) Hydrodynamic pressure fluctuations (HPF) extracted at two different sensor positions, s112 on the mirror and s120 on the plate. and c) schematic of the location of the sensor placed on the mirror. Solid vertical lines represent the mesh cut-off frequencies.

D. Validation and Verification study

The time-averaged pressure coefficient predicted by SBES with poly-hex core grid at several locations on the mirror (See Fig. 6(b)) is in reasonable agreement with both experimental and numerical results, as seen in Fig. 6(a). The *Cp* predicted by the SBES with the poly-hex core grid on the front edge is lower than the measured *Cp* at the front edge, the *Cp* value predicted by sensor s3 being the lowest. At sensors s10 and s25, the experimental results indicate the flow is separated, while the prediction from SBES with the poly-hex core grid predicts a lower *Cp* value indicating that the flow is attached. Overall, the SBES prediction closely matches the *Cp* values predicted by other published numerical results.[14,16,17,23,28] However, the *Cp* predicted on the centreline of HRM is higher than the measured *Cp* by 2.8%, indicating the flow separation on the centreline is less well predicted by SBES. At the rear centre and rear edge of the HRM, SBES prediction agrees closely with the experiment results and the published numerical results. The over-prediction of *Cp* on the front end and the centre line in Fig. 6(a) and the wall shear stress on the HRM (See: Fig. 7) indicate a delayed

separation. The upstream separation line observed in the experiment is located at 0.15D from the trailing edge of the mirror, whereas the predicted separation line is located at 0.0625D from the trailing edge for the results obtained from SBES with poly-hex core grid. This delay in the separation is likely due to the excessive production of turbulence on the front face of HRM, which prevents the flow from separation, as seen in Fig. 8. A similar observation is made by Ask and Davidson[16,23], Capizzano *et al.*[18], Rung *et al.*[14], and Yu *et al.*[22] for their numerical results.

The formation of a horseshoe vortex upstream of the mirror results from flow stagnation at the front of the mirror. The size of the horseshoe vortex is defined as L_{hx} in streamwise, L_{hz} in the spanwise direction, respectively, in Fig. 9. The flow separated from the mirror results in the formation of a large recirculation bubble behind the mirror, which impinges on the plate at a distance of 2.59D from the mirrors trailing edge, as indicated by L_{ws}. These distances are measured on the surface generated at the height of 0.01D above the plate and compared against other published numerical results as the experimental data is not available in Table 4. The horseshoe vortex predicted by the SBES is wider by 14% and 10% compared to the width predicted by LES presented by Ask and Davidson[16] and DDES presented by Chen and Li.[28] The horseshoe vortex interacts with the vortex generated from the trailing edge of the mirror and exerts pressure fluctuations on the plate and the mirror.

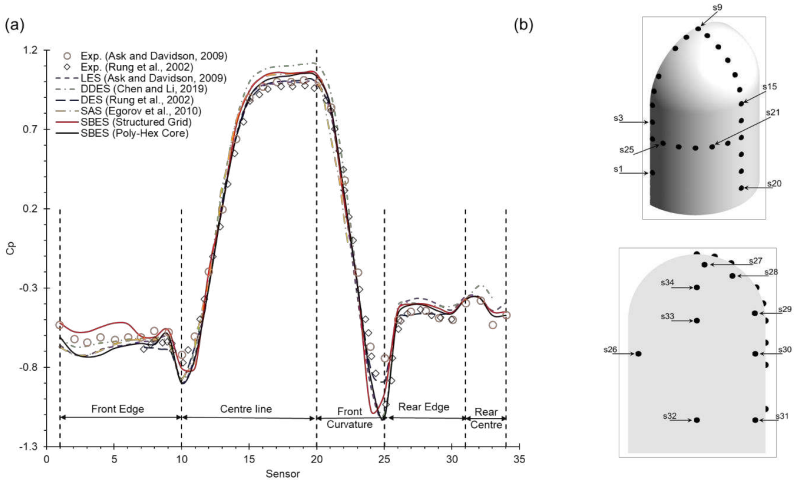

Fig. 6. a) Comparing the time-averaged pressure coefficient (c_p) on the surface of the mirror generated at 34 sensors is compared against experimental data[14,16] and published numerical results[14,16,21,28] and b) a schematic of the HRM with all the 34 sensors used to measure the pressure coefficient (Ref: Table 8 in Appendix A for the cartesian coordinates of the sensor locations).

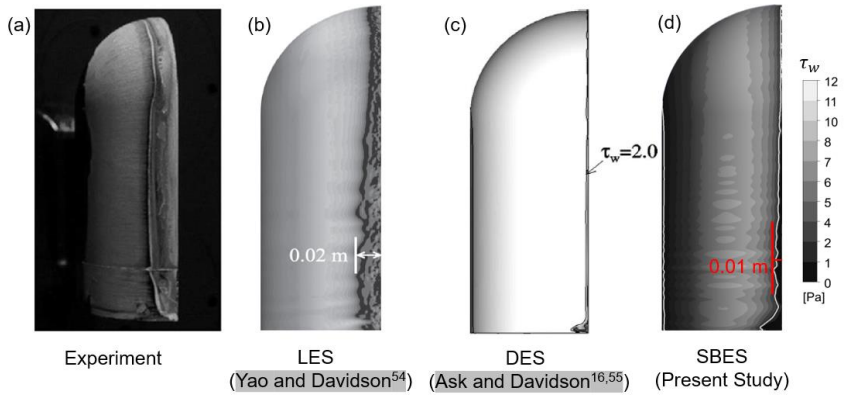

Fig. 7. Comparison of wall shear stresses predicted on the surface of the mirror by SBES against both Numerical and experiment results. a) Experimental results obtained by Daimler Chrysler, demonstrated by Ask and Davidson.[16] Reproduced with permission from J. Ask and L. Davidson, "A numerical investigation of the flow past a generic side mirror and its impact on sound generation," J. Fluids. Eng. Trans. 131, 0621011 (2009). Copyright 2009 ASME International. b) LES.[54] Reproduced from H.-D. Yao and L. Davidson, "Vibro-acoustics response of a simplified glass window excited by the turbulent wake of a quarter-spherocylinder body," J. Acoust. Soc. Am. 145, 3163 (2019). with the permission of AIP Publishing. c) DES.[16,55] Reproduced with permission from J. Ask and L. Davidson, "A numerical investigation of the flow past a generic side mirror and its impact on sound generation," J. Fluids. Eng. Trans. 131, 0621011 (2009). Copyright 2009 ASME International. d) SBES (Present Study). The solid white line shown in SBES (Present Study) indicates the value of τ_w = 2 pa.

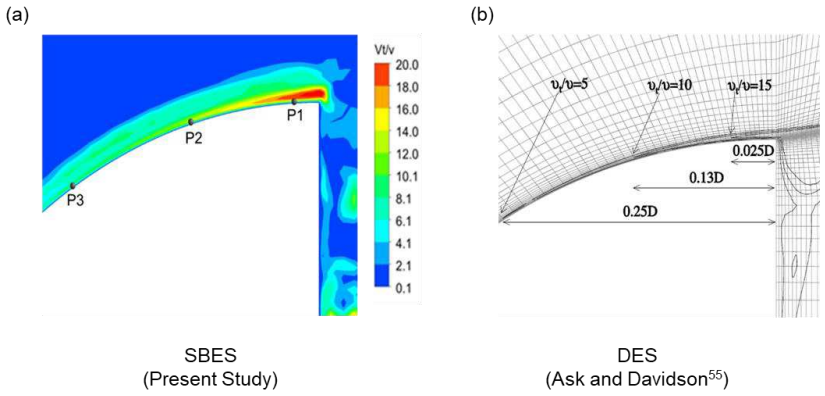

Fig. 8. Comparison of Turbulent Viscosity Ratio (TVR) predicted by a) SBES against b) DES.[55] P1, P2 and P3 here represent the probe position used for measurement.

Table 3
Comparison of Turbulent Viscosity Ratio (TVR) predicted by SBES against DES[21]

Probe location	SBES (Present Study)	DES[55]
P1	7.35	15
P2	11.44	10
P3	7.61	5

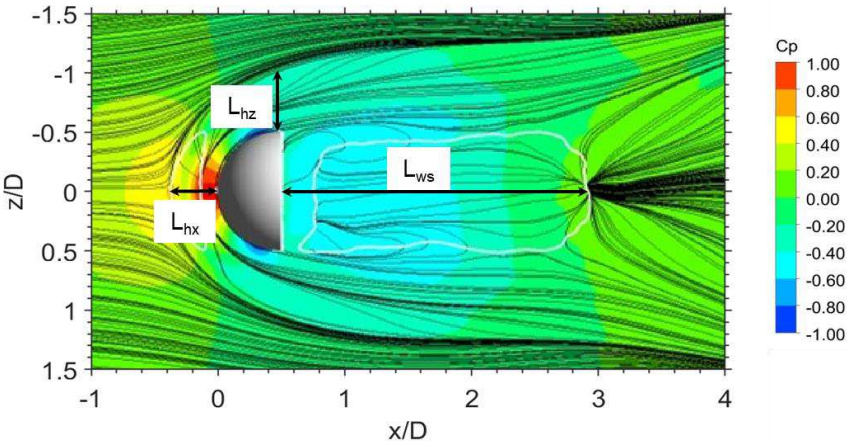

Fig. 9. Dominant Flow patterns around the HRM generated on the plane y = 0.01D and coloured with Mean Pressure Coefficient. L_{hx}, L_{hz} and L_{ws} represent the normalised length of the horseshoe vortex from the mirror in the streamwise direction, the normalised height of the horseshoe vortex from the lateral edge of the mirror, and the normalised length of the wake structure measured from the rear face of the mirror, respectively.

Table 4
Normalised lengths of the time-averaged flow features compared against published numerical results.

Case	Solver	L_{hx}	L_{ws}	L_{hz}
Belamri *et al.*[17]	SAS	-	$3D - 4D$	-
Ask and Davidson[16]	LES	$0.26D$	$2.58D$	$0.45D$
Chen and Li[28]	DES	$0.27D$	$3.25D$	$0.40D$
Chen and Li[28]	DDES	$0.27D$	$2.66D$	$0.43D$
Present Study	SBES	$0.30D$	$2.59D$	$0.42D$

The exerted pressure fluctuations recorded at two sensors located on the mirror (s111 and s113) and at four sensors located on the plate (s119, s121, s122 and s123) are computed using

$HPF = 10\log_{10}\frac{p^*}{p_{ref}^2}$. p^* is the power spectral density of the fluctuation pressure, and P_{ref} is the reference pressure and taken as 2 x 10^{-5} Pa. The coordinates of these sensors are shared within the supplementary data.

Pressure spectra generated at s111 and s113 (Fig. 10) indicate lower dB levels by 9.7% and 9.3%, respectively, compared to experimental spectra in the low-frequency range (f <100 Hz). At the mid frequencies range (100 < f < 500 Hz), the intensity levels were 4.5% and 5% lower for the two sensors, and a similar difference in the intensity levels can be found in the high-frequency range (500 < f < 1000 Hz). For frequencies ($f \geq 1000$ Hz), the predicted SBES spectra decay rapidly and deviate considerably from the experimental data, as seen in Fig. 10.

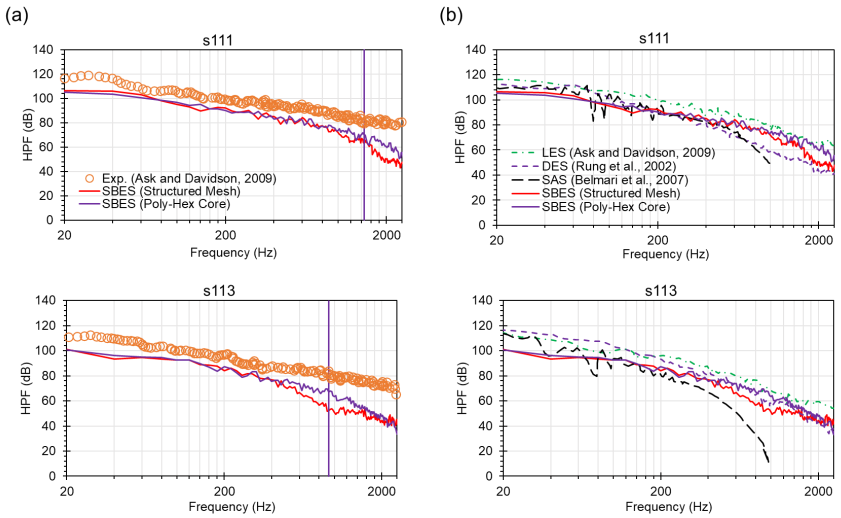

Fig. 10. Hydrodynamic pressure fluctuations extracted at two different sensors on the mirror s111 and s113 (Ref: Table 9 in Appendix A for cartesian coordinates of the sensor locations) a) shows a comparison between the predicted HPF by the structured grid and the poly-hex core grid using SBES against the experiment data[16] and b) the SBES predictions compared against other previously published numerical data.[14,16,17] Solid vertical lines represent the mesh cut-off frequency for the poly-hex core grid.

The HPF spectra obtained on the plate shows an overall better agreement with experimental results throughout the spectra than the HPFs obtained on the mirror. The HPF spectra from experiments at sensors located on the plate predict a peak frequency at ~38 Hz, which corresponds to the Strouhal frequency of St = 0.19 ($St = fD/U$), the vortex shedding frequency for HRM.[14,16] This peak frequency is more evident in the sensors located downstream, such as s121 – s123 in the wake, as seen in Fig. 11. At s119, no distinct peak is observed at 40Hz, both in the experimental and predicted data. Whereas at s121 and s122, there

is no distinct peak seen in the predicted spectra by SBES. The SBES predicts a distinct peak with the structured grid at s123.

Table 5
Comparison of mesh cut-off frequencies between the grid settings employed in the present study against several previously published numerical works

Sensor Location	Poly-hex Core SBES	Ask and Davidson[16] DES	Capizzano *et al.*[18] X-LES	Yao and Davidson[5] LES
	f_{max}	f_{max}	f_{max}	f_{max}
s111	1451	267	-	583
s114	1378	260	-	-
s119	620	425	550	684
s121	1020	492	781	-
s122	1248	533	919	-
s123	1460	606	510	1314

The maximum resolved frequency of the grid at the sensor location can be evaluated by estimating the cut-off frequency using the turbulence quantities. The cut-off frequency calculated for the SBES is higher than the DES for all the sensors reported in this study, as shown in Table 5. The pressure fluctuations on the plate and mirror are the source for producing noise, and this noise propagates within the domain. The propagated noise is evaluated at five different microphone locations using the FW-H acoustic analogy from the pressure fluctuations recorded at every frequency, and sound pressure level (SPL) computed at five microphone locations are shown in Fig. 12.

The SPL predicted by SBES with both poly-hex core and structured grid shows a good agreement in the trend compared with the measured data, as shown in Fig. 12. At M1 located in the mirror upstream, a maximum of 4 dB and 8 dB difference is observed at low-frequency for both the poly-hex core grid and the structured grid. A maximum difference of 1–2 dB difference is seen in the mid and the high-frequency ranges between SPL spectra predicted by the structured and the poly-hex core grids. The SPL spectra predicted by the structured grid at M4 over predicts the SPL intensity compared to measured data, while the poly-hex core grid agrees well with the intensity in measured spectra.[24] At the high-frequency range, the prediction from both the grids give a maximum difference of 8–9 dB from experimental data, and this difference in the predicted spectra is consistent with the other numerical results published by Ask and Davidson[23,24] and Caraeni *et al.*[19]At M10 and M11, the predicted SPL is in good agreement with the measured data throughout the SPL spectra, as shown in Fig. 12.

At M14, as shown in Fig. 12, the pressure spectra predicted by both the structured and poly-hex core grids indicate lower intensity levels than the measured spectra considering that the mesh is less refined in this region, and therefore the acoustic frequencies appear to be less resolved.

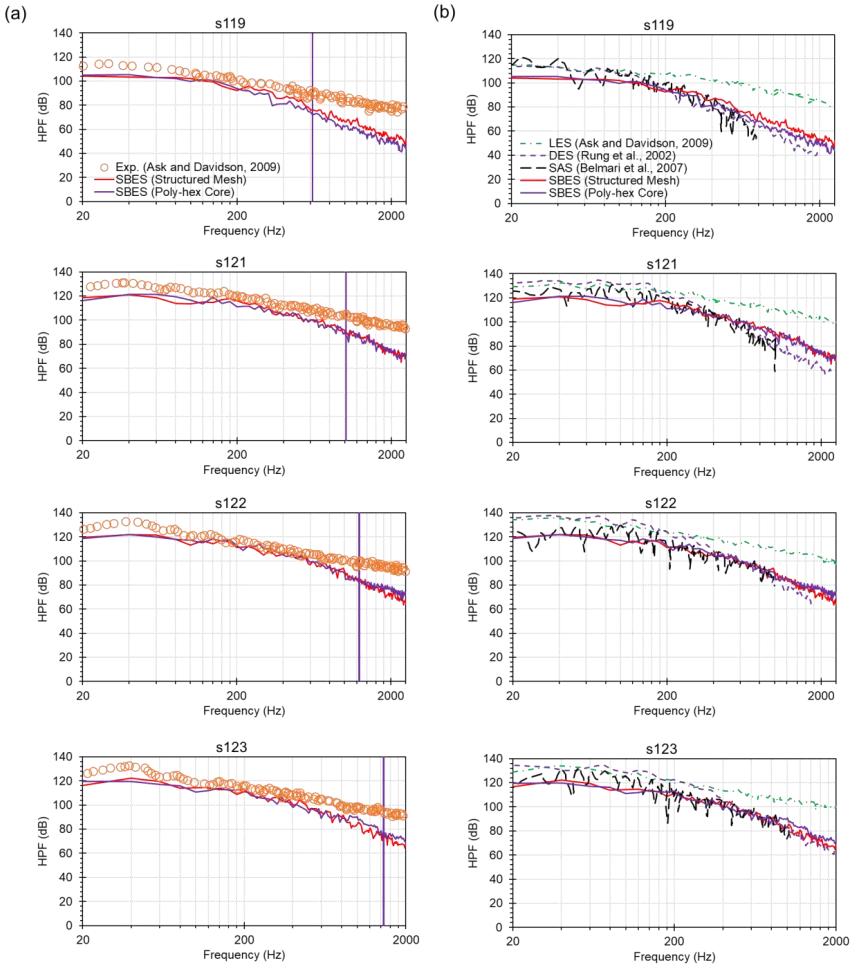

Fig. 11. Hydrodynamic pressure fluctuations extracted at four different sensors on the plate – s119, s121, s122, and s123 (Ref: Table 9 in Appendix A for cartesian coordinates of the sensor locations) a) shows a comparison between the predicted HPF by the structured grid and the poly-hex core grid against the experiment data[16] and b) the SBES predictions compared against other previously published numerical data.[14,16,17] Solid vertical lines represent the mesh cut-off frequency for the poly-hex core grid.

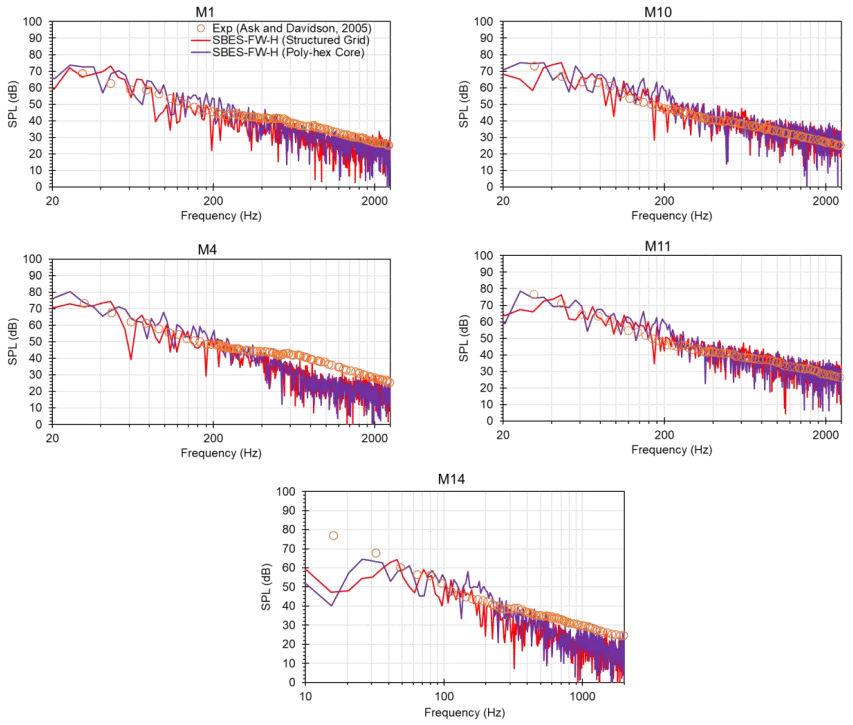

Fig. 12. Noise generation evaluated using the FW-H acoustic analogy at five different microphone positions - M1, M4, M10, M11 and M14, are compared against microphone data obtained from the experiments.[23] (Ref: Table 10 in Appendix A for cartesian coordinates of the locations of the microphones).

1. A comparison between the surface integral methods used for predicting the induced noise:

The intensity of sound propagated was evaluated at several microphone locations using the FW-H acoustic analogy. However, the propagation of acoustic waves in time and space for the entire domain or zone of interest can also be determined using Acoustic Perturbation Equations (APE). In this study, APE is used to verify the compatibility of the grid size used by solving Kirchhoff's surface integral (KI) method to determine sound intensity at the same locations where the FW-H analogy was computed by using the sound pressure p' obtained from the APE to obtain pressure signal at the receiver using the KI surface integral equation as shown in Eq. 21

$$p_r'(t) = \frac{1}{4\pi}\oint\left[\left(\frac{1}{cr}\frac{\partial p_s'(t)}{\partial t} + \frac{p_s'(t)}{r^2}\right)\frac{\partial r}{\partial n} - \frac{1}{r}\frac{\partial p_s'(t)}{\partial n}\right]_{tret} ds \tag{21}$$

Here, p'_r is the acoustic pressure evaluated at the non-moving receiver, located at a distance of r from the selected sound source surface (s). n denotes the vector normal to the surface, and t_{ret} represents the retarded time defined by $t_{ret} = t - c/r$. The sound source in the present study is the mirror surface, and the normal pressure gradient on the mirror surface is equal to zero. Thus Eq. 21 can be reduced to:

$$p'_r(t) = \frac{1}{4\pi}\oint\left[\left(\frac{1}{cr}\frac{\partial p'_s(t)}{\partial t} + \frac{p'_s(t)}{r^2}\right)\frac{\partial r}{\partial n}\right]ds \tag{22}$$

Due to the APE being solved for an entire computational domain in space, any abrupt changes or non-uniformities in the mesh can lead to an erroneous APE solution.[29,56] Therefore, in this study, the APE was only solved with the structured grid. The results obtained from KI and FW-H for the structured grid were compared against the FW-H obtained from the poly-hex core grid at M10, as shown in Fig. 13. The SPL obtained from the FW-H method for both structured and poly-hex core agree reasonably in the mid and high-frequency ranges. However, the KI predicts lower dB values in SPL at the low-frequency range (f < 100 Hz). These differences could possibly be attributed to a) the structured grid requiring a more stringent resolution for the SBES-KI approach and b) the inherent formulation of KI, wherein the nonlinear terms are weaker, unlike the FW-H formulation, which takes the nonlinear effects fully into account.[57]

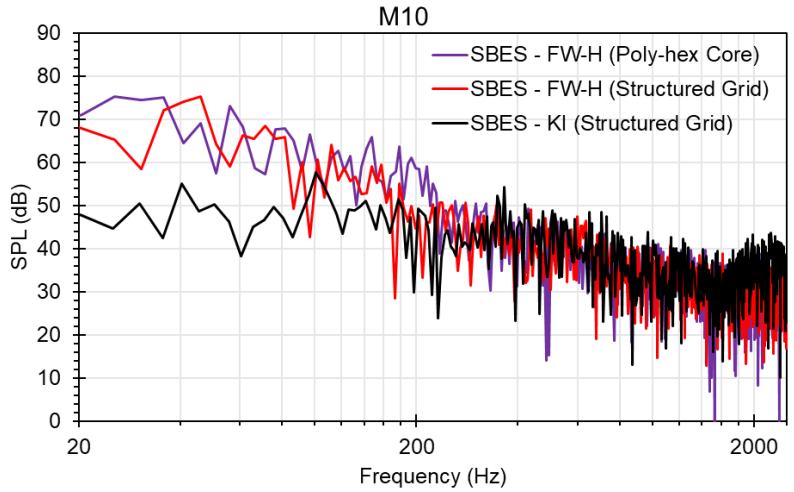

Fig. 13. Comparison between the SPL predicted at M10 using the SBES-FW-H approach with the structured grid, the SBES – KI approach with the structured grid and the SBES-FW-H approach with the Poly-hex core grid used in the study.

Considering that the overall match between the SBES-FW-H approach using the poly-hex core (fine) mesh and experimental data is in good agreement, the SBES-FW-H framework is used throughout the rest of the paper.

IV. EFFECT OF ASPECT RATIO (*AR*) ON FLOW AND NOISE RADIATED BY HRM

In this study, the aspect ratio (*AR*) is defined as *h*/*D*, where *h* is the height of the mirror and *D* is the diameter of the mirror, which is kept constant for all of the *AR* cases. A series of aspect ratios are taken into account, ranging from 1 to 2.5, as seen in Fig. 1(b). The size of the recirculation bubble formed behind the mirror increased in both streamwise and normal directions with an increase in *AR*, as seen in the streamline plots shown in Fig. 14. The smallest size of the recirculation bubble is seen for *AR* = 1, and the centre of the recirculation bubble (*e*) for *AR* = 1 is farthest in the streamwise direction while closest to the plate in the normal direction. The distance measured from the mirrors rear surface to *e* reduced with increasing *AR* until *AR* = 1.5. A further increase in *AR* increases the distance measured from the mirrors rear surface to *e* in the streamwise (*x)* direction. In the normal (*y*) direction, an increase in the *AR* increases the distance between the plate and *e*. The location of *e* in cartesian coordinates is tabulated in Table 6 for all the *AR* cases investigated.

Table 6
Comparison of the change in the centre of recirculation bubble (*e*) and the normalised lengths of the time-averaged flow features with the change in *AR*

Coordinates	***AR* = 1**	***AR* = 1.25**	***AR* = 1.5**	***AR* = 2**	***AR* = 2.5**
x/D	1.2	1.07	1.01	1.085	1.12
y/D	0.62	0.67	0.91	1.18	1.52
L_{ws}	2.36*D*	2.40*D*	2.59*D*	2.97*D*	3.26*D*
L_{hz}	0.39*D*	0.41*D*	0.42*D*	0.43*D*	0.46*D*
L_{hx}	0.27D	0.29D	0.30D	0.26D	0.27D

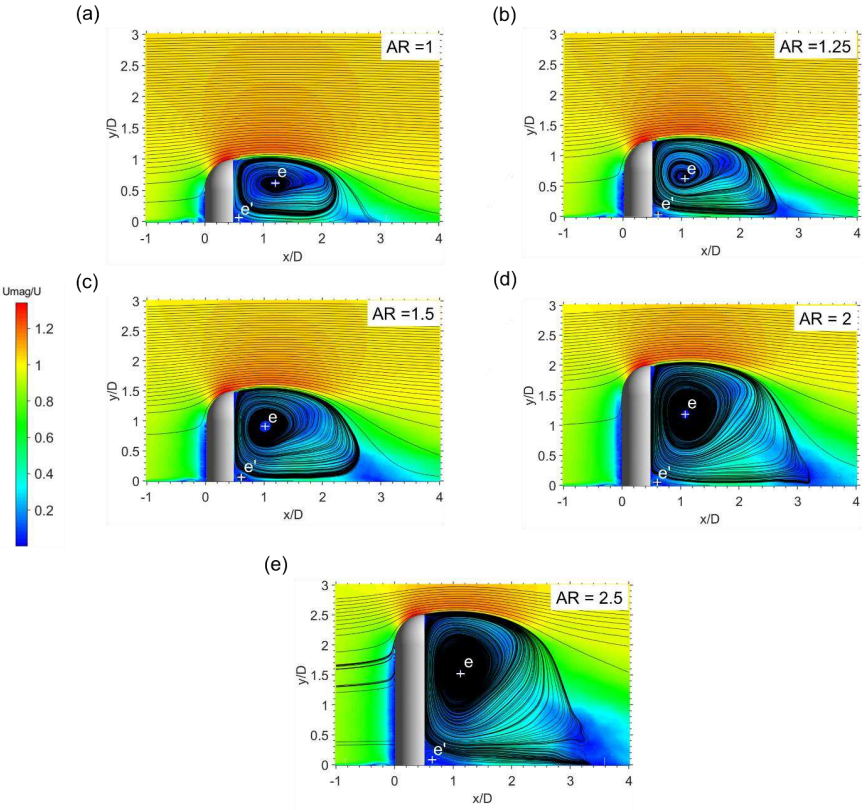

Fig. 14. Comparison of the time-averaged velocity magnitude contours superimposed with the velocity streamlines on the midplane for a) $AR = 1$, b) $AR = 1.25$, c) $AR = 1.5$, d) $AR = 2$ and e) $AR = 2.5$. e and e' represent the centre of the recirculation bubbles formed behind the mirror.

The general flow features around the HRM for all the aspect ratios can be visualised using the Q criterion in Fig. 15. The Q Criterion is defined as $Q = 0.5(\Omega_{ij}\Omega_{ij} - S_{ij}S_{ij})$, where Ω_{ij} is the rotation and S_{ij} is the strain rate. The presence of two distinct horseshoe vortices can be observed upstream of the mirror as indicated by h_a and h_b shown in Fig. 15. DeVilliers[20] also reported the presence of these horseshoe vortex upstream of the mirror. The flow structures that develop upstream show a negligible change with an increase in AR.

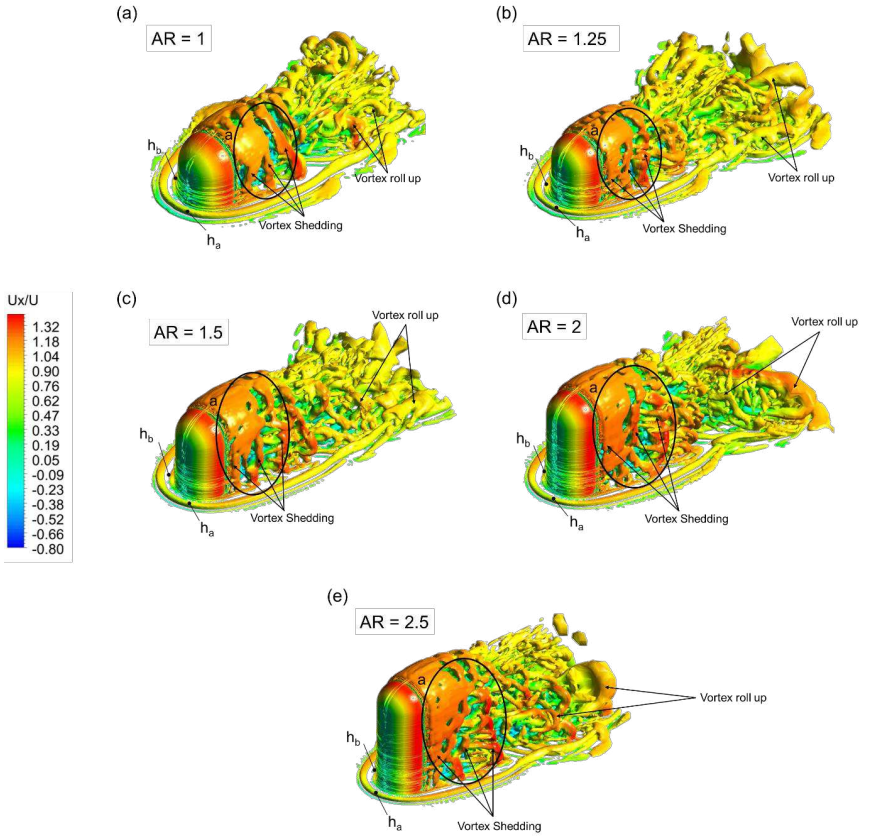

Fig. 15. Comparison of the vortical structures of an instantaneous flow field visualised by iso-surfaces of $Q = 10^3$ s^{-2} coloured with instantaneous x-velocity for all the investigated cases a) $AR = 1$, b) $AR = 1.25$, c) $AR = 1.5$, d) $AR = 2$ and e) $AR = 2.5$.

The flow separation is evident from the lateral edges of the mirror for all the aspect ratio, which evolves into a vortex shedding indicated by the arrows in Fig. 15. The coherent structure of the instantaneous flow field shown in Fig. 15 suggests that the near-wake region represented by a, increase with an increase in AR. This finding is substantiated by Fig. 14 wherein, the length of the separation bubble and the width of the horseshoe vortex (time-averaged) appears to increase with AR. A quantitative comparison of the normalised length (L_{ws}) and the width of the horseshoe vortex (L_{hz}) of the time-averaged wake for all values of AR are presented in Table 6. The horseshoe vortex traversing downstream interacts with the shed vortices that tend to roll up into the wake. The roll-up of the vortices shown in Fig. 15 increases with an increase in the AR. These flow features induce pressure fluctuations on the plate, and these pressure

fluctuations are visualised using normalised pressure fluctuations $NPrms = prms/(0.5\rho U_\infty^2)$ in Fig. 16. The *NPrms* on the plate shown in Fig. 16 shows two distinct pressure zones P_u and P_d formed due to the lateral vortices seen in the region *a* from Fig. 15. The intensity levels at both pressure zones P_u and P_d increase with an increase in *AR*. The intensity levels predicted at P_u is ~ 4% higher than the intensity levels reported at P_d for *AR* = 1.5, 2 and 2.5, respectively. This difference in the pressure fluctuations zones is consistent with observations made by Yu *et al.*[22] The size of the pressure zones also increases with an increase in the *AR*, as shown in Fig. 16.

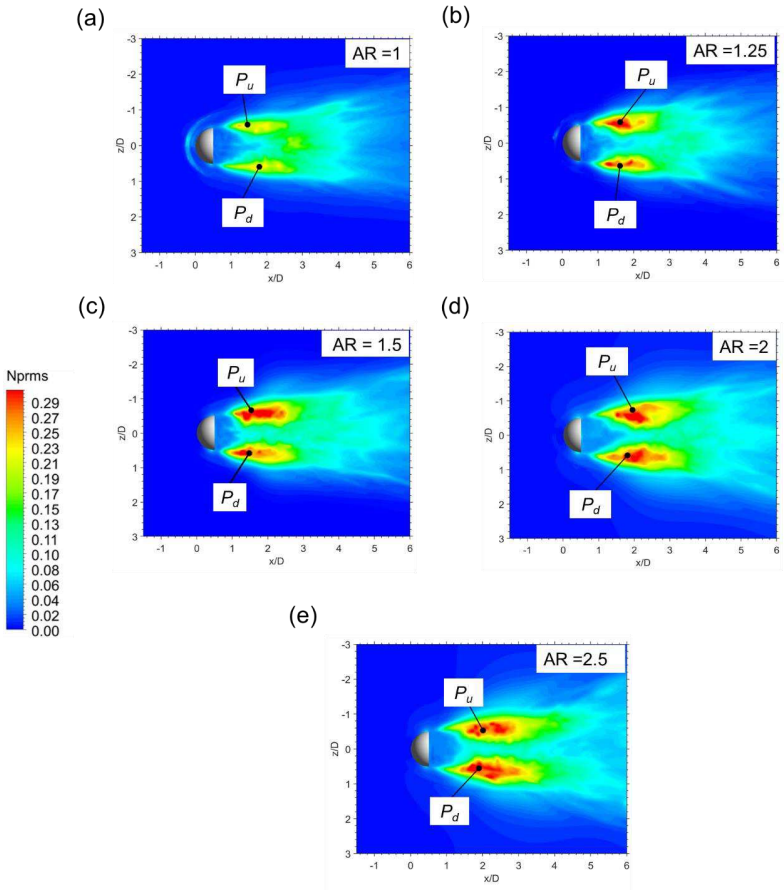

Fig. 16. Comparison of the normalised pressure fluctuations on the plate between a) *AR* = 1, b) *AR* = 1.25, c) *AR* = 1.5, d) *AR* = 2 and e) *AR* = 2.5. Here, P_u and P_d indicate the pressure regions formed due to the interaction of the lateral vortices with the plate.

The trend in pressure fluctuations generated on the mirror and closer to the plate at s111 and s113 indicates the intensity levels are lower for *AR* = 2.5. However, moving downstream, the intensity of the hydrodynamic pressure fluctuations increases for *AR* = 2.5, as shown in Fig. 18. This trend agrees well with the overall pressure distribution on the plate, as shown in Fig.16. The microphone data shown in Fig. 19 for *AR* = 2.5 show a distinct peak at ~36Hz in the frequency spectra plotted for all the microphone locations, while no such peaks are predicted in other *AR* cases.

The distribution of hydrodynamic pressure spectra (HPS) is analysed by plotting the real part of pressure fluctuations obtained from both the mirror and the plate using Fast Fourier Transform (FFT) shown in Fig. 20. Closer to the vortex shedding frequency viz. at 40Hz, stronger harmonics are predicted on the plate. However, the harmonics tend to dampen with the increase in frequency for all the *AR* cases presented, which supports the observations made in Fig.18 for individual sensor positions placed on the plate. Further, for *AR* =1 and 1.25, the distribution of the harmonics presented by the HPS are smaller compared to *AR* =1.5, and with an increase in *AR*, the intensity levels of the hydrodynamic pressure tend to increase.

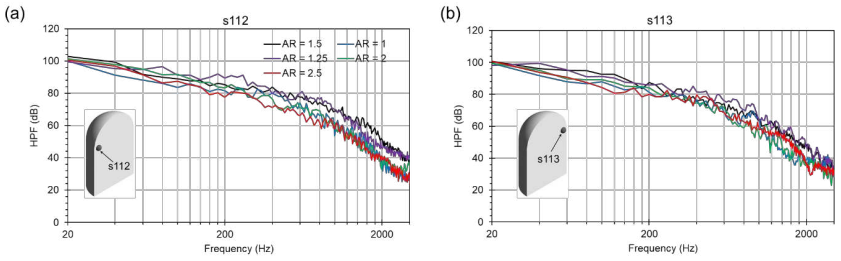

Fig. 17. Comparison of the hydrodynamic pressure fluctuations extracted on the mirror at a) s112 and b) s113 between *AR* = 1, 1.25, 1.5, 2 and 2.5. The location of the sensors is indicated within each figure.

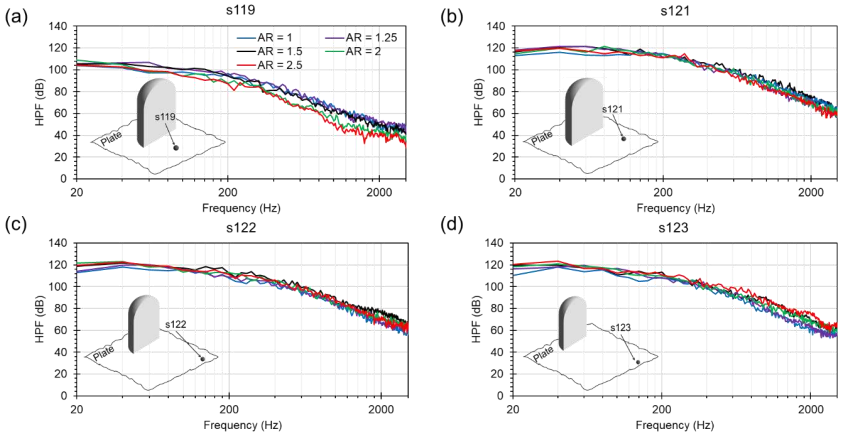

Fig. 18. Comparison of the hydrodynamic pressure fluctuations extracted on the mirror at a) s119, b) s121, c) s122 and d) s123 between AR = 1, 1.25, 1.5, 2 and 2.5. The location of the sensors is indicated within each figure.

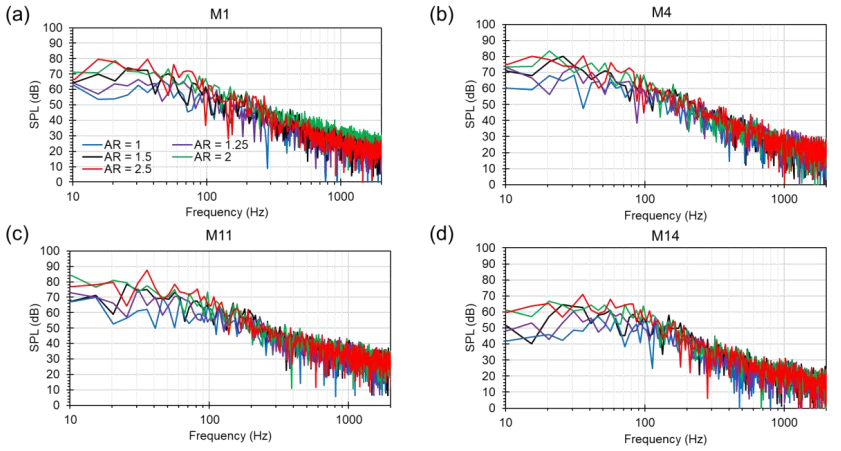

Fig. 19. Comparison of the sound pressure level extracted at four microphone locations: a) M1, b) M4, c) M10, and d) M14 between AR = 1, 1.25, 1.5, 2 and 2.5.

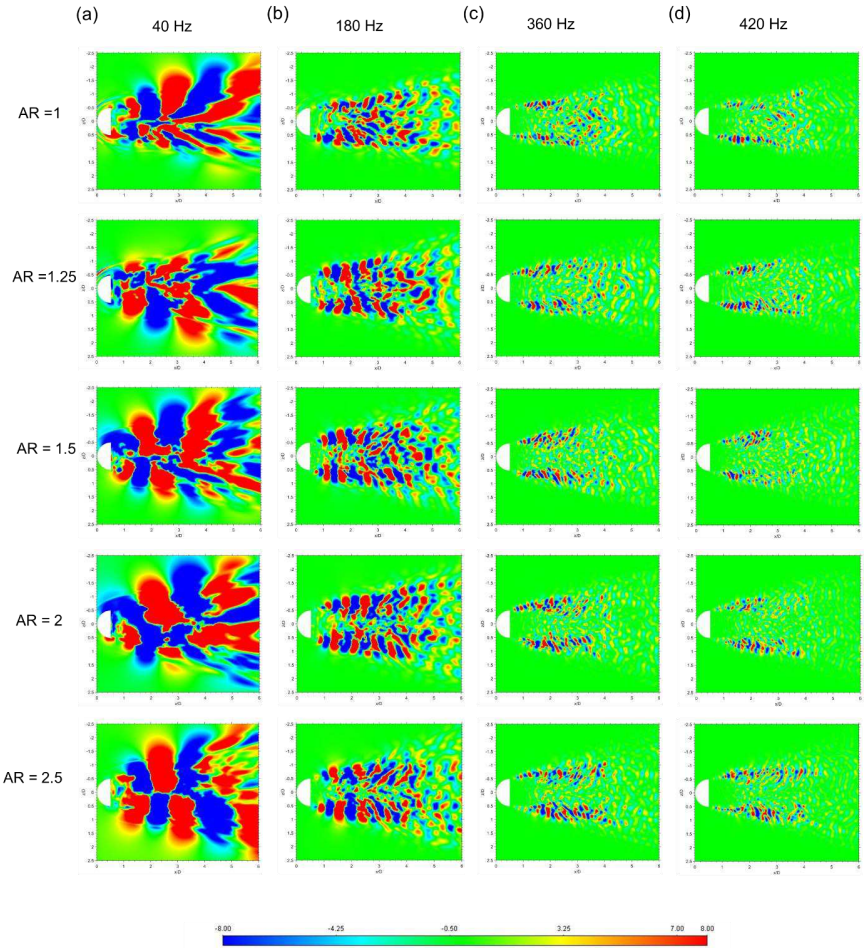

Fig. 20. Comparison of the real part of the Hydrodynamic Pressure Spectra (HPS) generated on the plate between AR = 1, 1.25, 1.5, 2 and 2.5 investigated at a) 40 Hz, b) 180 Hz, c) 360 Hz, and d) 420 Hz.

The structure of the emitted noise is identified by plotting directivity using the Overall Sound Pressure Level (OASPL) at two planes, $y = 0.25D$ and $y = 2D$, as shown in Fig. 21. Each plane consists of 36 microphones placed in a circular array around the mirror, as illustrated in Fig. 21(c). The structure of the emitted noise at $y = 0.25D$ is dipole-like, indicating that the induced noise has contributions from both the plate and the mirror. On the other hand, at $y = 2D$, the directivity plot shows a monopole-like structure. A decrease or increase in the AR indicates a negligible change in the overall structure of the emitted noise at both planes. From

the perspective of a standard mirror with $AR = 1.5$, the numerical results predict that an increase in AR tends to increase the radiated noise, whereas a reduction in AR tends to reduce the same.

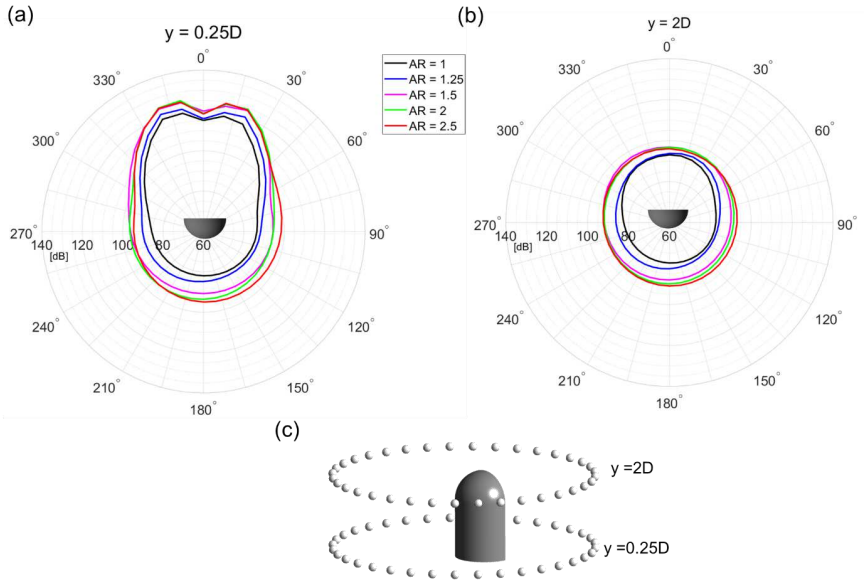

Fig. 21. The overall sound pressure level extracted at 36 microphones placed in a circular array at planes a) $y = 0.25D$ and b) $y = 2D$ plate are compared for $AR = 1$, 1.25, 1.5, 2 and 2.5 investigated, and c) illustrates the layout of the sensors located around the mirror at two different heights.

In the forthcoming sections, this work is extended by subjecting the HRM to different sweep angles, as realistic vehicle mirrors are inclined towards the side window.

V. EFFECT OF SWEEP ANGLE (θ) ON FLOW AND NOISE RADIATED BY HRM

The HRM is swept towards the plate to make a series of swept cases with 8° increments. The maximum sweep angle (θ) used in this study is 32°. For $\theta = 0°$ and 8°, the flow separates from the lateral edges of the HRM, as seen in Fig. 22 (a, b), whereas the flow separates from the top of the HRM for the $\theta = 16°$, 24° and 32° cases as shown in Fig. 22(c–d). The streamwise length of the separated flow from the upper trailing edge of the HRM increases for 24° and 32° compared to $\theta = 16°$. In Fig. 23, the centre of the recirculation bubble (e) tends to transverse downstream in a streamwise direction and decreases in the normal direction with an increase in θ. The location of the centre of the recirculation bubble for all θ is tabulated in Table 7. The

length of the recirculation bubble formed behind the HRM reduces with the change in θ, and the width of the horseshoe vortex reduces with an increase in θ, as indicated by L_{ws} and L_{hx}, respectively shown in Table 7. As a result, a change in reattachment location can be observed with a change in θ, as shown in Fig. 23.

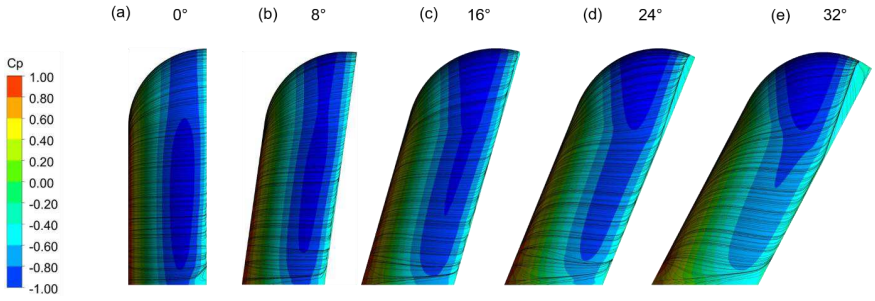

Fig. 22. Comparison of the flow separation between a) θ = 0°, b) θ = 8°, c) θ = 16°, d) θ = 24°, and θ = 32° represented by friction lines superimposed on the contours of time-averaged pressure coefficient.

Table 7
Comparison of the change in the centre of recirculation bubble (e) and the normalised lengths of time-averaged flow features with the change in θ

Coordinates	**0°**	**8°**	**16°**	**24°**	**32°**
x/D	1.01	1.105	1.23	1.305	1.455
y/D	0.91	0.78	0.72	0.65	0.55
L_{hx}	0.30D	0.28D	0.21D	0.18D	0.13D
L_{hz}	0.42D	0.41D	0.40D	0.38D	0.34D
L_{ws}	2.59D	2.56D	2.39D	2.38D	2.36D

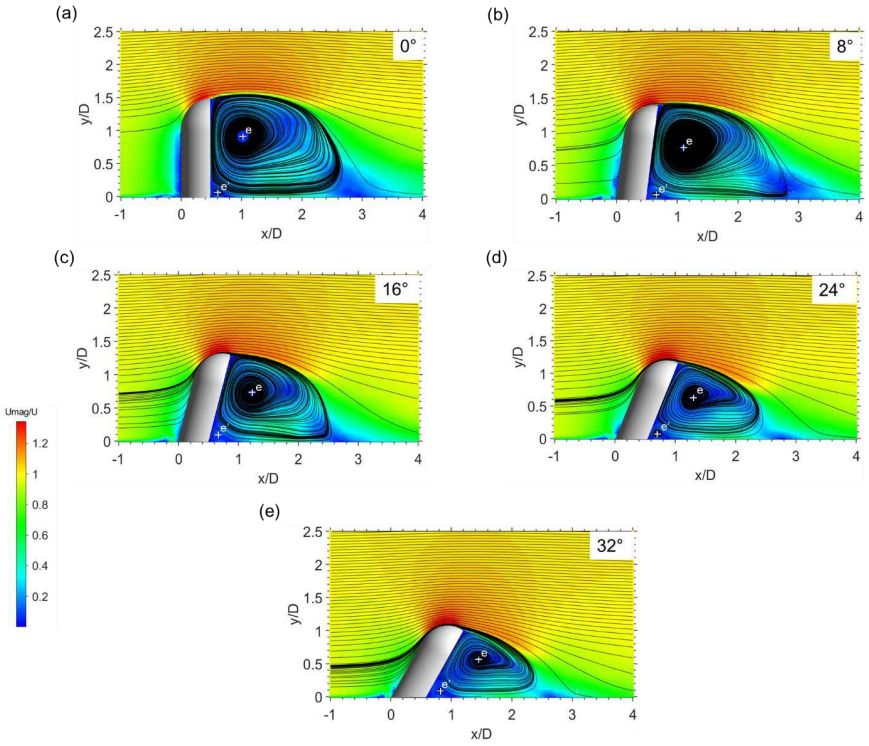

Fig. 23. Comparison of the time-averaged velocity magnitude contour plots superimposed with the velocity streamlines on the midplane for a) $\theta = 0°$, b) $\theta = 8°$, c) $\theta = 16°$, d) $\theta = 24°$,and e) $\theta = 32°$. e and e' represent the centre of recirculation bubbles formed behind the mirror.

Upstream of the mirror, the dominant flow feature is the formation of two distinct horseshoe vortices, h_a and h_b, for 0° and 8° as seen in Fig. 24(a,b). The vortex h_b vanishes for larger values in θ, and the formation of a secondary horseshoe vortex h'_a can be seen at 8° (Fig. 24b), which grows with higher values of θ. The presence of h'_a upstream of the HRM is visualised using the Q criterion, as shown in Fig. 25. These results predict that the horseshoe vortex originating from the upstream region to the side of the HRM moves closer to the mirror with the increase in θ as observed in Fig. 24. L_{hx} further substantiates the observation made in Table 7. The horseshoe vortices h_a and h'_a tend to roll up and merge into the wake as seen in $\theta = 8°$ marked by region b, and with the increase θ, the roll-up of the vortex grows, resulting in the formation of two distinct vortex structures in the wake (w and w') as shown in Fig. 25. The near-wake region represented by a in Fig. 25 reduces in length with an increase in θ, the decrease in the

near-wake region is due to a decrease in the length of the recirculation bubble as seen in Fig. 23.

The two distinct pressure zones p_u and p_d are likely a result of the lateral vortex from the lateral edges of the HRM, and the pressure zone p_m is predicted as a result of impingement of the recirculation bubble on the plate, as seen in Fig. 23. The pressure fluctuations exerted by the lateral vortex show a difference of ~4.5% in the peak intensity levels between p_u and p_d for the standard HRM configuration, as seen in Fig. 26(a), and also the size of the pressure zone show a disparity in the intensity levels which is consistent with the observations made by Ask and Davidson[16] and Yu *et al.*[22]. The intensity of p_m increases with an increase in θ from 16° to 32°. Compared to $\theta = 0°$, 32° case shows an additional pressure zone (p_m) formed on the plate as seen in Fig. 26 despite this, the overall intensity levels shown by $\theta = 32°$ is weaker than 0°.

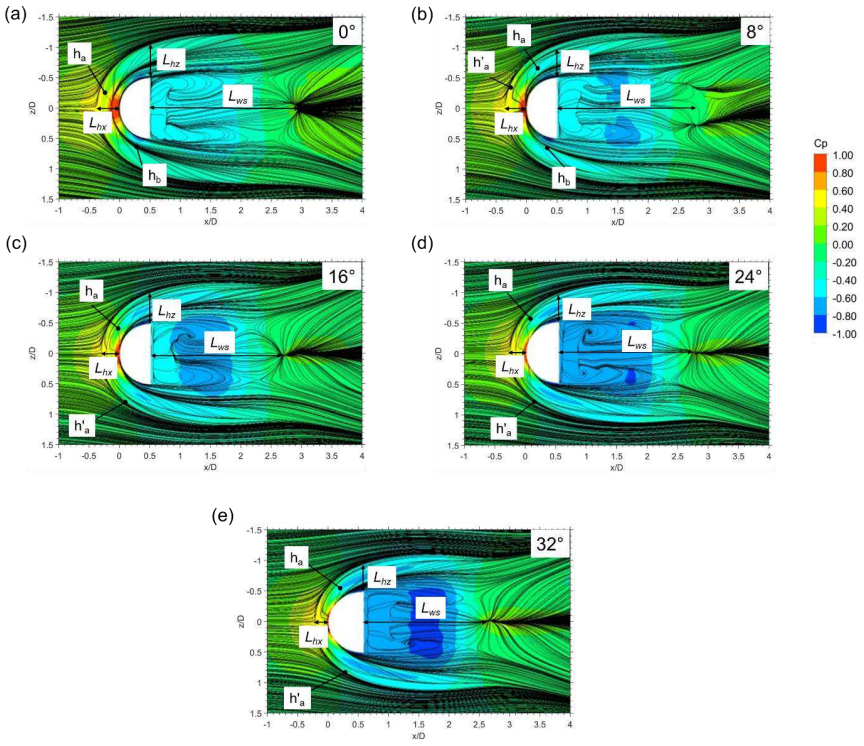

Fig. 24. Comparison of the time-averaged velocity magnitude streamlines superimposed on the pressure coefficient generated on a plane at $y = 0.01D$ between all the sweep angles investigated: a) $\theta = 0°$, b) $\theta = 8°$, c) $\theta = 16°$, d) $\theta = 24°$,and e) $\theta = 32°$. L_{hx}, L_{hz} and L_{ws} represent the horseshoe vortex's normalised length from the mirror, the normalised height of the horseshoe vortex from the lateral edge of the mirror, and the normalised length of the wake structure measured from the rear face of the mirror, respectively.

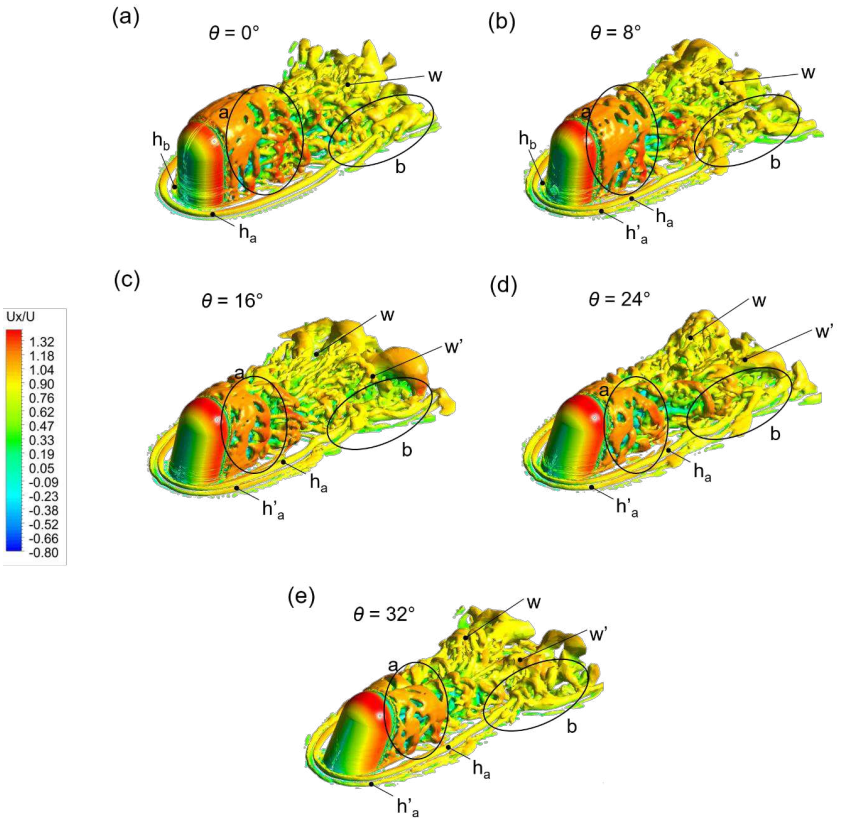

Fig. 25. Comparison of the vortical structures of an instantaneous flow field visualised by iso-surfaces of $Q = 10^3$ s^{-2} coloured with instantaneous x-velocity between all the sweep angles investigated: a) $\theta = 0°$, b) $\theta = 8°$, c) $\theta = 16°$, d) $\theta = 24°$,and e) $\theta = 32°$.

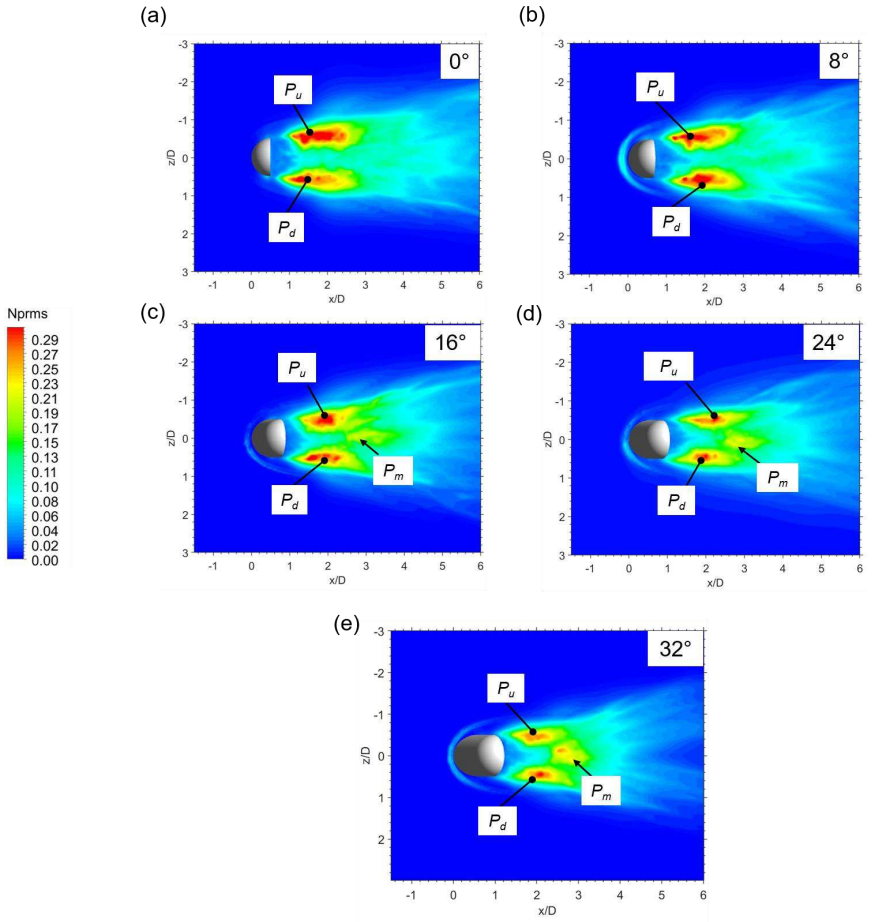

Fig. 26. Comparison of the time-averaged normalised pressure fluctuations on the plate for all the sweep angles investigated: a) $\theta = 0°$, b) $\theta = 8°$, c) $\theta = 16°$, d) $\theta = 24°$,and e) $\theta = 32°$. P_u and P_d represent the pressure regions formed due to the lateral vortex, and P_m represents the pressure region formed due to the impingement of the flow.

The sensors located on the mirror at s111 and s114 show a maximum reduction of ~5 dB at the vortex shedding frequency (~40Hz) with the increase in θ from the standard HRM configuration (0°) as shown in Fig. 27, with $\theta = 24°$ reporting the lowest intensity levels in both low and mid-frequency ranges. A similar trend is observed at s119 located on the plate, but moving downstream to sensors s120, s122, and s123 (Fig. 28), the intensity levels are lowest for the $\theta = 32°$. The radiated noise measured at all the four different microphone locations indicates a decrease in the SPL for $\theta = 32°$, as seen in Fig. 29.

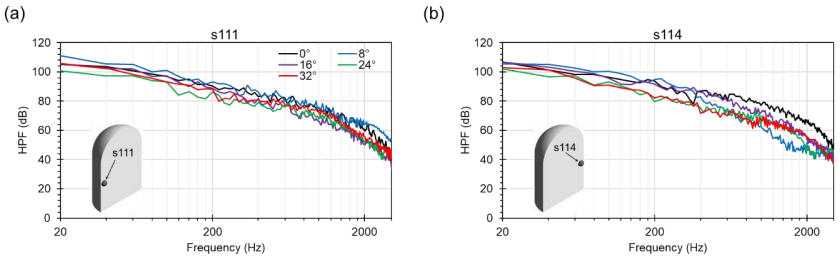

Fig. 27. Comparison of the hydrodynamic pressure fluctuations extracted on the mirror at a) s111 and b) s114 for all the sweep angles investigated: 0°, 8°, 16°, 24° and 32°. The location of the sensors is indicated within each figure.

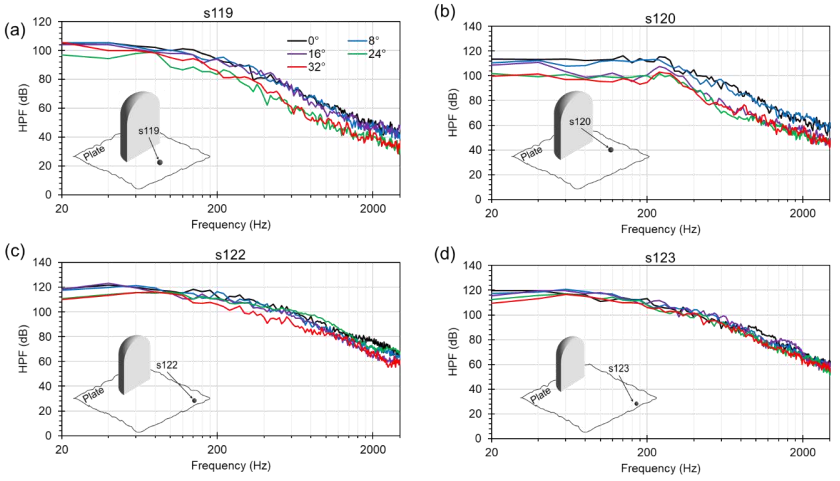

Fig. 28. Comparison of the hydrodynamic pressure fluctuations extracted on the plate at a) s119, b) s120, c) s122 and d) s123 for all the sweep angles investigated: 0°, 8°, 16°, 24° and 32°. The location of the sensors is indicated within each figure.

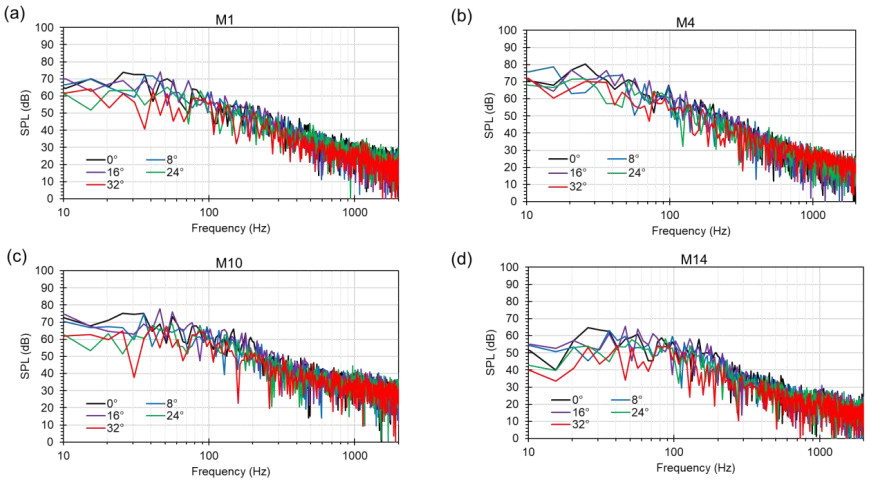

Fig. 29 Comparison of the sound pressure level extracted at four microphone positions a) M1, b) M4, c) M10, and d) M14 for all the sweep angles investigated, viz., 0°, 8°, 16°, 24° and 32°.

Fig. 30 represents the hydrodynamic pressure spectra (HPS) obtained for all the sweep cases investigated in this study. The harmonics presented by the hydrodynamic pressure spectra are more dominant at 40Hz compared to other frequencies that are presented. A decrease in the size of the intensity zones is seen for $\theta = 24°$ and 32°, which agrees with the reduction in the characteristic lengths shown in Fig. 24. As a result, by inclining the mirror closer to the plate, a tendency to reducing the noise generated from the mirror is predicted. The radiated noise closest to the plate shown at $y = 0.25D$ in Fig. 31 resembles a dipole-like structure for all the angles investigated in this study. However, away from the plate, at $y = 2D$, the noise radiated resembles a monopole-like structure. This suggests that there is a dipole to monopole transition in the structure of the induced noise that takes place closest to the plate and regions further away from the plate for all the cases investigated in the study. Also, the intensity levels of the induced noise decrease with an increase in θ.

This numerical work reveals that the change in the topology of the HRM viz., change in *AR* and change in sweep angles (θ) may not necessarily affect the overall structure of the induced noise. However, the overall SPL levels of the induced noise can vary depending on the configuration of the HRM.

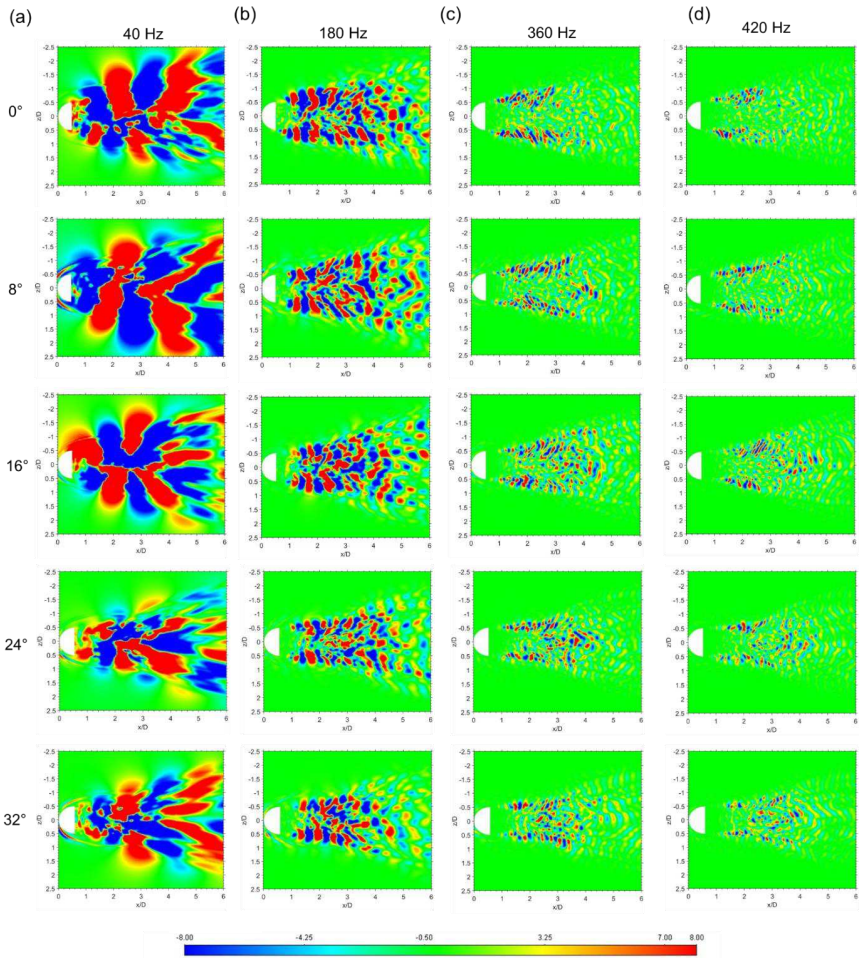

Fig. 30. Comparison of the real part of the Hydrodynamic Pressure Spectra (HPS) generated on the plate for all the sweep angles investigated, viz., 0°, 8°, 16°, 24° and 32°at a) 40 Hz, b) 180 Hz, c) 360 Hz, and d) 420 Hz.

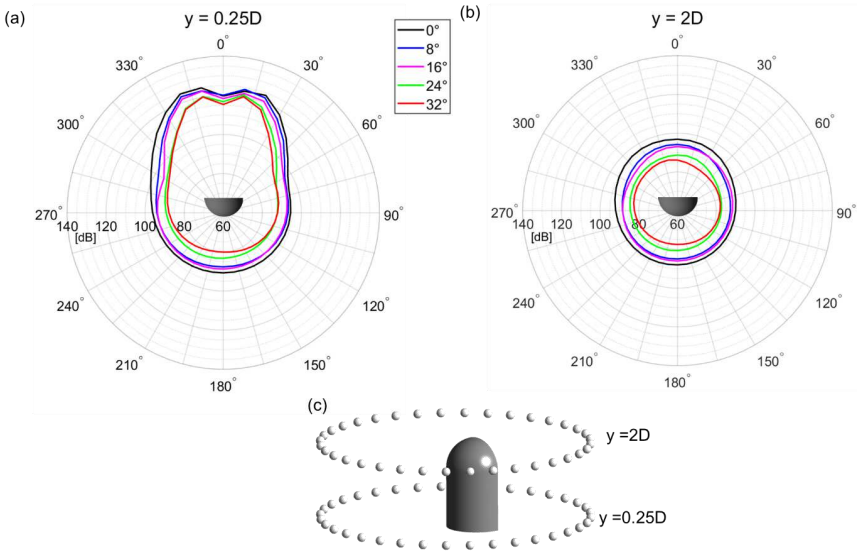

Fig. 31. Comparison of overall sound pressure level extracted at 36 microphones placed in a circular array at planes a) $y = 0.25D$ and b) $y = 2D$ for all the sweep angles investigated, viz., 0°, 8°, 16°, 24° and 32°, and c) illustrates the layout of the sensors located around the mirror at two different heights.

CONCLUSION

A numerical investigation was conducted to predict the noise generated and emitted from a subcritical flow (Re_D = 5.2 x 10^5) past a generic side-view mirror (HRM) mounted on a plate. Detailed flow features, fluctuating pressure distributions on the plate and the mirror, including the near field noise, were obtained by employing a hybrid RANS-LES approach, namely the Stress-Blended Eddy Simulation (SBES). The radiated noise was predicted by employing Ffowcs Williams-Hawkings (FW-H). The main conclusions of this study are summarised as follows:

(1) A comprehensive verification and validation strategy was presented to assess the applicability of SBES-FW-H for predicting both the near field and far-field noise characteristics from the HRM. An unstructured poly-hex core grid was carefully chosen using a grid independency study that was further substantiated by comparing against several previously published numerical and experimental results. Further, a comparison against the surface integral methodologies employed for radiated noise, such as FW-H and Kirchhoff's Integral obtained by solving the Acoustic Perturbation Equation (APE), was undertaken. The SBES-FW-H methodology provided a reasonable agreement with experimental data sets and other published numerical results. Therefore, it was chosen as a preferred methodology to further investigate various configurations of the HRM that can possibly alter the aerodynamically induced noise.

(2) With the SBES-FW-H methodology established, the variation in noise generated and radiated owing to the changes in Aspect Ratio (AR) of the HRM and the sweep angle (θ) between the HRM and the plate were investigated. The numerical predictions suggest that increasing AR from the standard mirror (AR = 1.5) results in an increase in the size of the recirculation bubble and the length of the wake. As a result, the pressure fluctuations exerted on the plate also increases, which increases the aerodynamic noise by ~ 8% for AR = 2.5. The induced noise is also found to decrease with a reduction from the AR of the standard mirror. Typically, the radiated noise decreases by ~12% for AR = 1. This reduction is consistent for noise predicted at several sensors, microphone locations and the directivity plots extracted at 36 microphones locations for the lateral and vertical directions of the wake and closest to the plate. Conversely, an increase in the sweep angle (θ) dampens the induced noise, despite some increase in the fluctuating pressure regions on the plate. The flow appears to separate from the mirror by traversing upward with an increase in θ. The flow then separates from the top of the

mirror and impinges on the plate resulting in an additional pressure zone. A maximum of 4 dB reduction in the radiated sound is observed with $\theta = 32°$.

(3) The numerical results obtained by changing the topologies of the mirror in terms of *AR* and θ reveal that for all the cases examined, a monopole to dipole transition takes place between the radiated noise from upstream of the mirror and closest to the plate. This result suggests that the overall structure of the induced noise from the mirror does not influence change in either *AR* or θ. However, the intensity levels of the generated sound appear to depend on the configuration examined.

This study has demonstrated that the noise from the side-view mirrors can be effectively mitigated by carefully reducing the *AR* of the mirror or the sweep angle (θ) between the mirror and the plate. However, further investigations of this study can be extended to identify the vortex interactions between the mirror and a vehicle's A-pillar, the interplay between features on the mirrors that can induce tonal noise, and Tollmien-Schlichting like waves that can potentially arise due to laminar-turbulent transition on the plate and the mirror for different inflow conditions.

ACKNOWLEDGEMENT

The authors would like to thank ANSYS for sharing the structured grid for the Half-Round Mirror and very grateful for the Academic Research Partnership Grant. This work is supported by the Vice-Chancellor PhD scholarship between Sheffield Hallam University and HORIBA–MIRA.

APPENDIX A: SENSOR AND MICROPHONE LOCATIONS

Table 8

Cartesian coordinates of the sensors located on the standard HRM in m

Sensor	x	y	z		Sensor	x	y	z
s1	0.0936	0.0667	-0.0998		**s18**	0	0.1000	0
s2	0.0936	0.1333	-0.0998		**s19**	0	0.0667	0
s3	0.0936	0.1667	-0.0998		**s20**	0	0.0333	0
s4	0.0936	0.2000	-0.0998		**s21**	0.0034	0.1333	-0.0259
s5	0.0936	0.2258	-0.0964		**s22**	0.0134	0.1333	-0.0500
s6	0.0936	0.2499	-0.0864		**s23**	0.0293	0.1333	-0.0707
s7	0.0936	0.2864	-0.0499		**s24**	0.0500	0.1333	-0.0866
s8	0.0936	0.2964	-0.0258		**s25**	0.0741	0.1333	-0.0966
s9	0.0936	0.2998	0		**s26**	0.1000	0.1500	0.0850
s10	0.0741	0.2966	0		**s27**	0.1000	0.2850	-0.0111
s11	0.0500	0.2866	0		**s28**	0.1000	0.2674	-0.0517
s12	0.0293	0.2707	0		**s29**	0.1000	0.2111	-0.0843
s13	0.0134	0.2500	0		**s30**	0.1000	0.1500	-0.0850
s14	0.0034	0.2259	0		**s31**	0.1000	0.0500	-0.0850
s15	0	0.2000	0		**s32**	0.1000	0.0500	0
s16	0	0.1666	0		**s33**	0.1000	0.2000	0
s17	0	0.1333	0		**s34**	0.1000	0.2500	0

Table 9

Cartesian coordinates of the sensors located on the standard HRM and the plate in m

Sensor	x	y	z
s111	0.1	0.1167	0.085
s112	0.1	0.2517	0.0674
s113	0.1	0.2517	-0.0674
s114	0.1	0.1167	-0.085
s119	0.2	0	0
s120	0.1995	0	-0.1105
s121	0.2989	0	-0.1209
s122	0.3984	0	-0.1314
s123	0.4978	0	-0.1418

Table 10

Cartesian coordinates of the microphone locations in m

Microphone	x	y	z
M1	-0.248	0.446	0.2469
M4	0.1	0.2	-0.5
M10	0.453	0.5458	0
M11	0.453	0.446	-0.2469
M14	0.1	1.615	-1.4345

APPENDIX B: ADDITIONAL COMPARISONS

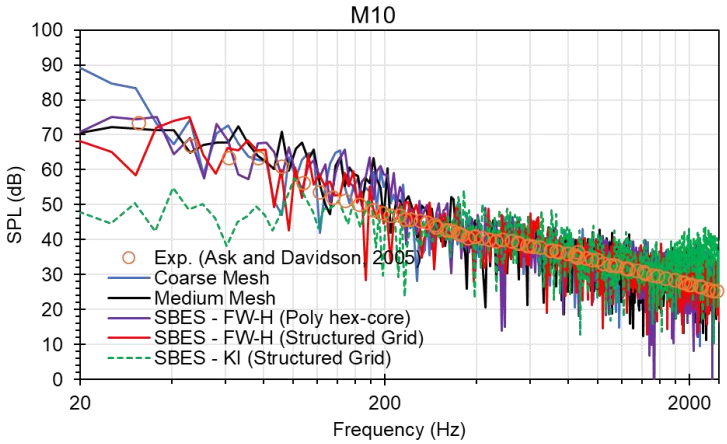

Fig. 32. Comparison between SPL predicted at M10 using SBES–FW-H approach with the structured grid, SBES – KI approach with structured grid and SBES–FW-H approach with the Poly-hex core grids used in the grid evaluation study.

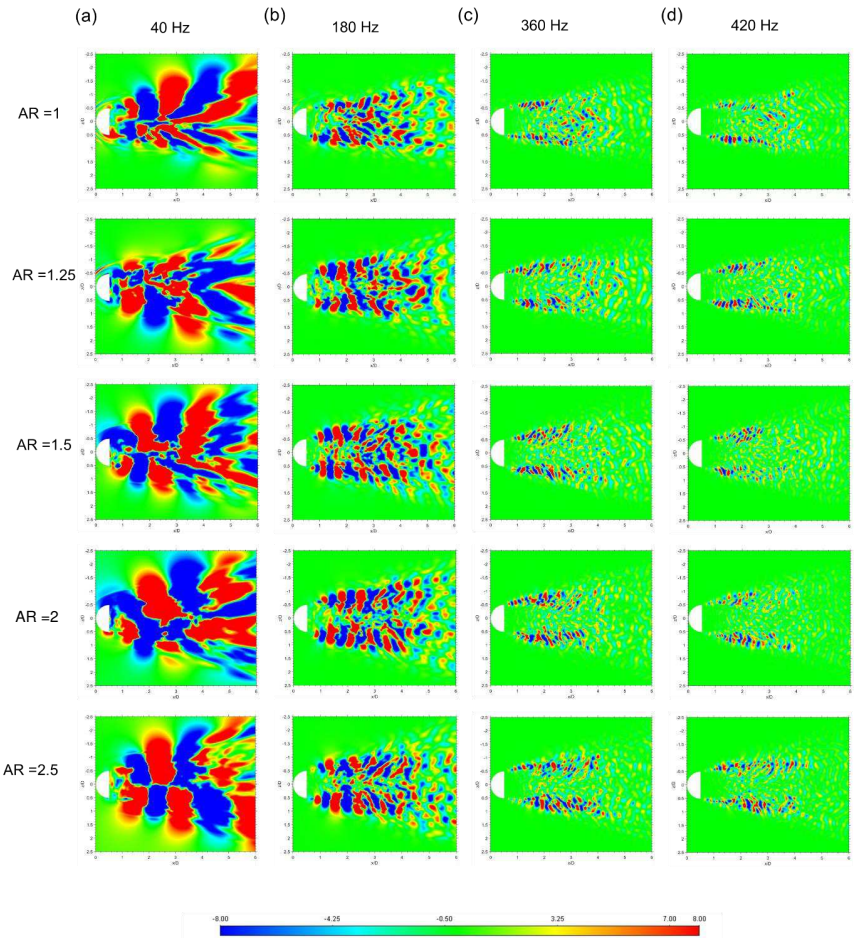

Fig. 33. Comparison of the imaginary part of the Hydrodynamic Pressure Spectra (HPS) generated on the plate between *AR* = 1, 1.25, 1.5, 2 and 2.5 is presented at a) 40 Hz, b) 180 Hz, c) 360 Hz, and d) 420 Hz.

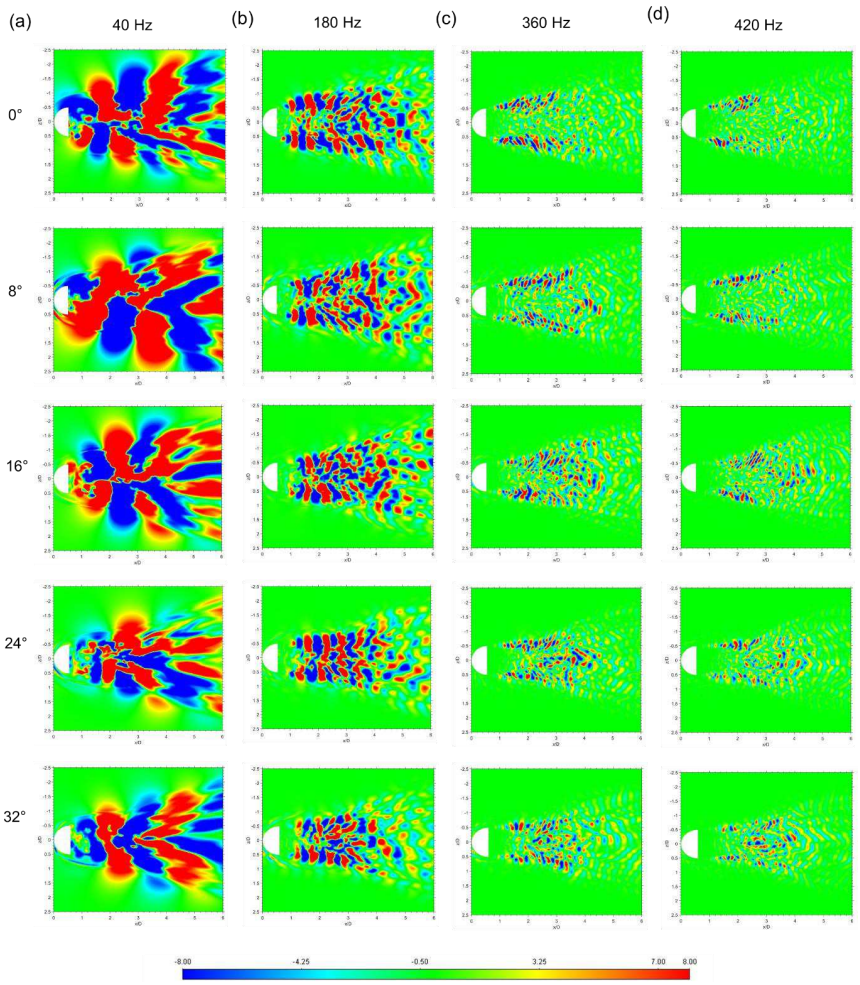

Fig. 34. Comparison of the imaginary part of the Hydrodynamic Pressure Spectra (HPS) generated on the plate between for all the sweep angles, viz., 0°, 8°, 16°, 24° and 32°. a) 40 Hz, b) 180 Hz, c) 360 Hz, and d) 420 Hz.

DATA AVAILABILITY

Data that supports the findings of this study are available from the corresponding author upon reasonable request.

REFERENCES

[1] B. Li, C.C. Ye, Z.H. Wan, N.S. Liu, D.J. Sun, and X.Y. Lu, "Noise control of subsonic flow past open cavities based on porous floors,"Phys. Fluids **32**, (2020).

[2] G. Nasif, R. Balachandar, and R.M. Barron, "Influence of bed proximity on the three-dimensional characteristics of the wake of a sharp-edged bluff body,"Phys. Fluids **31**, 025116 (2019).

[3] Y. Wang, D. Thompson, and Z. Hu, "Numerical investigations on the flow over cuboids with different aspect ratios and the emitted noise,"Phys. Fluids **32**, (2020).

[4] Y. Wang, D. Thompson, and Z. Hu, "Effect of wall proximity on the flow over a cube and the implications for the noise emitted,"Phys. Fluids **31**, (2019).

[5] H.D. Yao and L. Davidson, "Generation of interior cavity noise due to window vibration excited by turbulent flows past a generic side-view mirror,"Phys. Fluids **30**, (2018).

[6] H. Yao, L. Davidson, and L. Eriksson, "Noise radiated by low-Reynolds number flows past a hemisphere at Ma = 0.3,"Phys. Fluids **29**, 076102 (2017).

[7] B. Mahato, N. Ganta, and Y.G. Bhumkar, "Mitigation of aerodynamic sound for a laminar flow past a square cylinder using a pair of cowl plates,"Phys. Fluids **32**, (2020).

[8] A.M. Shinneeb, R. Balachandar, and K. Zouhri, "Effect of gap flow on the shallow wake of a sharp-edged bluff body - Coherent structures,"Phys. Fluids **30**, (2018).

[9] H. Yuan, Z. Yang, Y. Wang, Y. Fan, and Y. Fang, "Experimental analysis of hydrodynamic and acoustic pressure on automotive front side window,"J. Sound Vib. **476**, (2020).

[10] S. Becker, K. Nusser, and M. Oswald, "Aero-Vibro-Acoustic Wind Noise-Simulation Based on the Flow around a Car,"SAE Tech. Pap. (2016).

[11] M. Helfer, "General Aspects of Vehicle Aeroacoustics,"in *Lect. Ser. Road Veh. Aerodyn.* (Von Karman Institute, Rhode-Genèse, Belgium, 2005).

[12] R. Höld, A. Brenneis, A. Eberle, V. Schwarz, and R. Siegert, "Numerical simulation of aeroacoustic sound generated by generic bodies placed on a plate: Part I - Prediction of aeroacoustic sources,"in *5th AIAA/CEAS Aeroacoustics Conf. Exhib.* (American Institute of Aeronautics and Astronautics, Reston, Virigina, 1999).

[13] R. Siegert, V. Schwarz, and J. Reichenberger, "Numerical simulation of aeroacoustic sound generated by generic bodies placed on a plate: Part II - Prediction of radiated sound pressure,"in *5th AIAA/CEAS Aeroacoustics Conf. Exhib.* (1999).

[14] T. Rung, D. Eschricht, J. Yan, and F. Thiele, "Sound radiation of the vortex flow past a generic side mirror,"in *8th AIAA/CEAS Aeroacoustics Conf. Exhib.* (2002), pp. 1–10.

[15] I. Afgan, C. Moulinec, and D. Laurence, "Numerical simulation of generic side mirror of a car using large eddy simulation with polyhedral meshes,"Int. J. Numer. Methods Fluids **56**, 1107 (2008).

[16] J. Ask and L. Davidson, "A numerical investigation of the flow past a generic side mirror and its impact on sound generation,"J. Fluids Eng. Trans. ASME **131**, 0621011 (2009).

[17] T. Belamri, Y. Egorov, and F. Menter, "CFD simulation of the aeroacoustic noise generated by a generic side view car mirror,"in *13th AIAA/CEAS Aeroacoustics Conf. (28th AIAA Aeroacoustics Conf.* (2007), pp. 1–12.

[18] F. Capizzano, L. Alterio, S. Russo, and C. de Nicola, "A hybrid RANS-LES Cartesian method based on a skew-symmetric convective operator,"J. Comput. Phys. **390**, 359 (2019).

[19] M. Caraeni, O. Aybay, and S. Holst, "Tandem cylinder and idealized side mirror far-field noise predictions using DES and an efficient implementation of FW-H equation,"in *17th AIAA/CEAS Aeroacoustics Conf. 2011 (32nd AIAA Aeroacoustics Conf.* (2011), pp. 5–8.

[20] E. DeVilliers, "The Potential of Large Eddy Simulation for the Modeling of Wall Bounded Flows Eugene de Villiers,"PhD Thesis 1 (2006).

[21] Y. Egorov, F.R. Menter, R. Lechner, and D. Cokljat, "The scale-adaptive simulation method for unsteady turbulent flow predictions. part 2: Application to complex flows,"Flow, Turbul. Combust. **85**, 139 (2010).

[22] L. Yu, S. Diasinos, and B. Thornber, "A Fast Transient Solver for Low-Mach Number Aerodynamics and Aeroacoustics,"Comput. Fluids **214**, 104748 (2020).

[23] J. Ask and L. Davidson, "The sub-critical flow past a generic side mirror and its impact on sound generation and propagation,"in *Collect. Tech. Pap. - 12th AIAA/CEAS Aeroacoustics Conf.* (2006), pp. 1925–1944.

[24] J. Ask and L. Davidson, "The Near Field Acoustics of a Generic Side Mirror based on an

Incompressible Approach,"(2005).

[25] S.B. Pope, "Turbulent Flows,"*Turbulent Flows* (Cambridge University Press, Cambridge, 2000).

[26] W. Calus, H. Thomas, and S. PIERRE, "Large Eddy Simulation for Acoustics,"*Large Eddy Simulation for Acoustics* (2007).

[27] M.S. Gritskevich, A. V. Garbaruk, and F.R. Menter, "Fine-tuning of DDES and IDDES formulations to the *k-ω* shear stress transport model,"Prog. Flight Phys. 23 (2013).

[28] X. Chen and M. Li, "Delayed Detached Eddy Simulation of Subcritical Flow past Generic Side Mirror,"J. Shanghai Jiaotong Univ. **24**, 107 (2019).

[29] A. Tosh, M. Caraeni, and D. Caraeni, "A hybrid computational aeroacoustic method for low speed flows,"2018 AIAA/CEAS Aeroacoustics Conf. 1 (2018).

[30] A. Schell and M. Eiselt, "Numerical Investigation of Tonal Noise at Automotive Side Mirrors due to Aeroacoustic Feedback,"SAE Tech. Pap. Ser. **1**, 1 (2020).

[31] A.H. Dawi and R.A.D. Akkermans, "Spurious noise in direct noise computation with a finite volume method for automotive applications,"Int. J. Heat Fluid Flow **72**, 243 (2018).

[32] M.A. Alhawwary and Z.J. Wang, "Implementation of a fwh approach in a high-order les tool for aeroacoustic noise predictions,"AIAA Scitech 2020 Forum **1 PartF**, (2020).

[33] Y. Khalighi, A. Mani, F. Ham, and P. Moin, "Prediction of sound generated by complex flows at low mach numbers,"AIAA J. **48**, 306 (2010).

[34] B. Lokhande, S. Sovani, and J. Xu, "Computational Aeroacoustic Analysis of a Generic Side View Mirror,"in *SAE Tech. Pap. Ser.* (2003).

[35] H. Choi and P. Moin, "Effects of the Computational Time Step on Numerical Solutions of Turbulent Flow,"J. Comput. Phys. **113**, 1 (1994).

[36] F. Menter, "Stress-Blended Eddy Simulation (SBES)—A New Paradigm in Hybrid RANS-LES Modeling,"in *Notes Numer. Fluid Mech. Multidiscip. Des.* (2018), pp. 27–37.

[37] K.K. Chode, H. Viswanathan, and K. Chow, "Numerical investigation on the salient features of flow over standard notchback configurations using scale resolving simulations,"Comput. Fluids **210**, 104666 (2020).

[38] J. Ye, M. Xu, P. Xing, Y. Cheng, D. Meng, Y. Tang, and M. Zhu, "Investigation of aerodynamic noise reduction of exterior side view mirror based on bionic shark fin structure,"Appl. Acoust. **182**, 108188 (2021).

[39] M. Hartmann, J. Ocker, T. Lemke, A. Mutzke, V. Schwarz, H. Tokuno, R. Toppinga, P. Unterlechner, and G. Wickern, "Wind noise caused by the a-pillar and the side mirror flow of a generic vehicle model,"AIAA Pap. **01**, 1 (2012).

[40] A.H. Dawi and R.A.D. Akkermans, "Direct noise computation of a generic vehicle model using a finite volume method,"Comput. Fluids **191**, 104243 (2019).

[41] S. Bhattacharya and A. Ahmed, "Effect of aspect ratio on the flow over a wall-mounted hemispherical turret,"Int. J. Heat Fluid Flow **84**, 108600 (2020).

[42] D. Sumner, N. Rostamy, D.J. Bergstrom, and J.D. Bugg, "Influence of aspect ratio on the mean flow field of a surface-mounted finite-height square prism,"Int. J. Heat Fluid Flow **65**, 1 (2017).

[43] W. Devenport, N. Alexander, S. Glegg, and M. Wang, "The Sound of Flow Over Rigid Walls,"Annu. Rev. Fluid Mech. **50**, 435 (2018).

[44] F. Nicoud and F. Ducros, "Subgrid-scale stress modelling based on the square of the velocity gradient tensor,"Flow, Turbul. Combust. **62**, 183 (1999).

[45] F.R. Menter, "Two-equation eddy-viscosity turbulence models for engineering applications,"AIAA J. **32**, 1598 (1994).

[46] D.L. Ffowcs Williams, J. E., and Hawkings, "Sound Generation by Turbulence and Surfaces in Arbitrary Motion,"Philos. Trans. R. Soc. London. Ser. A, Math. Phys. Sci. **264**, 321 (1969).

[47] R. Ewert and W. Schröder, "Acoustic perturbation equations based on flow decomposition via source filtering,"J. Comput. Phys. **188**, 365 (2003).

[48] K.K. Chode, H. Viswanathan, and K. Chow, "Computational Aeroacoustics of a Generic Side View Mirror using Stress Blended Eddy Simulation,"2 (2020).

[49] T. Grahs and C. Othmer, "Evaluation of aerodynamic noise generation: Parameter study of generic side mirror evaluating the aeroacoustic source strength,"in *Proc. Eur. Conf. Comput. Fluid Dyn. (ECCOMAS CFD 2006)* (2006), pp. 1–14.

[50] M. Su and J. Der Yu, "A parallel large eddy simulation with unstructured meshes applied to

turbulent flow around car side mirror,"Comput. Fluids **55**, 24 (2012).

[51] F.Q. Hu, M.Y. Hussaini, and J.L. Manthey, "Low-dissipation and low-dispersion Runge-Kutta schemes for computational acoustics,"J. Comput. Phys. **124**, 177 (1996).

[52] R.B. Langtry, E.A. Gren, J. V. Larssen, and P.R. Spalart, "Evaluation of structured and unstructured grids for Detached Eddy Simulation of flap edge noise,"in *15th AIAA/CEAS Aeroacoustics Conf. (30th AIAA Aeroacoustics Conf.* (2009), pp. 11–13.

[53] ANSYS, "5 Best Practices for Gas Turbine Combustion Meshing Using Ansys Fluent,"1 (2020).

[54] H. Yao and L. Davidson, "Vibro-acoustics response of a simplified glass window excited by the turbulent wake of a quarter-spherocylinder body,"J. Acoust. Soc. Am. **145**, 3163 (2019).

[55] J. Ask and L. Davidson, "The sub-critical flow past a generic side mirror and its impact on sound generation and propagation,"Collect. Tech. Pap. - 12th AIAA/CEAS Aeroacoustics Conf. **3**, 1925 (2006).

[56] L. Zhong, Q. Li, Y. Wang, and Z. Yang, "Aerodynamic noise prediction of passenger vehicle with hybrid detached eddy simulation / acoustic perturbation equation method,"**233**, 2390 (2019).

[57] H.D. Yao, L. Davidson, L.E. Eriksson, O. Grundestam, S.H. Peng, and P.E. Eliasson, "Surface integral analogy approaches to computing noise generated by a 3D high-lift wing configuration,"50th AIAA Aerosp. Sci. Meet. Incl. New Horizons Forum Aerosp. Expo. 9 (2012).

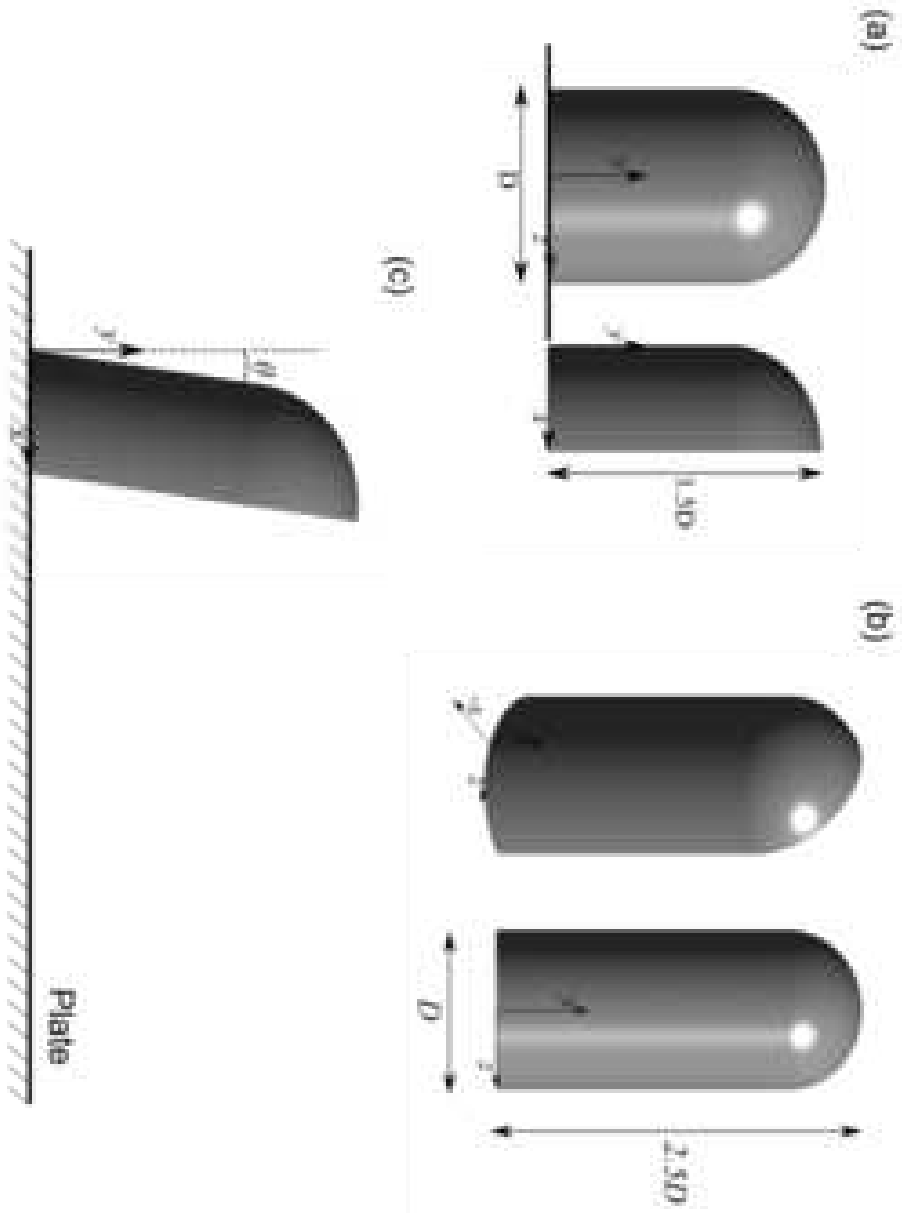

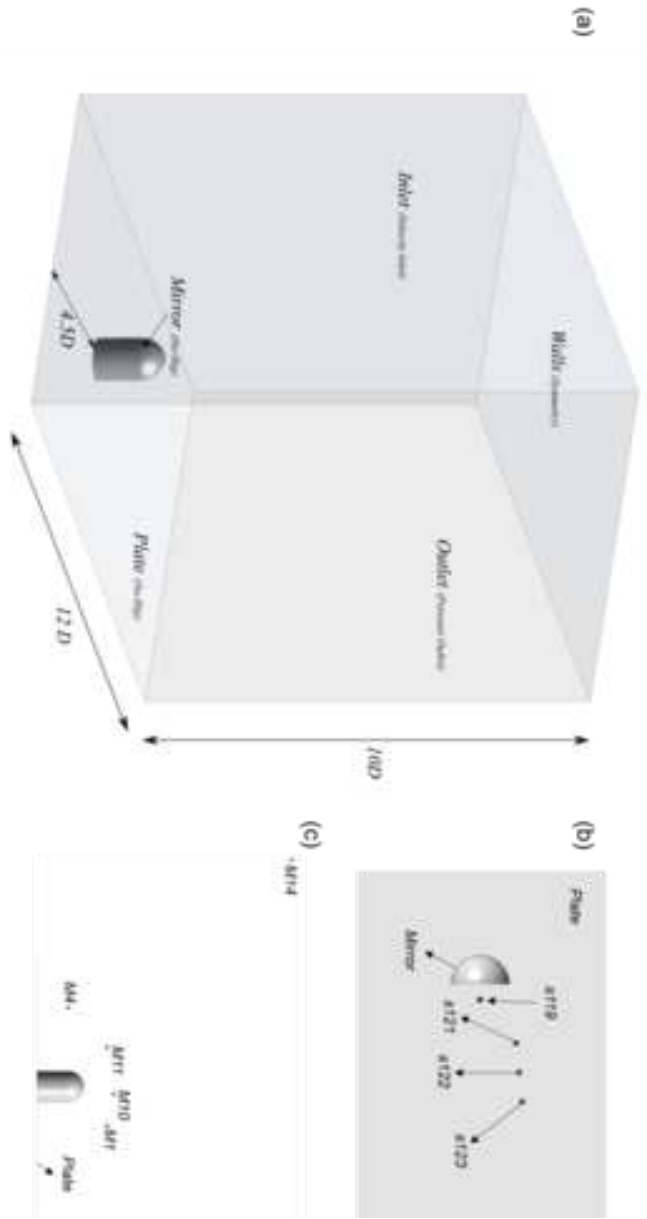

PLEASE CITE THIS ARTICLE AS DOI: 10.1063/5.0057166

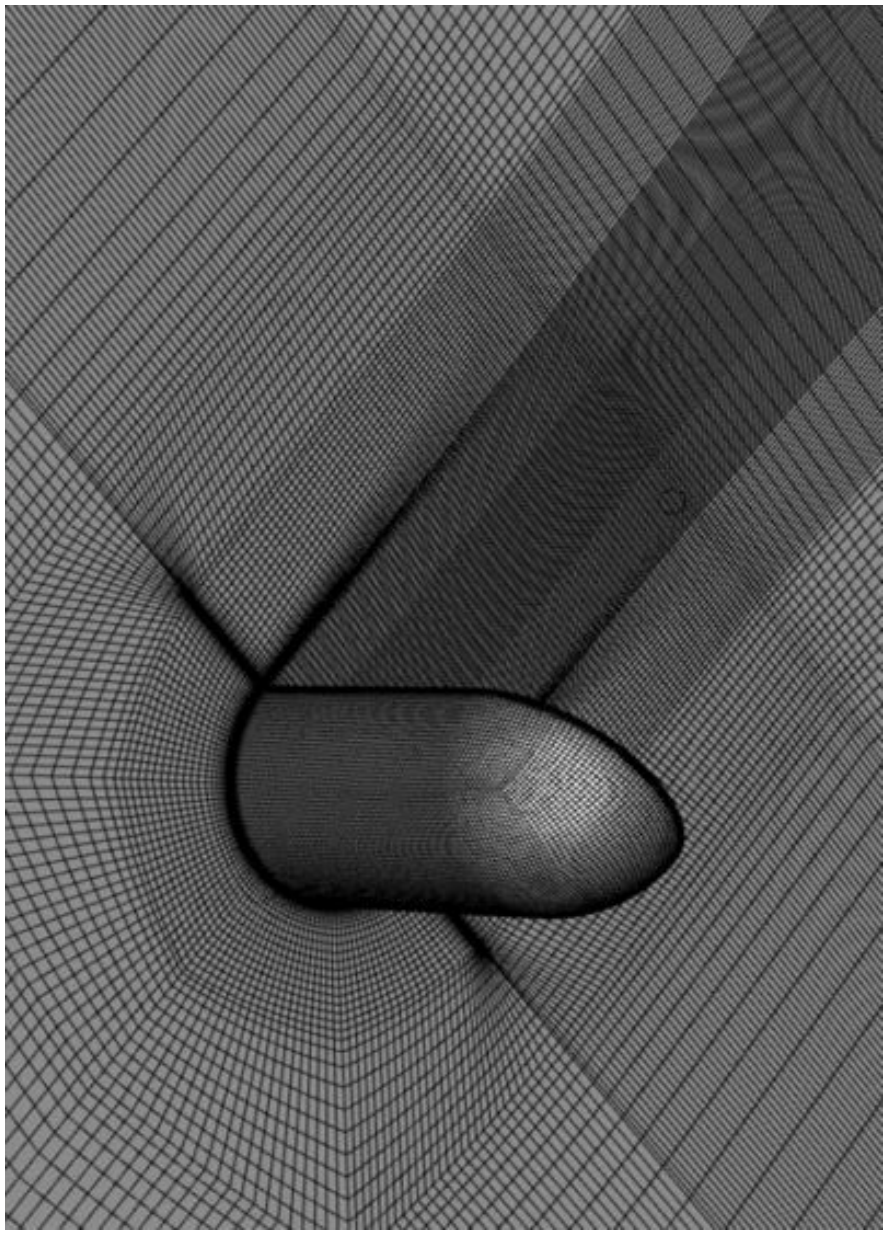

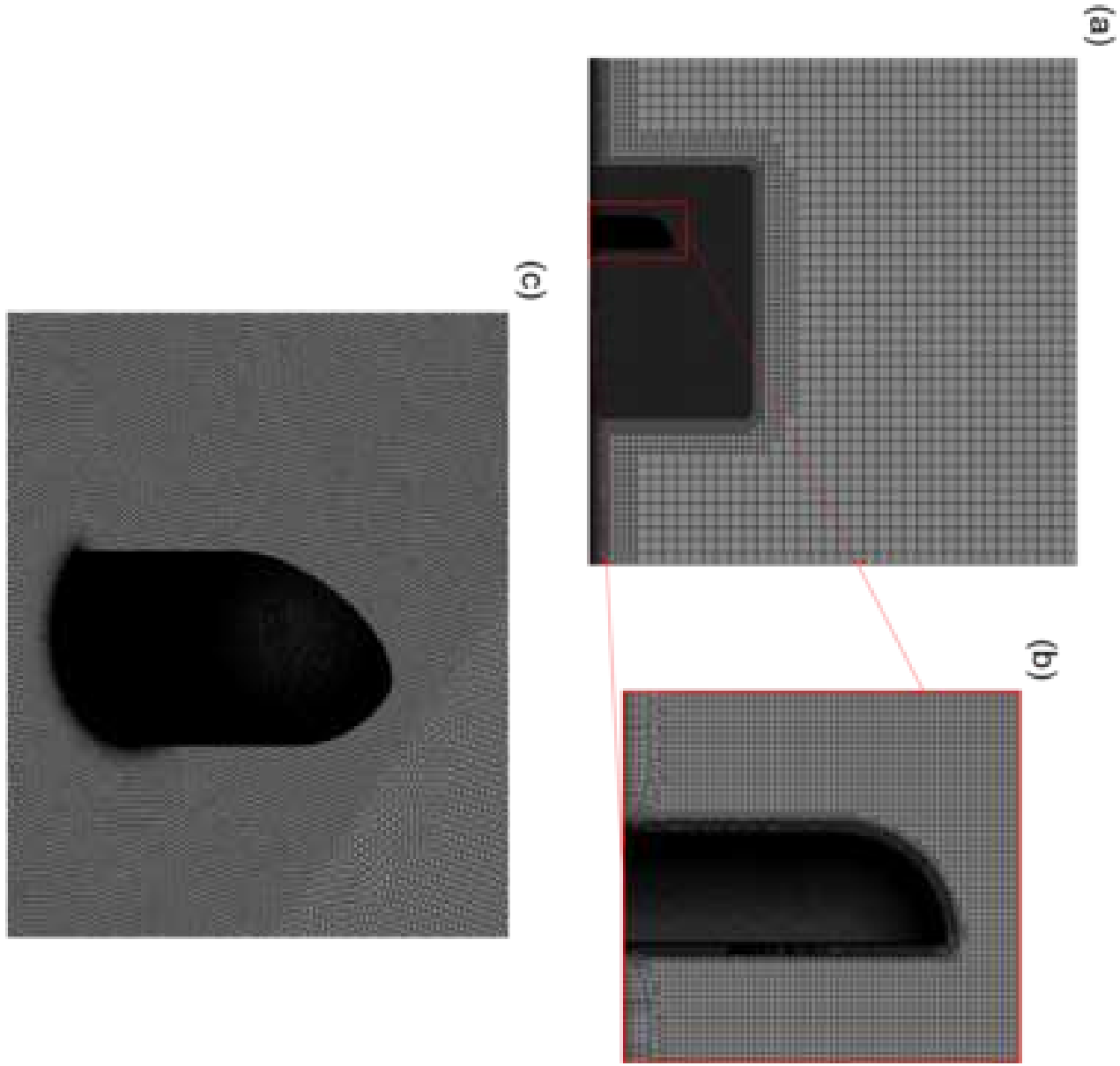

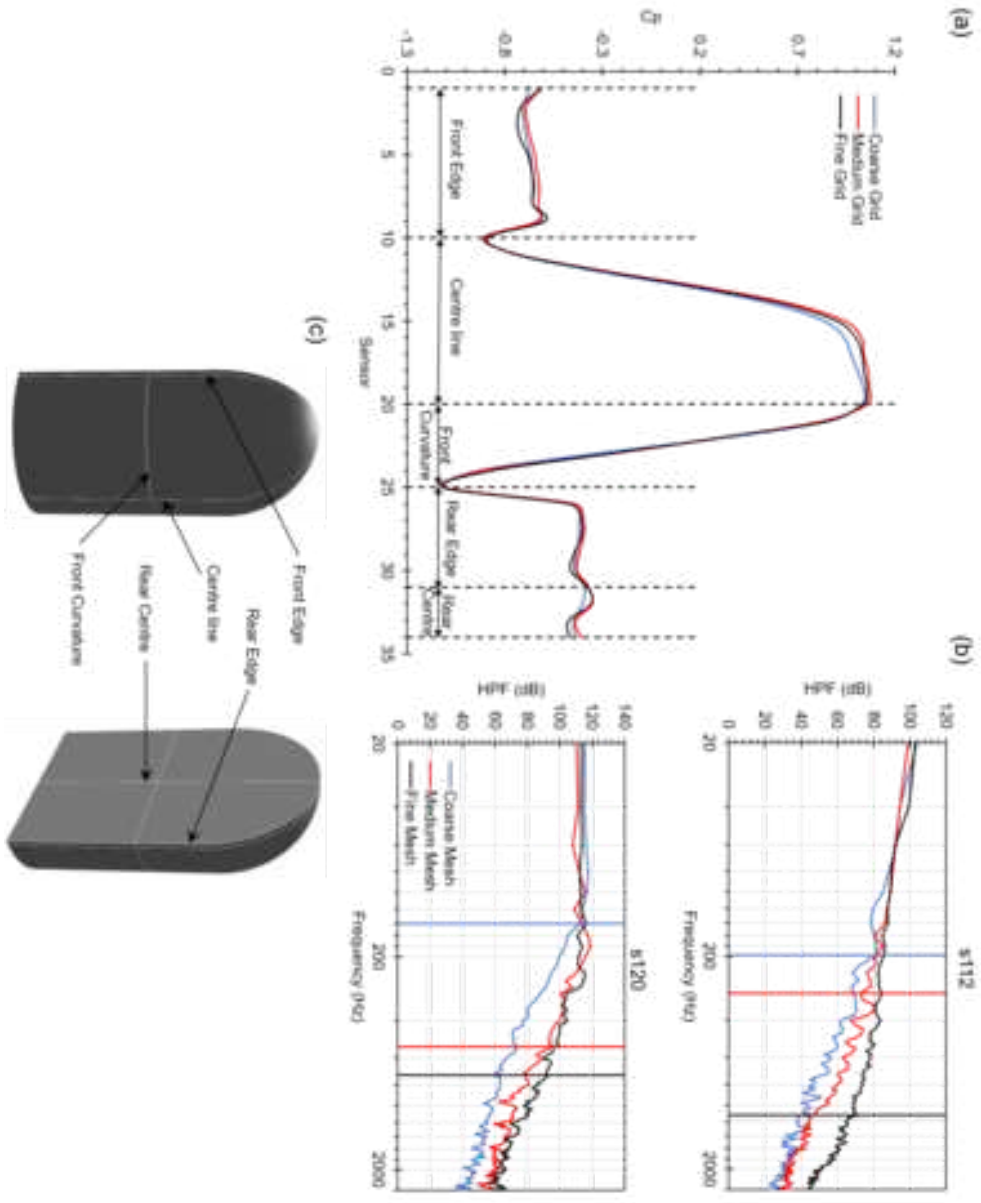

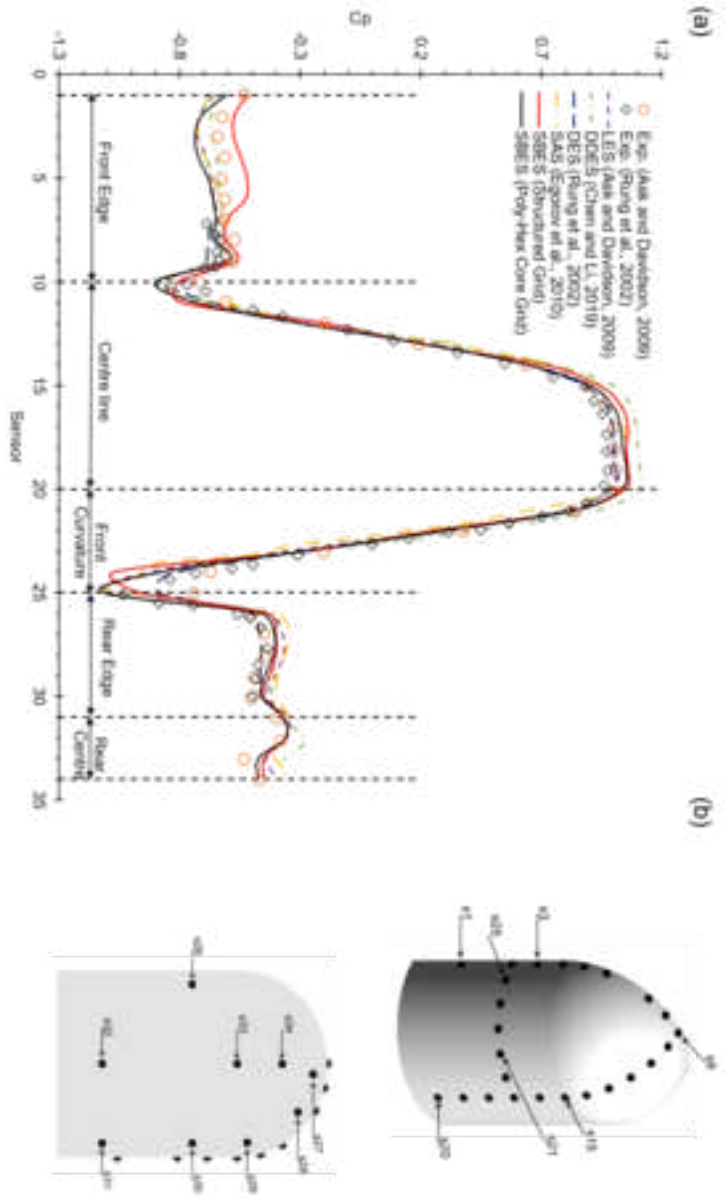

PLEASE CITE THIS ARTICLE AS DOI: 10.1063/5.0057166

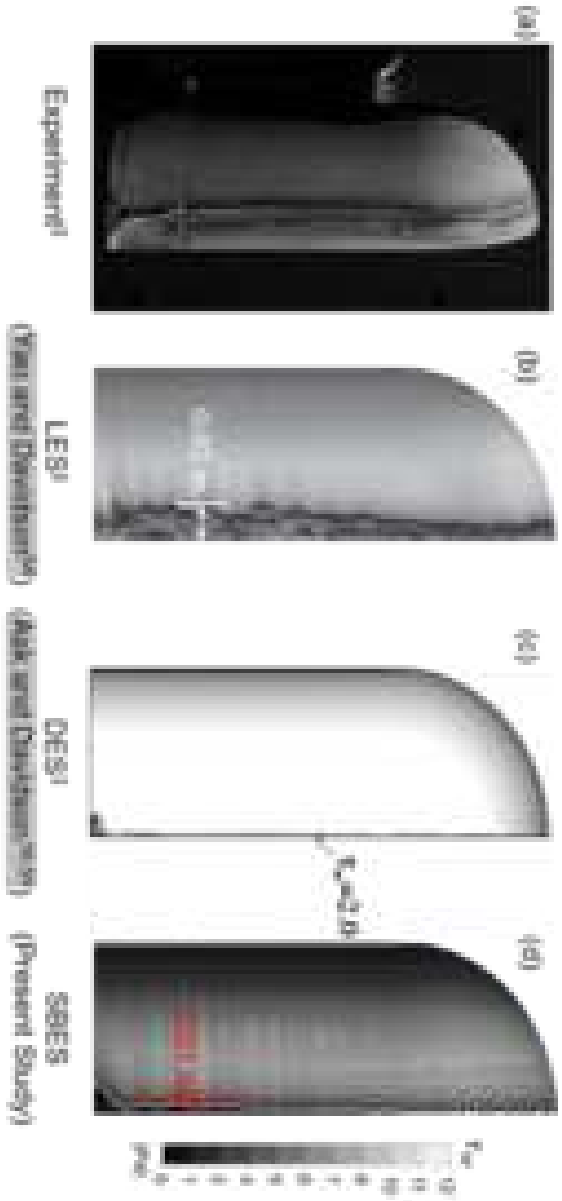

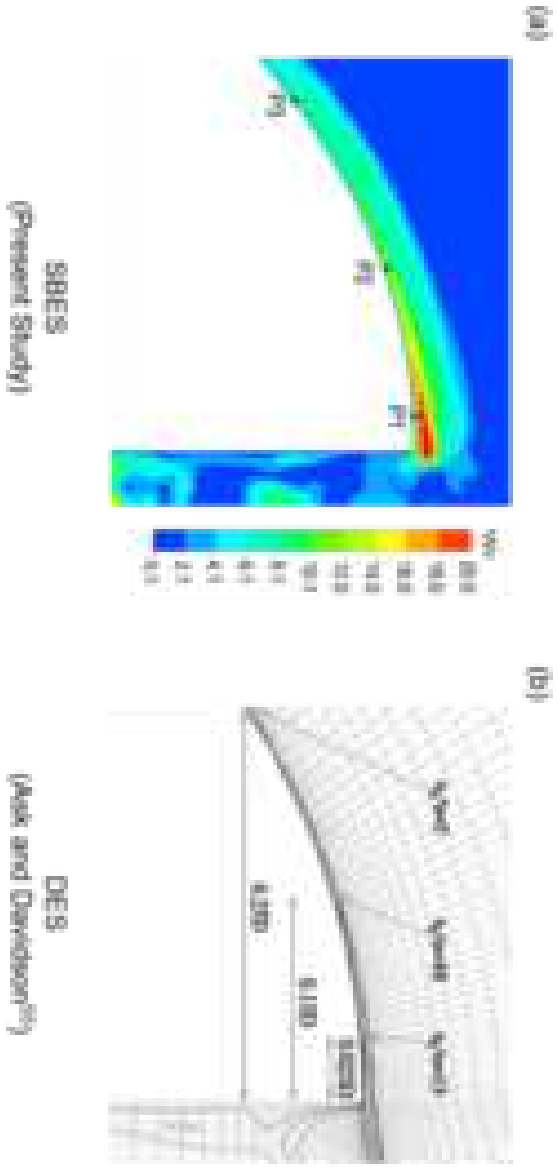

PLEASE CITE THIS ARTICLE AS DOI: 10.1063/5.0057166

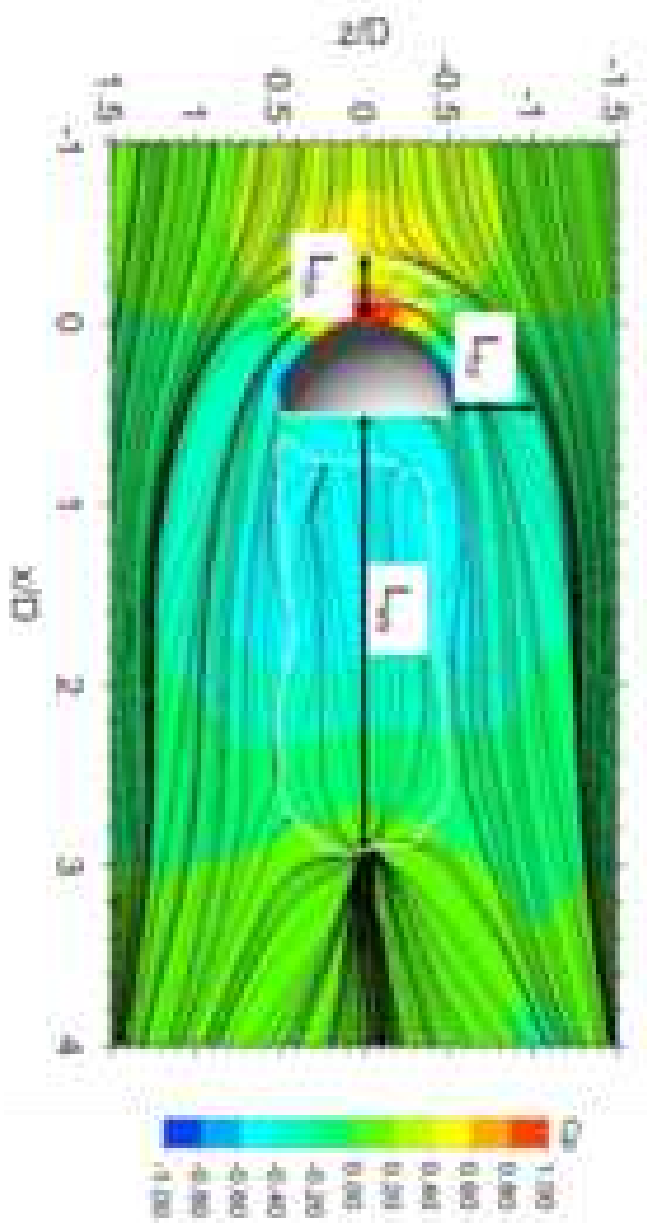

PLEASE CITE THIS ARTICLE AS DOI: 10.1063/5.0057166

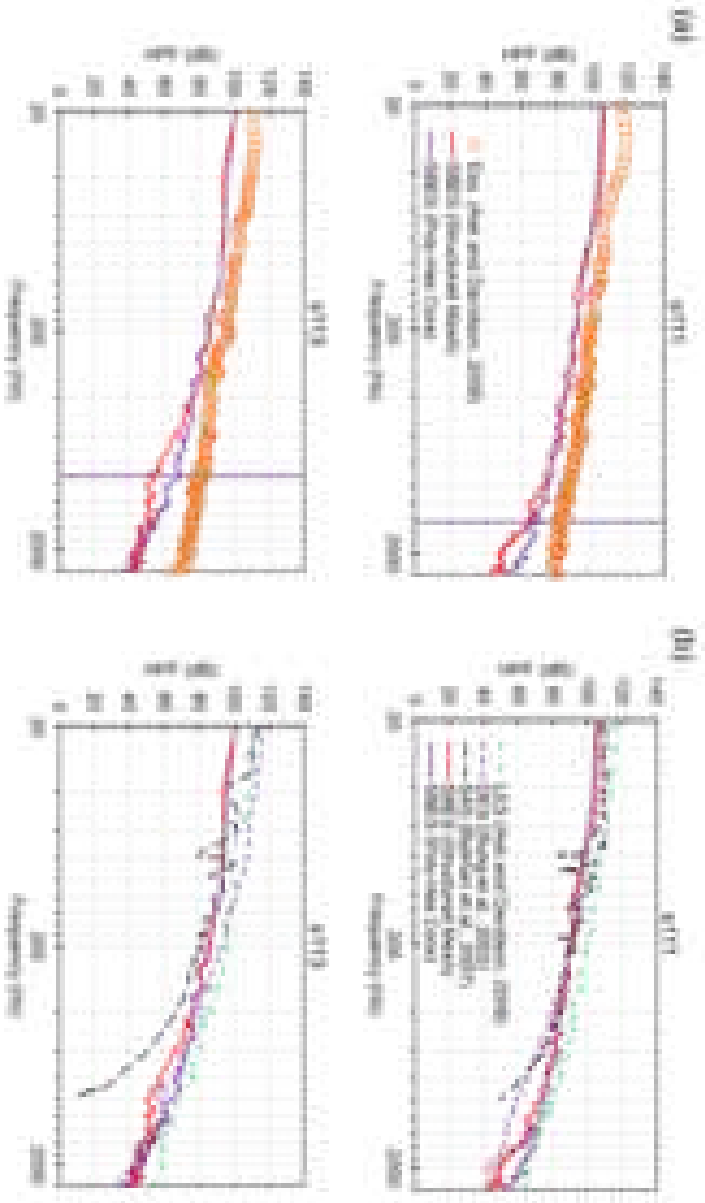

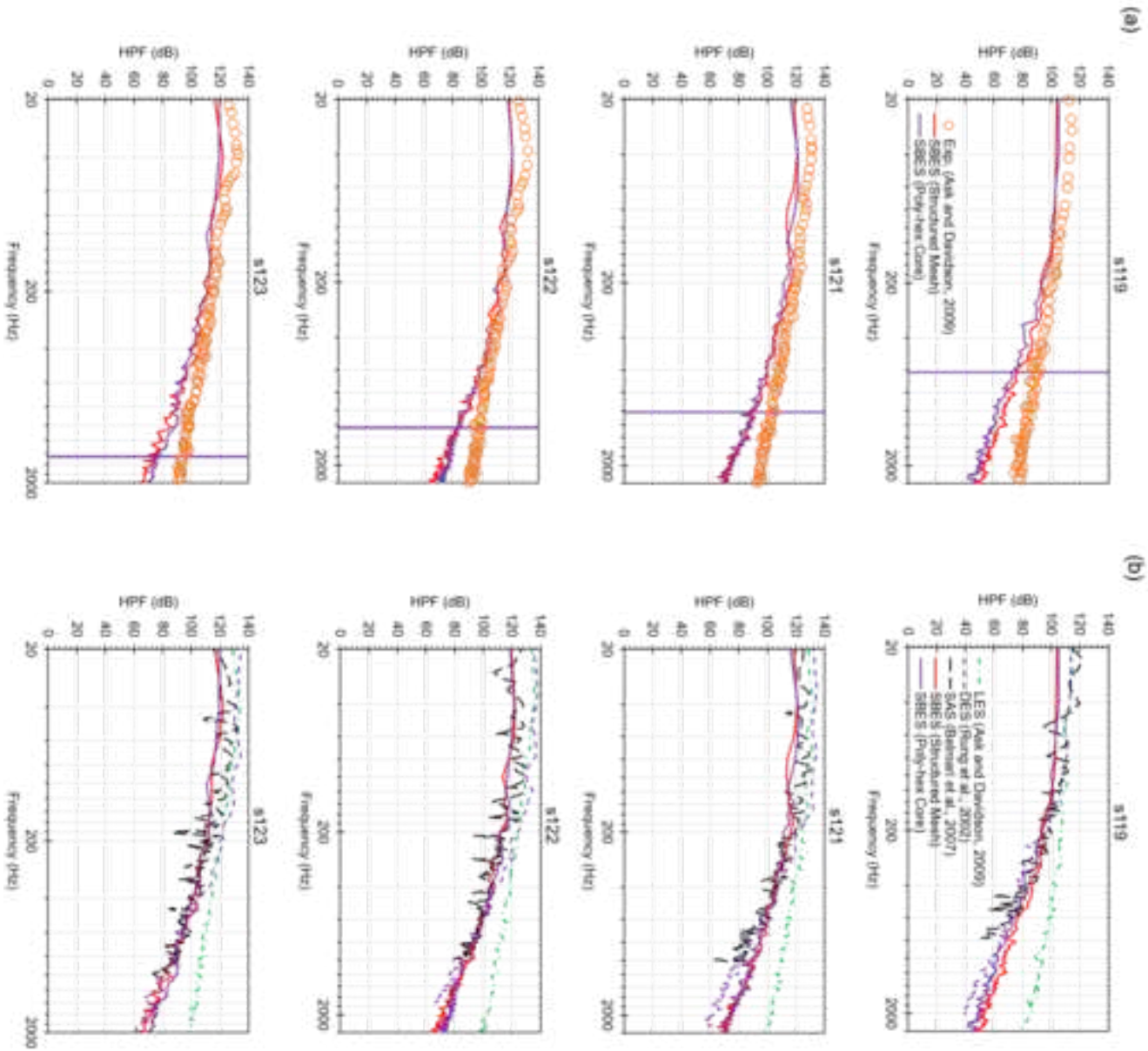

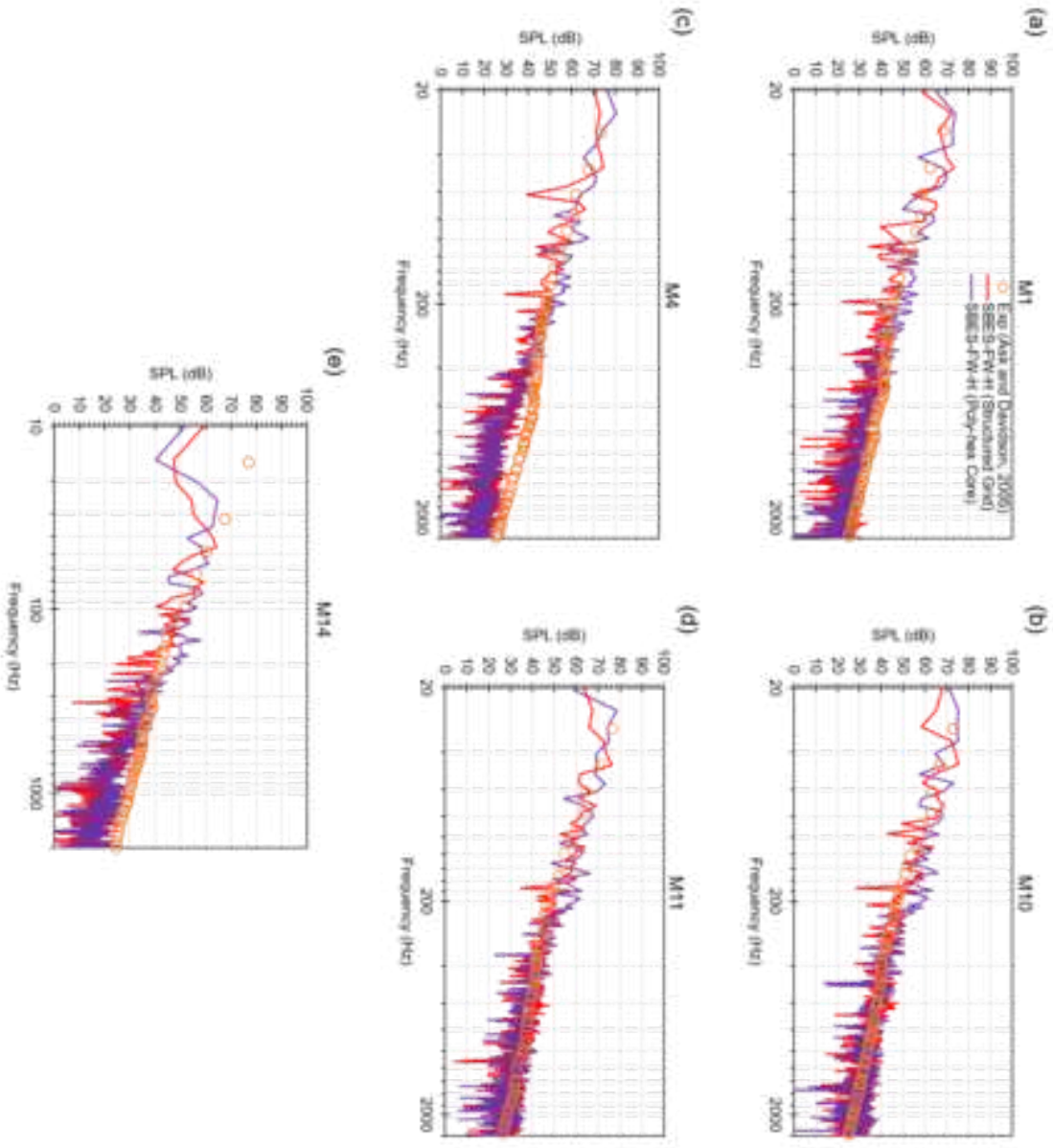

PLEASE CITE THIS ARTICLE AS DOI: 10.1063/5.0057166

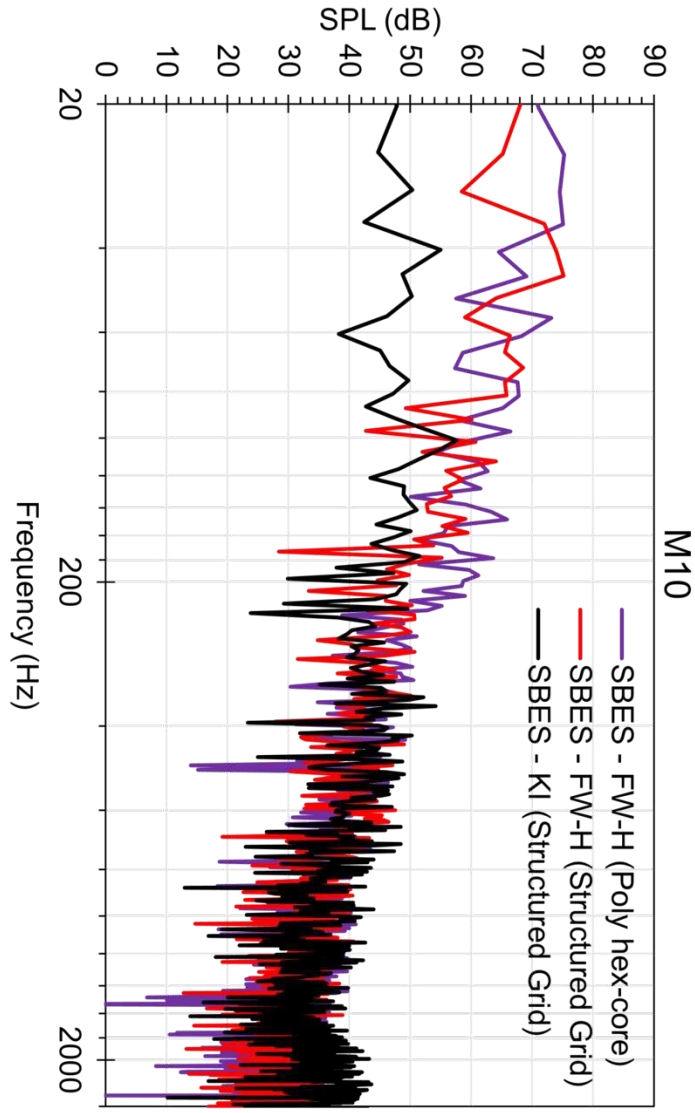

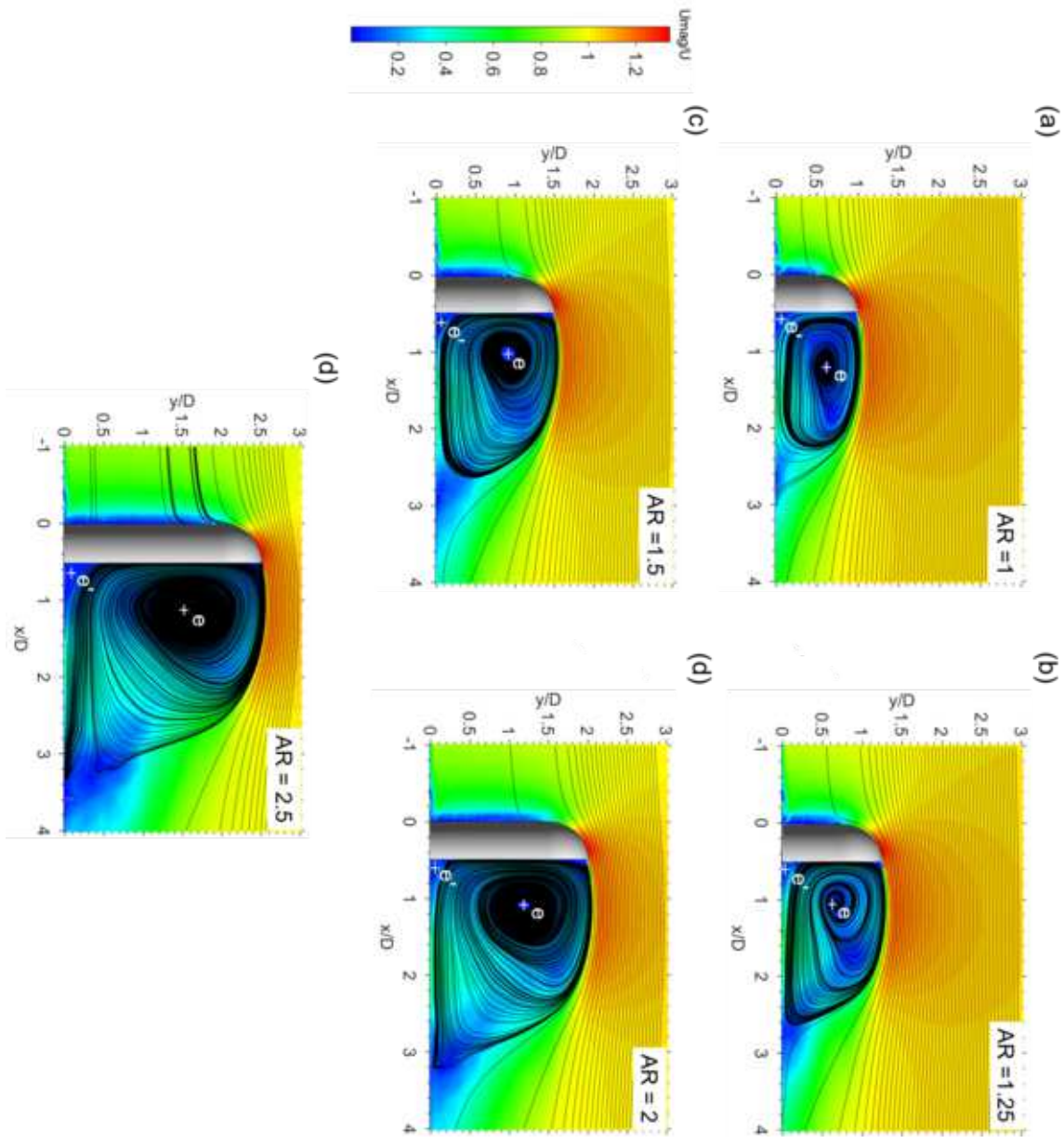

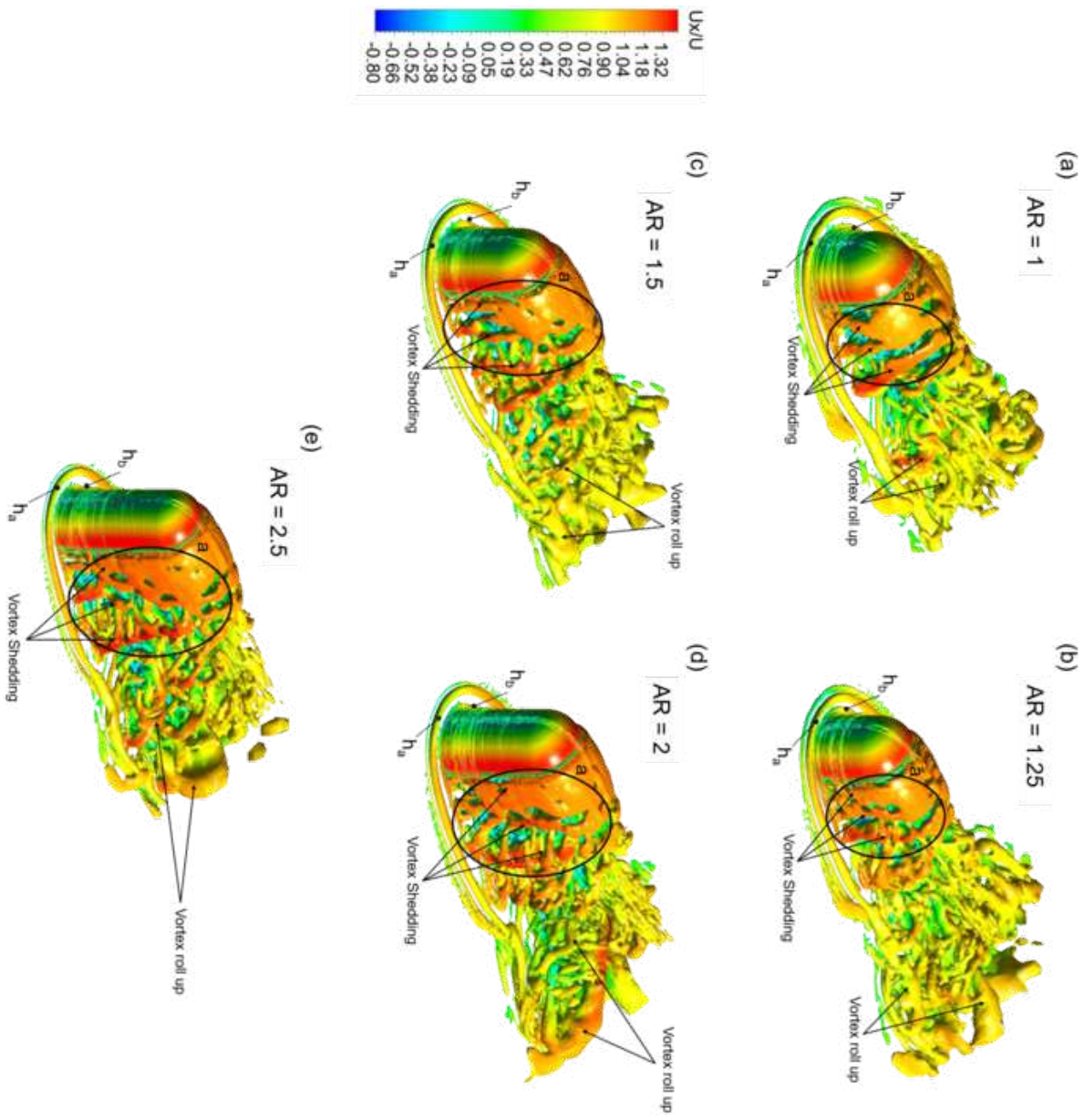

PLEASE CITE THIS ARTICLE AS DOI: 10.1063/5.0057166

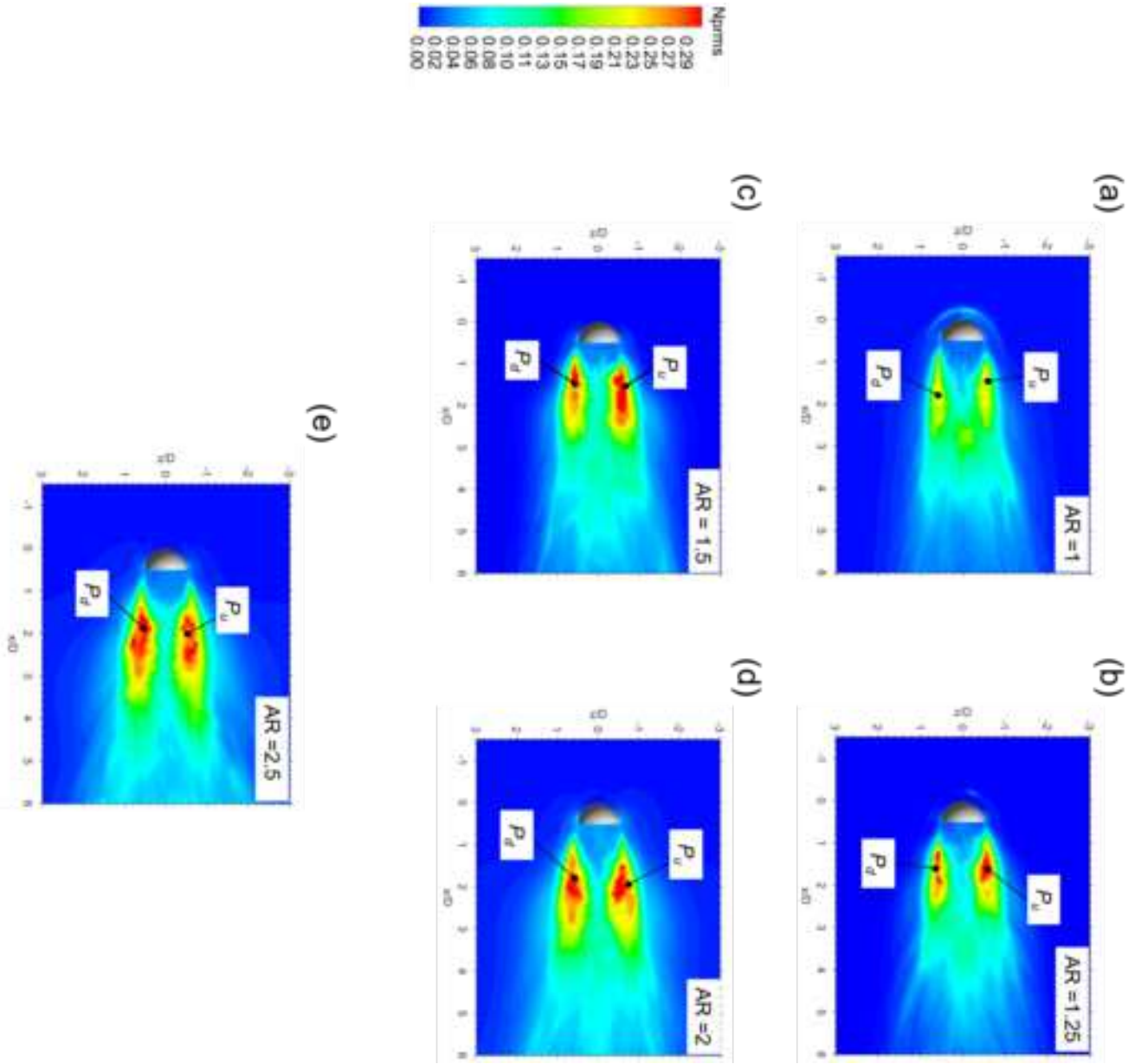

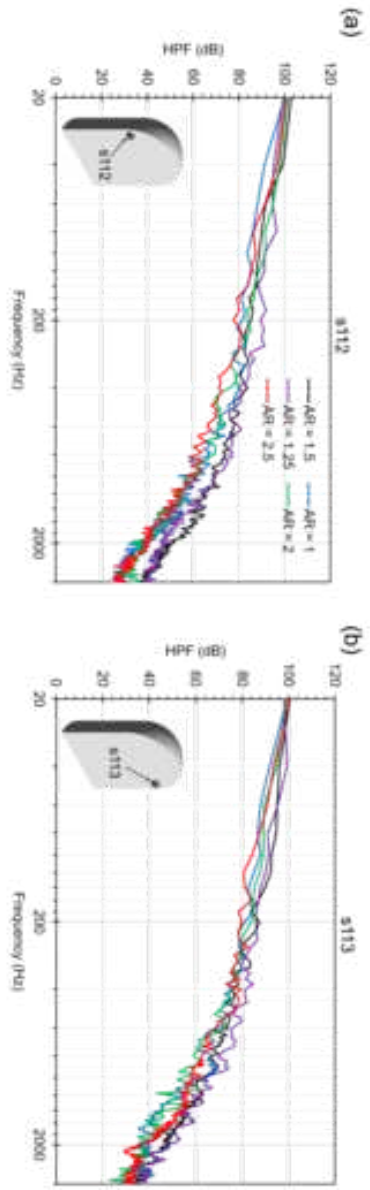

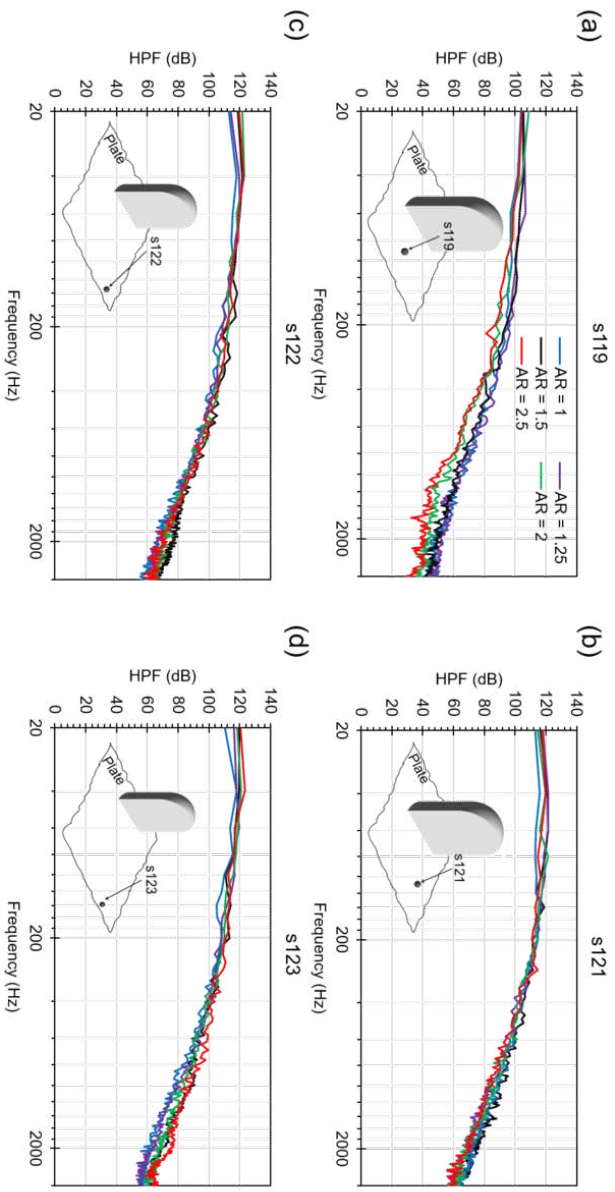

PLEASE CITE THIS ARTICLE AS DOI: 10.1063/5.0057166

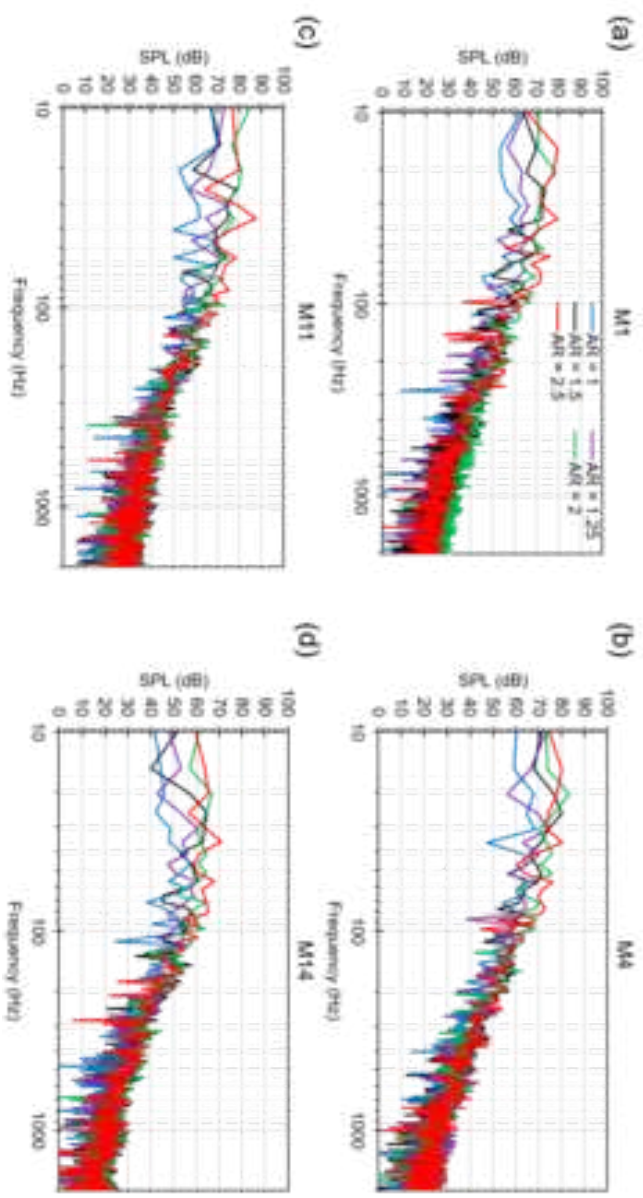

PLEASE CITE THIS ARTICLE AS DOI: 10.1063/5.0057166

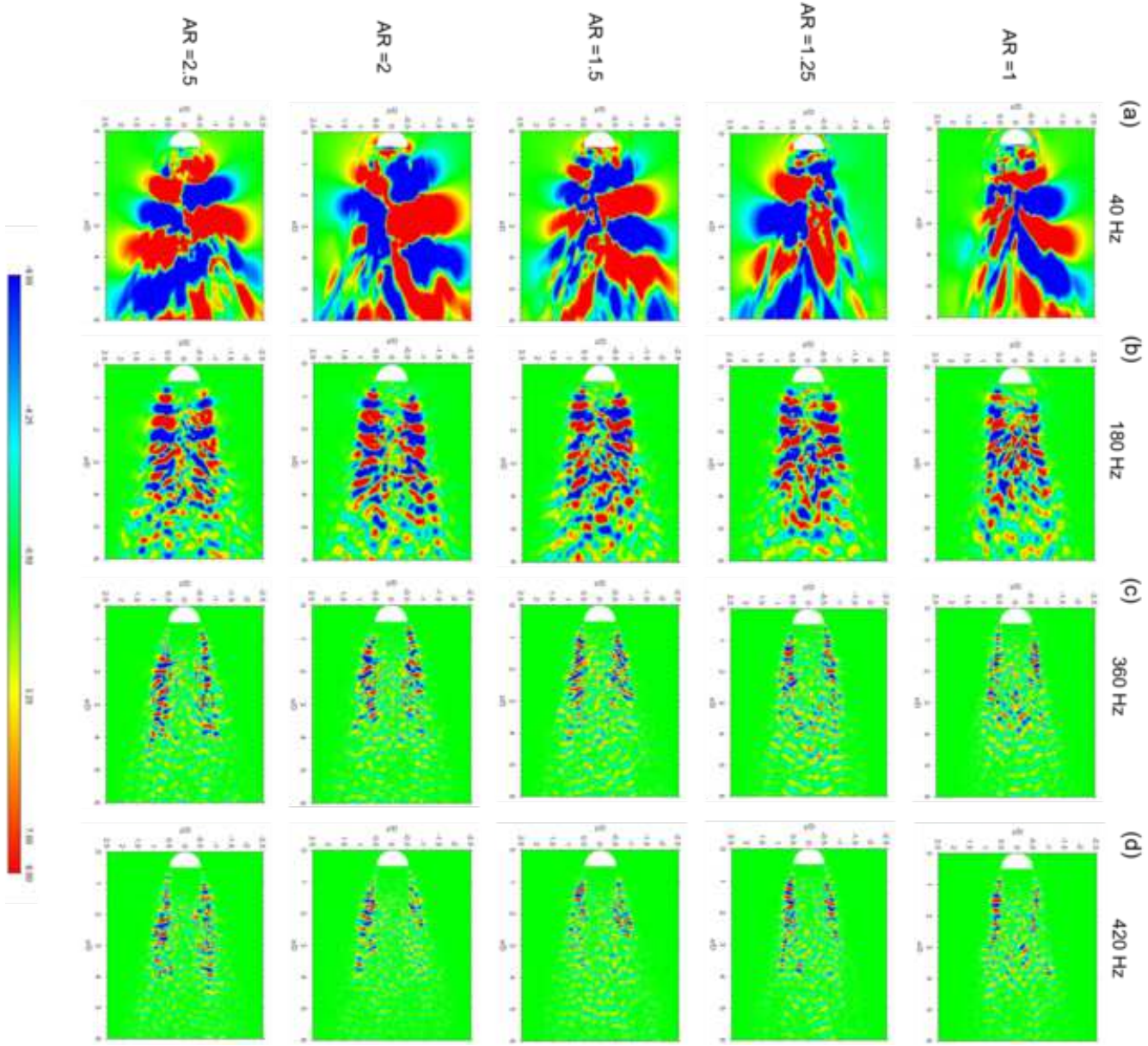

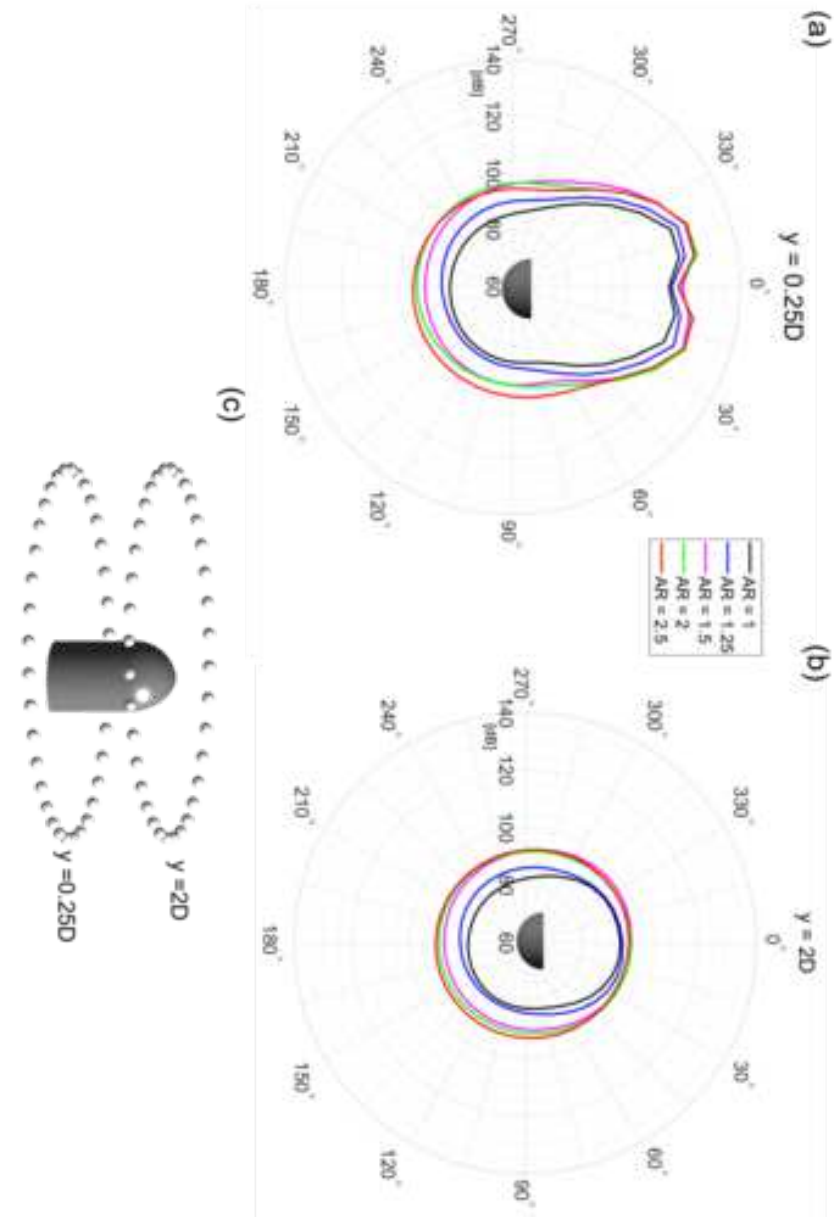

PLEASE CITE THIS ARTICLE AS DOI: 10.1063/5.0057166

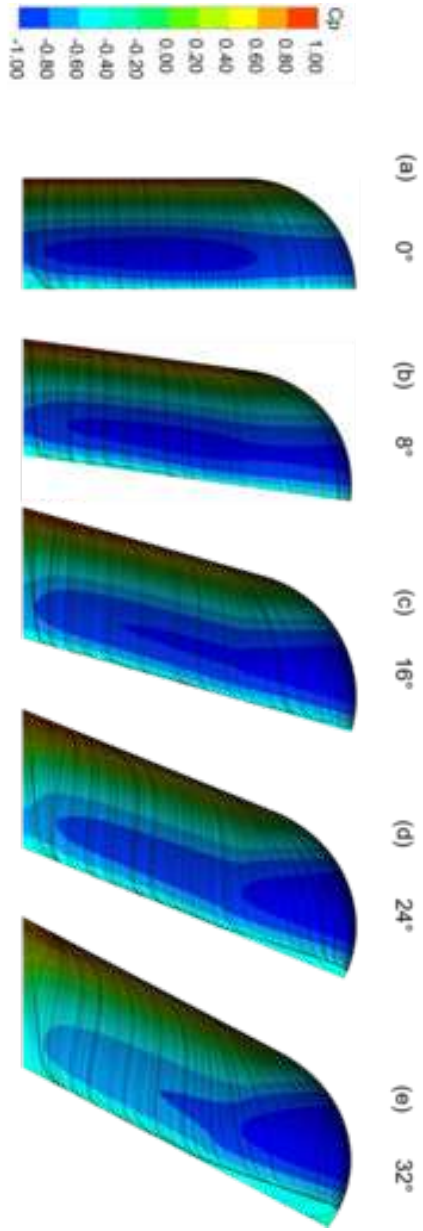

PLEASE CITE THIS ARTICLE AS DOI: 10.1063/5.0057166

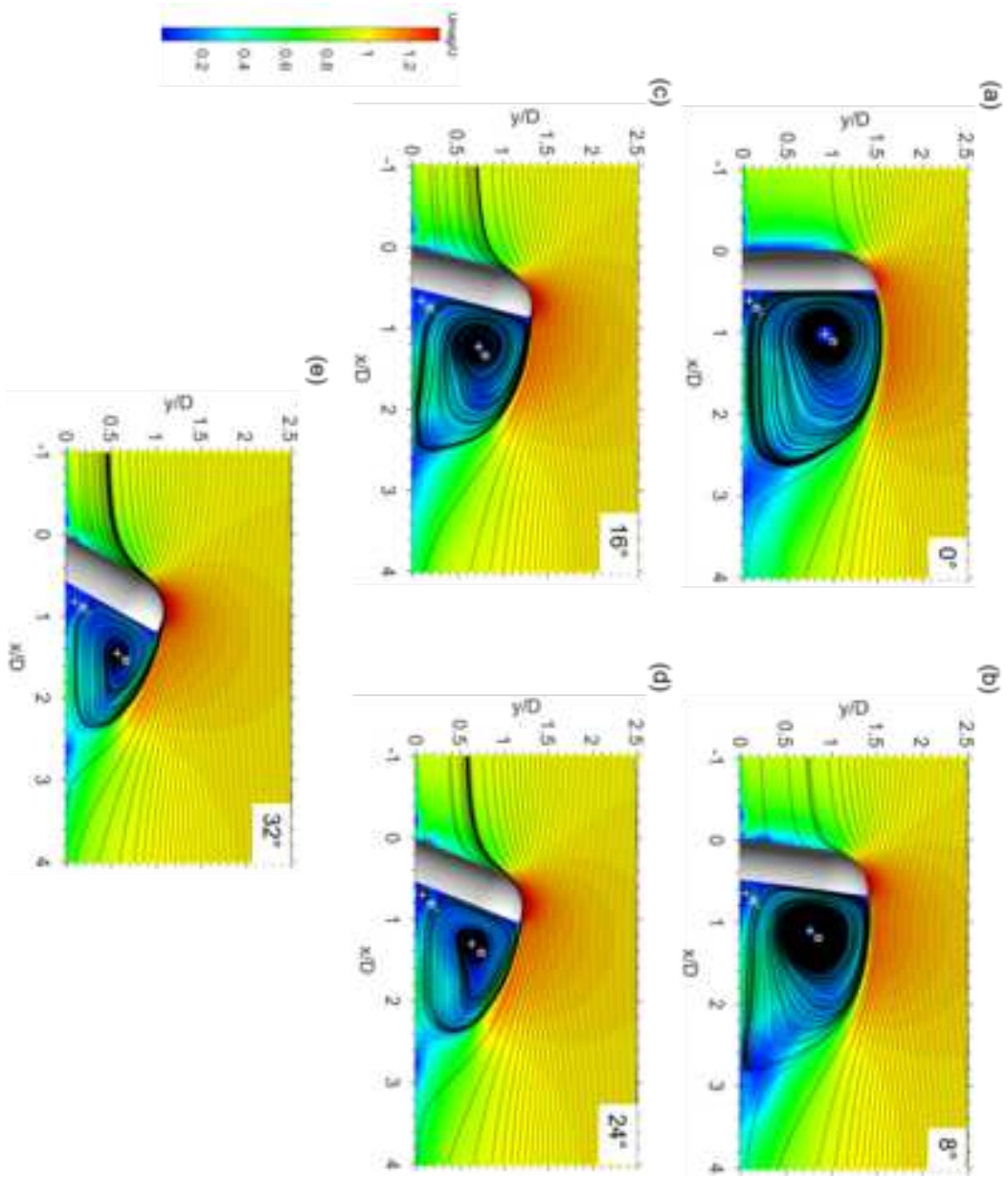

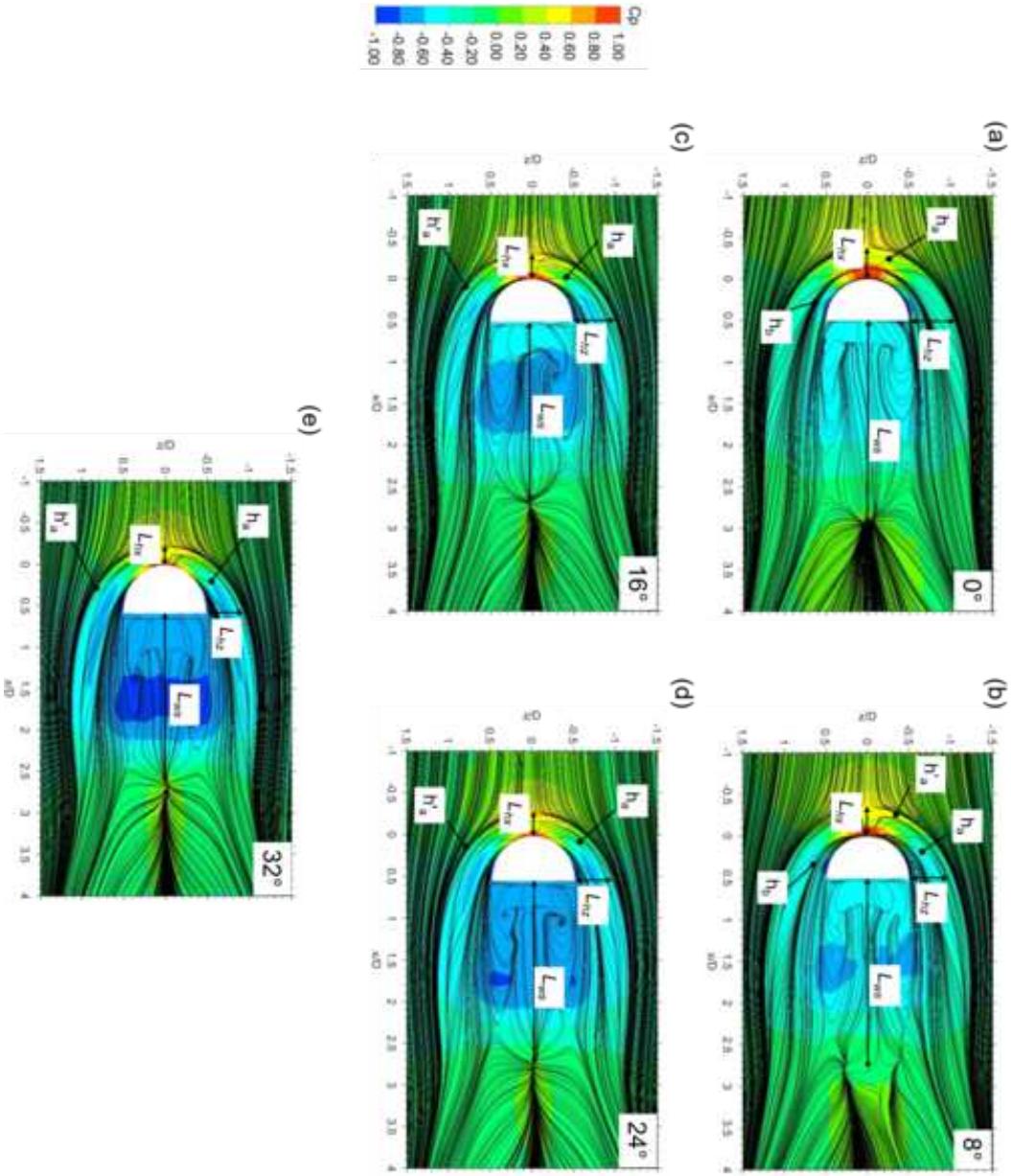

PLEASE CITE THIS ARTICLE AS DOI: 10.1063/5.0057166

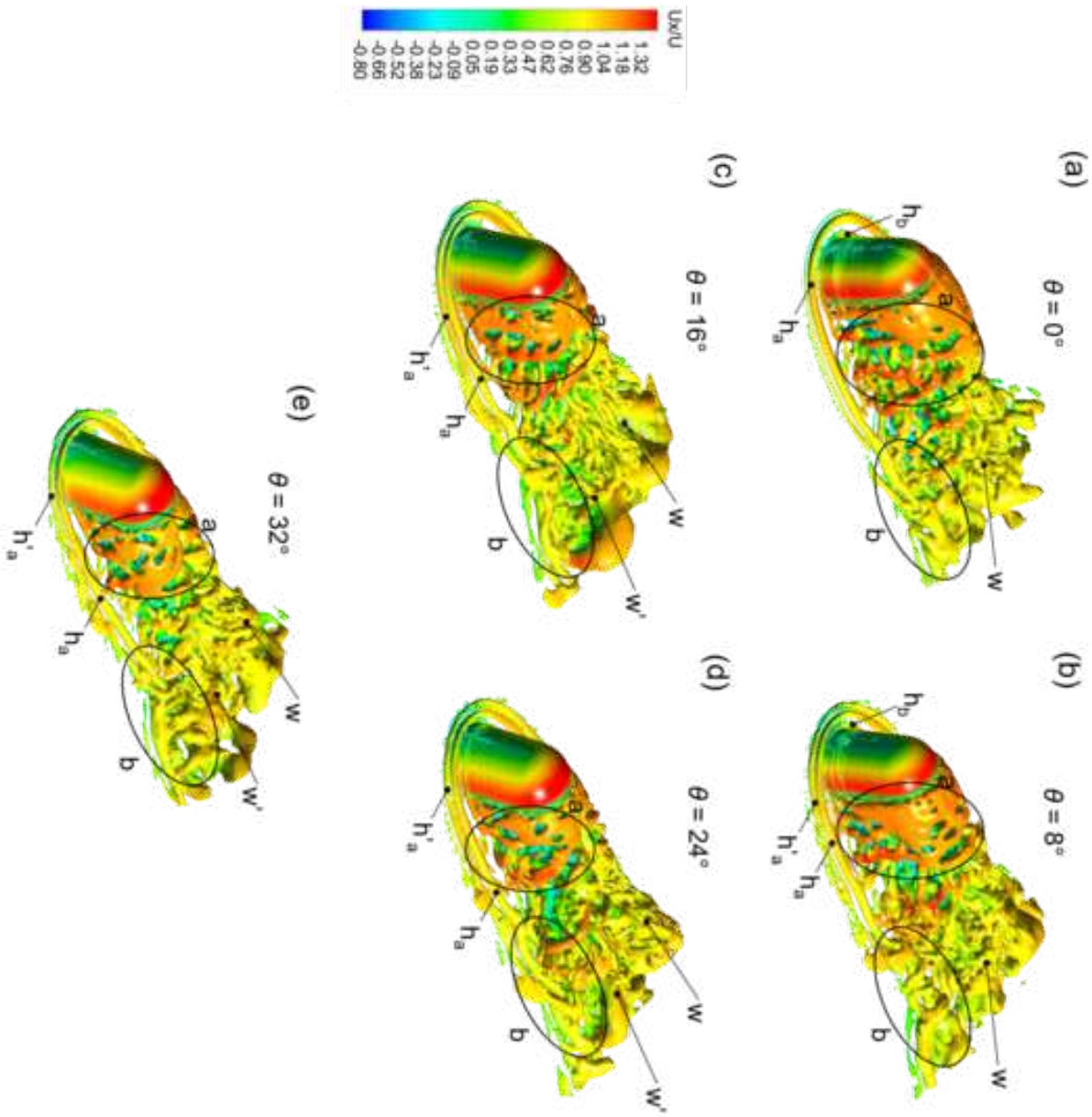

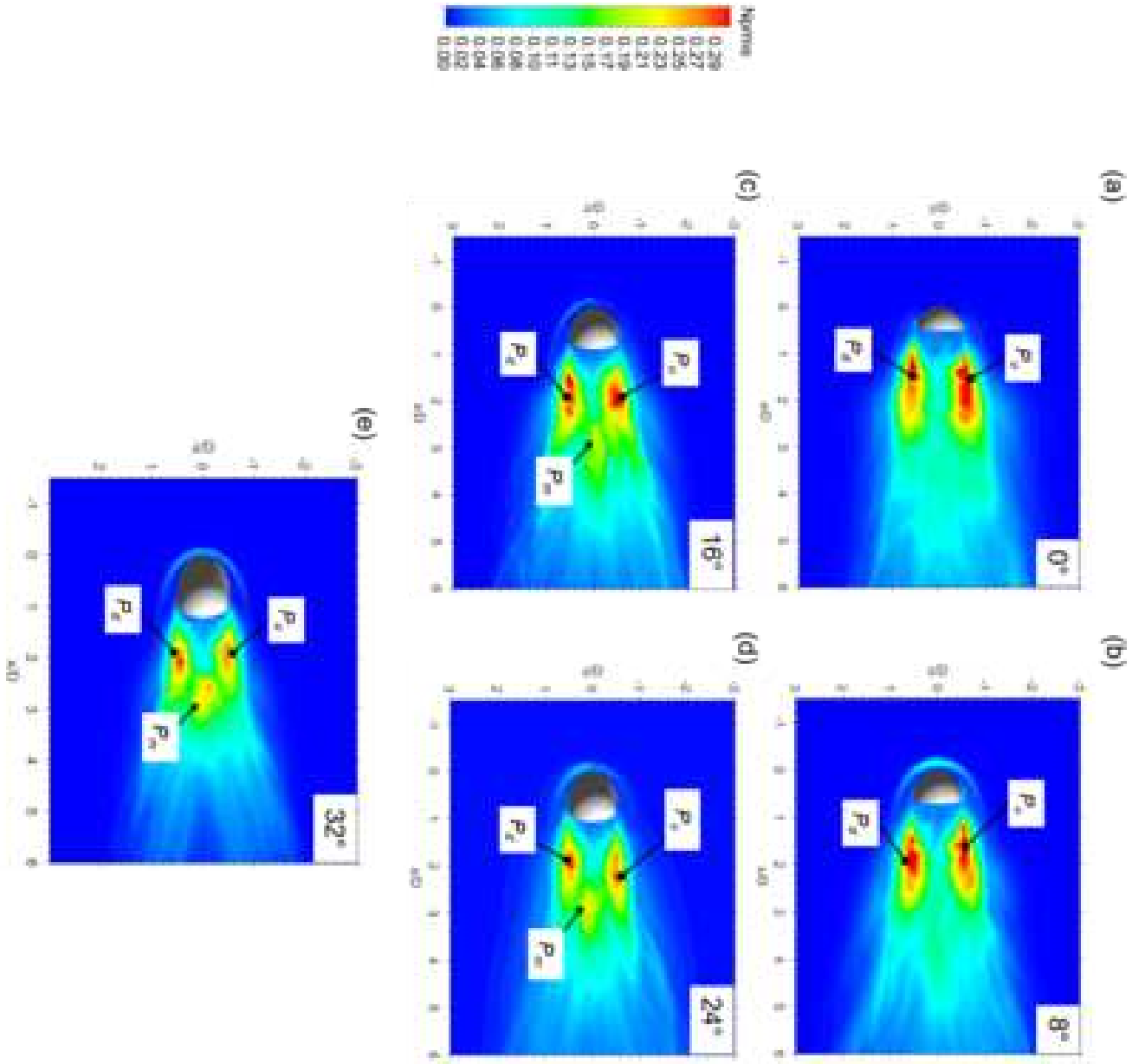

PLEASE CITE THIS ARTICLE AS DOI: 10.1063/5.0057166

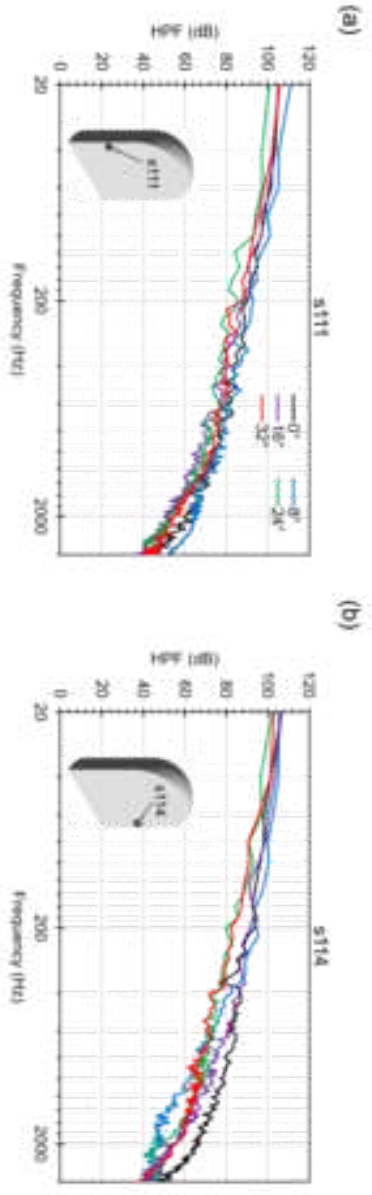

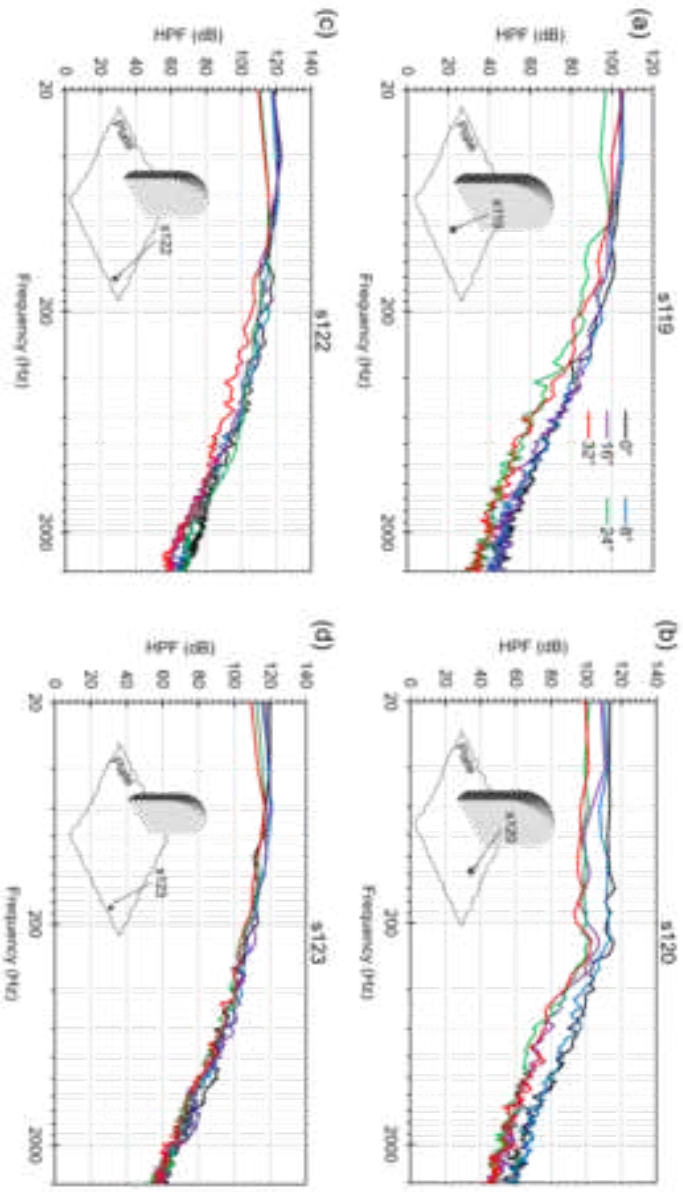

PLEASE CITE THIS ARTICLE AS DOI: 10.1063/5.0057166